Photophysical and Catalytic Properties of a Cubic Coordination Cage

---

Jennifer Suzanne Train

October 2019

A thesis submitted to The University of Sheffield in partial fulfilment of the requirements for the Degree of Doctor of Philosophy

Department of Chemistry, University of Sheffield, S3 7HF

Author's Declaration

Except where specific references have been made to other sources, the work within this thesis is the original work of the author. It has not been submitted, in whole or in part, for any other degree.

Jennifer Train

October 2019

Acknowledgments

Firstly, I would like to thank Professor Mike Ward for giving me the opportunity to do a PhD and work in his research group. His continuous support, guidance and enthusiasm for research has enabled me to complete my PhD and stay motivated throughout the three years. I am truly grateful for all the time and support you have given to me, thanks Mike.

Secondly, I am grateful for Professor Julia Weinstein for taking me under her wing when Mike moved, for supporting me throughout the three years and for always being a friendly face when needed.

Thank you to all of the past and present Ward group members. In particular, I would like to thank Alex Metherell for the help in my first year, showing me the ropes and for being a good friend. I would also like to thank Dylan and Beth, for their support in Sheffield; it would have been a lot harder remaining in Sheffield without you both. In addition, thanks to the Weinstein group for taking us in and making us feel like part of a group, especially Andy and James.

Thanks to Alex Auty and James Shipp for help with TA, Sandra and Craig for NMR support, and Alex Metherell, Chris Taylor and Stephen Argent for their X-ray Crystallography work. Also, thanks to the rest of the staff in the chemistry department at University of Sheffield, including Prof. Nick Williams and Simon Thorpe.

Next, thanks to all of my friends in the department, but especially the lunch bunch (Alex, Dave, James, Shannon and Joe) - Alex in particular, I could not have done it without you! I would also like to thank all past and present members of the office, especially Josh and the Foster group; you have been great to share the office with.

Lastly thanks to my family and non-chemistry friends for their support and interest in my work. Thanks to the netball girls, for letting me play for the last couple of years and for all of your energy. Finally, a special thanks to James, for keeping me going and always listening to my problems no matter how big or small.

Abstract

Chapter One consists of an introduction to supramolecular chemistry and supramolecular photochemistry. With particular focus on metal-organic cages and their application in catalysis and photocatalysis.

Chapter Two describes the synthesis of an Os(II) cage, photophysical properties and guest binding. Successful synthesis of water soluble $[Os_4Zn_4(L^{nap})_{12}]X_{16}$ coordination cage complex (where L^{nap} = bidentate pyrdiyl-pyrazole chelating ligand with a 1,5-dinaphthalene spacer and X = perchlorate or chloride) and $[Os(L^{me})_3]X_2$ (where L^{me} = methyl pyridyl-pyrazole and X = potassium hexafluorophospate or chloride). Both show strong visible absorption and emission at 630 nm. As well as reversible oxidation at 0.7 V and 0.6 V respectively. In addition, binding in the cavity of five guests is presented through X-ray crystallography, NMR titrations and luminescence titrations.

Chapter Three displays the evidence of photoinduced electron transfer detected by UV/vis transient absorption (TA) spectroscopy of three host.guest complexes. Ultrafast TA spectroscopy measurements show formation of a charge-separated Os(III)/guest$^{\bullet-}$ state, due to cage-to-guest photoinduced electron transfer. The states are formed within 13-21 ps and decay within 185-205 ps. Control experiments with a competing guest show that binding is required for the electron transfer to occur, as well as use of $[Os(L^{me})_3]X_2$ which shows that the Os(II) unit needs to be assembled in the cage structure for PET to occur.

Chapter Four details the study of binding of disulfide guests and looks for evidence of photo-induced electron transfer between cage and guest. The study indicates that there is a two-step binding profile for the binding of a selection of four aryl-disulfide guests. Binding with $[Os_4Zn_4(L^{nap})_{12}]X_{16}$, $[Cd_8(L^w)_{12}](NO_3)_{16}$ and $[Co_8(L^{nap})_{12}]Cl_{16}$ has been analysed with consistent binding constants of $10^3 – 10^5$ M^{-1} via different mediums: X-ray crystallography, NMR titration and luminescence titrations.

Chapter Five describes the use of $[Os_4Zn_4(L^{nap})_{12}]X_{16}$ to affect the catalysis of 5-nitrobenzisoxazole and the effects of changing the oxidation state of the cage. $[Os_4Zn_4(L^{nap})_{12}]X_{16}$ and $[Co_8(L^w)_{12}](BF_4)_{16}$ similarly catalyse the Kemp elimination of 5-nitrobenzisoxazole with a rate enhancement of 6 and 4 respectively, at pH 8.2. Control tests using a competitive binder also show an unexplained rate enhancement. Additionally, oxidised Os(III) cage catalyses the Kemp elimination reaction at a similar rate to the Os(II) cage.

Abbreviations

2θ	Angles of the diffractometer
Ǻ	Angstrom
α, β, γ	Unit cell angles
δ	Chemical shift
ε	molar extinction coefficient
λ	wavelength
τ	lifetime
μ	Linear absorption correction
A	acceptor
a, b, c	Unit cell dimensions
ArH	Aromatic proton
bipy	2,2'-Bipyridine
cat	catalysed
CD_3CN	Deuterated acetonitrile
CD_3NO_2	Deuterated nitromethane
$CDCl_3$	Deuterated chloroform
CFSE	Crystal field stabilisation energy
CT	charge transfer
D_2O	Deuterium oxide
DCM	Dichloromethane
DMF	Dimethylformamide
DMSO	Dimethylsulphoxide
DNA	Deoxyribonucleic acid
d	doublet
D	donor
DOSY	diffusion-ordered spectroscopy
ES	Electrospray
ESMS	Electrospray Mass Spectrometry
Et_3N	Triethylamine
eq	equivalents
F_o, F_c	Observed and calculated structure factors
fac	facial
G	guest
GOLD	Genetic Optimisation of Ligand Docking
H	host

H•G	host/guest complex
hr	hour(s)
HSAB	Hard-soft acid-base
Hz	hertz
IR	infra-red
J	coupling constant
K	binding constant
K	Kelvin
k	rate constant
L	Ligand
lum	luminescence
m	multiplet
M	Metal
Me	Methyl
MeCN	Acetonitrile
$MeNO_2$	Nitromethane
MeOD	Deuterated methanol
MeOH	Methanol
mer	meridional
$MgSO_4$	Magnesium sulphate
MLCT	metal-to-ligand charge transfer
m/z	Mass to charge ratio
NMR	Nuclear Magnetic Resonance
Ph	phenyl
PPh_3	Triphenylphosphine
ppm	parts per million
PyPz	Pyrazolyl-pyridine
R_1, wR_2	R-indices (based on F and F_2 respectively)
s	singlet
sh	shoulder
t	triplet
T	temperature
TA	transient absorption
uncat	uncatalysed
UV	Ultraviolet
V	unit cell volume
Z	Formula units per unit cell

List of Publications

1. **J. S. Train**, A. B. Wragg, A. J. Auty, A. J. Metherell, D. Chekulaev, C. G. P. Taylor, S. P. Argent, J. A. Weinstein and M. D. Ward, *"Photophysics of Cage/Guest Assemblies: Photoinduced Electron Transfer between a Coordination Cage Containing Osmium(II) Luminophores, and Electron-Deficient Bound Guests in the Central Cavity". Inorg. Chem.*, 2019, **58**, 2386–2396.

2. A. M. James, M. J. Derry, **J. S. Train** and R. Dawson, "*Dispersible Microporous Diblock Copolymer Nanoparticles via Polymerisation-Induced Self-Assembly". Polym. Chem.*, 2019, **10**, 3879–3886.

Contents

Chapter 1

Introduction

1.1 Supramolecular Chemistry

Supramolecular chemistry is the study of interactions beyond the molecule. This generally refers to the bonding, organisation and properties of complex assemblies of molecules held together by non-covalent interactions. Including cycles, cages and knots as well as nanowires, DNA, proteins and molecular machines, there are a huge range of applications for these molecules in all areas of science, from biology to materials science.[1] Early studies in supramolecular chemistry developed from the study of simple host-guest chemistry of crown ethers to self-assembly of far more elaborate structures and now to the study of their functions, making supramolecular chemistry a very dynamic area of chemical studies.

1.1.1 Self-assembly

Self-assembly is the process by which an organized structure spontaneously forms from individual components as a result of specific, local interactions among the components.[1] Formation of the resulting supramolecules is entropically unfavourable as there is a large loss in the number of degrees of freedom upon combining several molecules into one larger structure. However, as additional non-covalent interactions are produced in the supramolecular assembly, formation of the supramolecule does also provide some enthalpic compensation. In addition, for true self-assembly to occur, the interactions need to be weak and form reversibly, in order to allow the system to move towards the true thermodynamic minimum by allowing ‘incorrect’ assemblies to break and re-form.[2]

1.1.1.1 Self-assembly in nature

Self-assembly is highly prevalent in nature, with many famous examples including (i) the DNA (deoxyribonucleic acid) structure, whereby the complementary interactions between the two strands give rise to this unique self-assembled double helix (figure 1.1.1), and (ii) the tobacco mosaic virus, which is made up of a central strand of DNA surrounded by 2130 identical protein units which assemble reversibly under the correct conditions. When the virus particle is decomposed into its individual components and then mixed under physiological conditions, it then perfectly reforms to form the same complex structure, from all >2000 parts, with the same functionality, showing the real power of self-assembly.[1,3]

These are examples of strict self-assembly in which the product formation is completely reversible, because the self-assembled structure is purely based on weak non-covalent interactions, resulting in the thermodynamic product being formed. In contrast to this, self-assembly with covalent modifications can sometimes occur, which involves the formation of covalent linkages, this can entail the covalent formation of a precursor or post-assembly covalent modification. For example, the biosynthesis of insulin involves the formation of irreversible disulphide linkages post self-assembly of the polypeptide chains.[1] In general, this type of self-assembly is irreversible and so the thermodynamic minimum product is not necessarily formed.

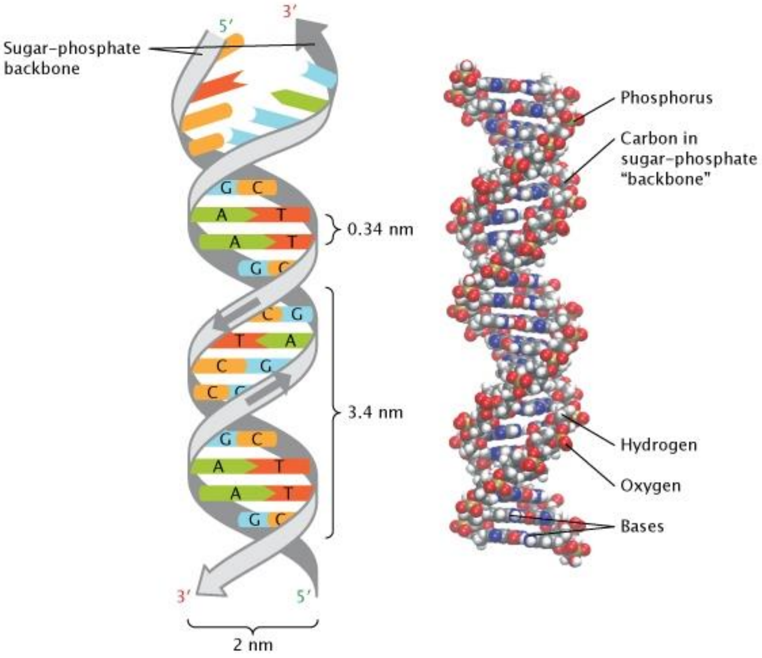

Figure 1.1.1: Double helix structure of DNA.[4]

1.1.1.2 Synthetic self-assembled cages

The incorporation of metal ions into the self-assembly of supramolecules is beneficial as they provide a range of predictable geometries and bond angles, bringing some predictability to formation of structures. In addition, where labile metal ions are used, the metal-ligand bond lability allows for fast and efficient assembly, without the need for a template and multistep syntheses. The use of metal ions is also advantageous because of the functionality that metal ions may bring to the molecule, including photo-activity, magnetism, and redox properties.

Three-dimensional coordination cages, in which a central cavity is surrounded by an array of metal ions and bridging ligands, have been of great interest within supramolecular chemistry. Saalfrank was a pioneer in this field, giving the first example of a self-assembled coordination cage in 1988.[5] An M_4L_6 tetrahedron, with four magnesium(II) ions and six bridging bis-enolate ligands, was fortuitously prepared through the condensation of diethyl malonate and methylmagnesium bromide (figure 1.1.2a).[5] From this, the field has expanded dramatically, with recent impressive examples being Fujita's $M_{30}L_{60}$ and $M_{48}L_{96}$ 'nanocages'; these were rationally designed based on a bipyridyl-type bridging ligand, which were designed to have a small bend between the termini which gives a slight degree of curvature to the cage (bend angle, $\theta = 152°$), arising from combination with Pd(II) ions (figure 1.1.2b).[6] Since then, many groups have delved into this exciting area and produced a large array of shapes and sizes of self-assembled cages, with various different functionalities, based on combination of rigid components to form specific geometries.[7]

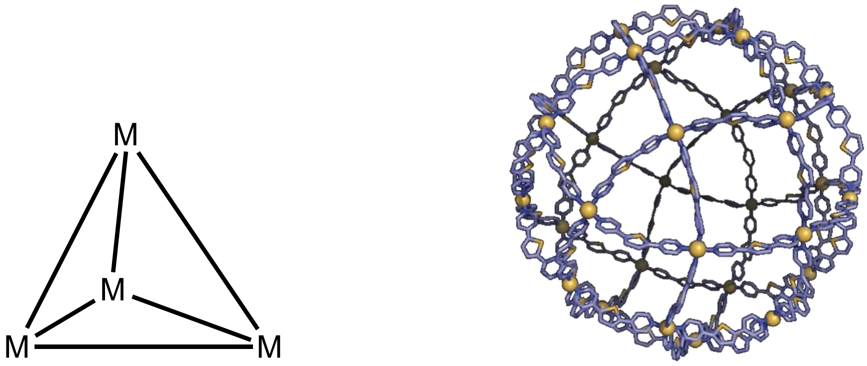

Figure 1.1.2: (a) Depiction of Saalfrank's M_4L_6 tetrahedron and (b) Crystal structure of Fujita group $Pd_{30}L_{60}$ coordination sphere (right). (Reprinted with permission from ref. 6. Copyright 2016 Springer Nature.)

1.1.1.3 Mixed-metal cages

The majority of cages contain only two types of component (one type of metal ion and one type of ligand), which limits the functionality that can be incorporated into such molecules. Mixed-metal coordination cages are an ideal way to increase the range of functional behaviour, as the use of more than one type of metal can expand the range of photophysical, electrochemical and magnetic properties displayed by a cage. The synthesis of heterometallic cages is dependent on the kinetic lability of the metals used, and such cages can either be formed through a kinetic or thermodynamic control approach.

The Ward group has previously made use of the kinetic control approach, whereby they use inert ruthenium(II) or osmium(II) metal ions, which are functionalised with pendant ligands (figure 1.1.3) to give a mononuclear ‘complex ligand’ with pendant binding sites. These 'complex ligands' with vacant binding sites are then mixed with a labile metal, for example silver(I), cadmium(II) or cobalt(II) which connect the vacant binding sites to produce a series of different cage structures which all contain two different types of metal centre.[8,9,10,11] The most elaborate of these designs is depicted in figure 1.1.3, which – as well as incorporating two different types of metal ion – also comprises two different ligands. The application of ditopic ligands which have pendant binding sites means that the self-assembly of the $[Ru_4Cd_{12}(L^a)_{12}(L^b)_{12}]^{32+}$ cage is possible, which can incorporate the useful redox and photophysical properties of inert second and third row d-block transition metals.[12]

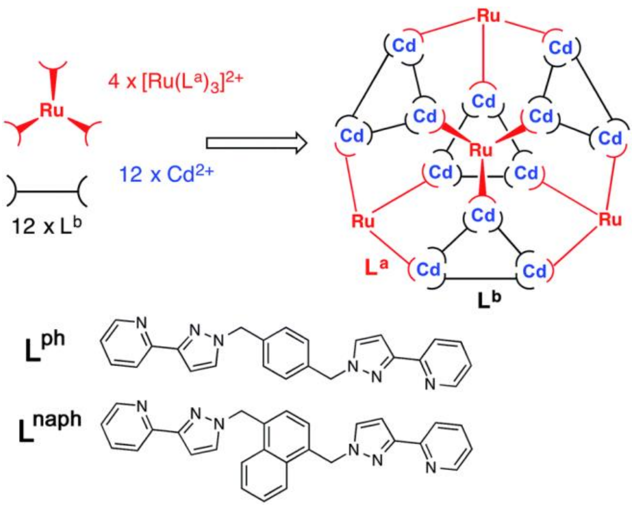

Figure 1.1.3: Ward group $[M_{16}L_{24}]^{32+}$ cage, made up of four components. (Ref.12 - published by the Royal Society of Chemistry)

A thermodynamically controlled approach has also been applied to the design of 3D coordination structures. This approach utilises the hard-soft acid-base principles, with 'hard' metals and 'hard' ligands connecting to each other and soft metal ions binding preferentially to soft ligands. Thus, employment of unsymmetrical ligands is important incorporating a mixture of hard and soft binding sites which will select for different types of metal ion. An example of this approach, without the use of pre-formed ligands, is from the Nitschke group, who were able to use 62 subcomponents to form a single cubic structure of $Fe_8Pt_6L_{24}$ (figure 1.1.4). To form this structure, the individual components were modified so that a symmetrical ligand could not form and that the two metals would favour different binding sites, this utilised hard/soft preferences as well as the preference of Fe(II) for low-spin octahedral geometry and of Pt(II) for square planar geometries. This enabled a one-pot synthesis with 96 new bonds being formed, which shows the strength of thermodynamic control on making complex heterometallic structures.

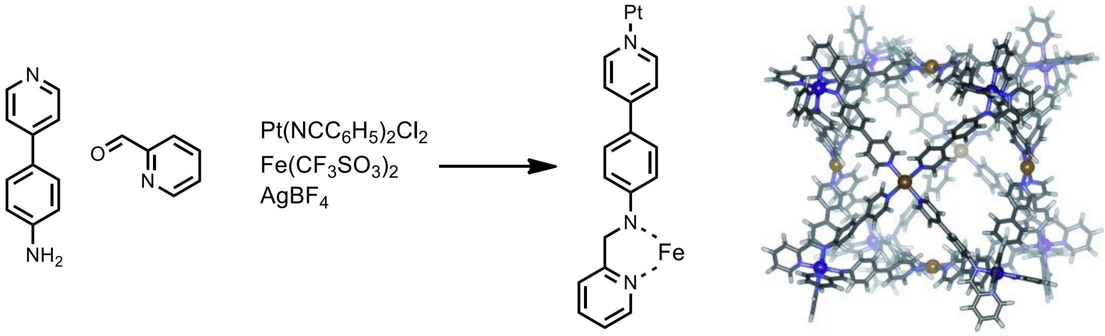

Figure 1.1.4: $Fe_8Pt_6L_{24}$ cage from subcomponent assembly, with one ligand to indicate coordination modes (reproduced with permission from ref. 14).

1.1.2 Host-guest chemistry

Host-guest chemistry is synonymous with supramolecular chemistry and cages. It involves the non-covalent interaction between a host molecule and a particular guest, in order to produce a host:guest supramolecule.[1] The origins of host-guest chemistry come from the study of macrocycles including crown ethers, beginning in 1987 (figure 1.1.5), with the ultimate aim to mimic the ability of enzymes to specifically recognise and catalyse reactions.[13,14]

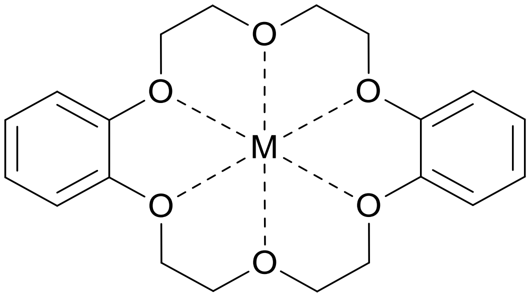

M = various salts of alkali and earth metals

Figure 1.1.5: Pederson’s pioneering crown ether host:guest supramolecule.

Enzyme binding works through a ‘lock and key’ mechanism which was first recognised in 1894 by Emil Fischer, who described that binding of substrates must be selective, through analysis of the receptor-substrate mechanism of enzymes.[15] This is the basis of molecular recognition and shows that the guest must have a size or shape complementary to the host in question. In addition to this, in 1958, Daniel Koshland proposed the induced-fit model.[16] This suggests that when the active site on the enzyme makes contact with the substrate, the enzyme host then moulds itself to the shape of the substrate. This is in contrast to the lock and key mechanism where the enzyme doesn’t alter its shape upon substrate binding. Both theories are accepted and the induced-fit model builds on the original discovery of substrate recognition.[17]

To construct a stable host-guest complex with a *metal ion* guest, the chelate and macrocyclic effects mean that there should be as many donor atoms as possible. This is because the interactions are weak compared to covalent interactions, so the cumulative effect of many of these interactions are needed for the resultant binding energy between host and guest to be significant.[1] The effectiveness of the macrocyclic effect in polydentate ligand hosts is due to the preorganisation of large molecules, meaning that there is less entropic and enthalpic costs of guest binding, compared to a long open-chain ligand for example. This effect is shown in Pedersen’s example above, where all six oxygen atoms of the cyclic ether are turned inward to provide dipole-to-ion bonds between host and guest.[18]

Since these early days, host-guest chemistry has developed enormously, with a large variety of host structures, and many different guests, ranging from alkali salts, to organic and inorganic compounds. This progression has forwarded the applications of host-guest chemistry and molecular recognition to sensors,[19–23] catalysis,[24–29] encapsulation of unstable species,[7,30,31] and drug delivery.[32–35]

1.1.2.1 Guest binding in cages

Molecular coordination cages have proven to constitute an exciting branch of supramolecular chemistry, not only due to their ability to utilise the power of self-assembly to produce remarkably complex structures, but because their large central cavities allow for the potential of host:guest (H.G) chemistry to occur; the confined spaces may provide an unusual and unique environment for guest molecules.

As previously stated, guest binding in a host cavity depends on the intermolecular forces between host and guest: these include hydrogen bonding, electrostatic interactions, non-polar interactions between aromatic regions, and solvophobic interactions.[36] These interactions vary in their strength, with ion-dipole interactions, like in the crown ether above, being the strongest at 50-200 kJ mol^{-1}; with hydrogen bonds (H-bonds) also having the ability to be fairly strong at 4-120 kJ mol^{-1}, because these are a kind of dipole-dipole interaction whereby a hydrogen atom attached to an electronegative atom is attracted to a neighbouring dipole.[1] π-π stacking is the next strongest interaction at 0-50 kJ mol^{-1}, and is when an electrostatic interaction occurs between aromatic rings, in which the negative electrostatic potential on one ring aligns with the positive electrostatic potential of another ring. Lastly, Van der Waals forces are around <5 kJ mol^{-1} and arise from the polarisation of electron clouds by an adjacent atom to give transient dipoles.[1]

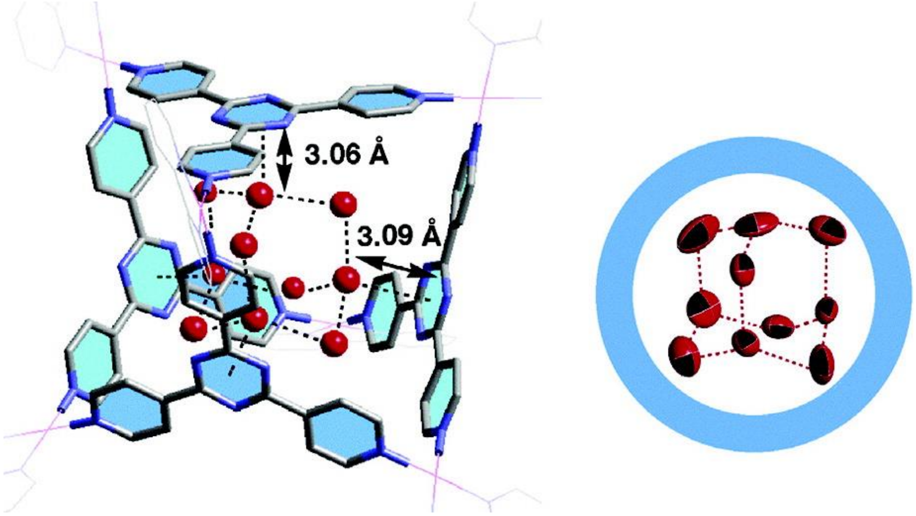

Figure 1.1.6: X-ray crystal structure of molecular ice in a coordination cage cavity.[38] (Reprinted with permission from ref. 38. Copyright 2005 American Chemical Society.)

Solvophobic interactions are particularly important in host/guest binding, however they aren't strictly a force, and occur predominantly due to the entropy increase upon H/G binding. In water these solvophobic interactions are known as the hydrophobic effect and play a key role in guest binding. The 'iceberg' model is based on the observation that water has the ability to aggregate to form hydrogen-bonded networks. Thus when water molecules are in contact with hydrophobic molecules, ordered arrays of water molecules spontaneously form at the surface, so that when the surfaces of host and guest molecules come together, the ordered array of water molecules around the hydrophobic surfaces is released back into the bulk solution, which as a result increases the entropy.[37,38] This release of water molecules can also result in favourable enthalpy changes if the water molecules can form more H-bonds in solution than they can around the hydrophobic surface, this means that the hydrophobic effect can have an unpredictable combination of entropy and enthalpy changes in different systems.[39,40]

As well as this, the size of the guest has an important influence on binding inside the cavity. The work of Rebek is fundamental in this by quantifying the volume that a guest must take up within the cavity. Rebek found that the optimal volume of the guest should be 55 ± 9 % of the volume of the cavity to give the greatest binding strength in the liquid phase, as the host-guest interactions are optimised.[41] This is reflected in the packing coefficient of most organic solvents, as about 55% of the space in these solvents is occupied by molecules, in liquids such as methanol, acetonitrile and chloroform.[42] However this is not an upper limit, as it was also found that filling of up to 70 % can be achieved if there are suitable hydrogen bonds in play, as they make up for the decrease in entropy from the limitation of thermal motion, and increase the enthalpic contribution.[41]

Binding constants

To determine the extent to which guest binding occurs inside a cage host, binding is quantified by determining the binding constant. The binding constant, *K*, is a measure of thermodynamic stability of a host.guest system compared to the separate species, and as shown in equation (1) (where [HG] = conc. of host•guest, [H] = conc. of host, [G] = conc. of guest). It is often seen as a ratio between the concentrations of each species in the equilibrium. The higher the binding constant, the higher the concentration of H•G complex compared to unbound material, which therefore means a more stable system. The Pedersen example above, in figure 1.1.5 has a very large binding constant of 1.2×10^6 M^{-1} (in ethanol) with K^+ as the metal ion, showing that this host has a high affinity for the guest when the H•G complex is formed.[43,44,13]

$$K = \frac{[\mathrm{HG}]}{[\mathrm{H}][\mathrm{G}]} \qquad (1)$$

Titrations are a common tool in determining the binding constants of guests in cage cavities and can be determined using various methodologies, with the most common being NMR or luminescence spectroscopy.

Titrations are generally performed whereby one component, the guest, is added in small portions to a second component, the host, while monitoring a certain physical property such as change in NMR chemical shift or luminescence intensity that is sensitive to the supramolecular interaction(s) of interest.[45] The resulting information is then analysed and fitted to binding models to obtain information such as the binding constant. The most common type of binding is 1:1 and so for example in ^{1}H NMR spectra, we will observe the behaviour shown in equation 2, upon titration (where $\Delta\delta$ = change in chemical shift and $\delta_{\Delta HG} = \delta_{HG} - \delta_{H}$).

$$\Delta\delta = \delta_{\Delta HG}\left(\frac{[HG]}{[H]}\right) \qquad (2)$$

1.1.2.2 Coordination cage enabled catalysis

As previously stated, there are many applications of host-guest chemistry including drug delivery[34,20,46] and sensing,[23,22,47] with one of the most exciting applications being reaction catalysis.[7,27,48–52] Catalysis using H•G assemblies is of prime importance in achieving the goal of mimicking enzyme ability. Cages have the potential to be a powerful tool for accelerating reactions, due to the unique enclosed space, within which the effective molarity of bimolecular reactions is increased, so that the intramolecular forces can have an effect greater than the intermolecular forces and thus accelerate the rate of reaction (as the reactants will be isolated from the bulk solvent).[31] Cages also have the ability to stabilize transition states of the guests (sometimes more strongly than the ground state) and accommodate uncommon confirmations of such guests, allowing for an increase in reaction rates and a higher probability of unique reactions.[27]

In contrast to this, there are many challenges to finding suitable reactions and hosts to use in cage-enabled catalysis. Processes like product inhibition can occur, where the product ends up binding more strongly to the inside of the cage compared to the reactants, as well as impediments such as new reaction products being too large to then leave the cage. Therefore, determining the complementary host/guest/products combination is critical.[31]

Although there are many examples of the use of cages to facilitate new reactions, there have been relatively few examples of existing reactions that have been greatly accelerated by cages. One of the first examples of cage catalysis was by Fujita and co-workers in 2006. They utilised an M_6L_4 cage to investigate the Diels-Alder reaction of anthracene and N-cyclohexylmaleimide. This led to regioselectivity of the 1,4-product by pre-organising the substrates, however the reaction was non-catalytic due to product inhibition. More recently the Fujita group have developed a chiral M_6L_4 cage, to achieve the asymmetric [2+2] olefin cross-photoaddition of fluoroanthene and maleimide. Fluoroanthene tends to be inert to photochemical pericyclic reactions, however when combined in the cage, due to preorganisation the reaction proceeds.[29,53] In the past year the group has also developed a system for cascade reactions, using two separate cages in solution, which are internally functionalised with catalysts, thus protecting their active sites from unwanted reactivity (figure 1.1.7).[54] The reactions that they have cascaded are an allylic oxidation followed by a Diels-Alder cyclization to enable controlled synthesis of an asymmetric ring. This is unique, as usually the catalysts (for oxidation and for the Diels-Alder reaction) wouldn't be compatible with each other in the same solution, as typically the Diels-Alder catalyst will be oxidised by the oxidation catalyst. However, by using an $M_{12}L_{24}$ cage, where they have covalently pre-linked the catalyst to the bent ditopic ligand and then formed the cage, they have created a protected environment in the cage cavity of 24 catalytic sites.

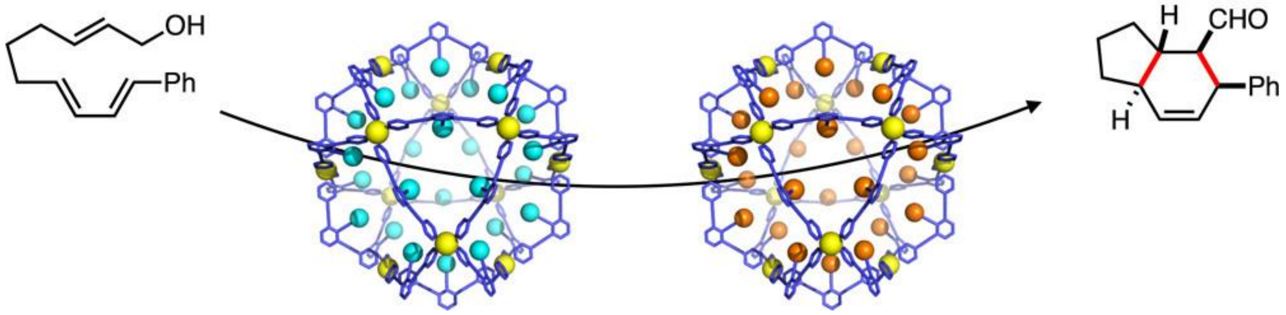

Figure 1.1.7: Cascade catalysis scheme utilising two functionalised cage molecules. (Reprinted with permission from ref. 52. Copyright 2017 American Chemical Society.)

Another very recent example of cage catalysis has been performed by the Cui group, who in 2018 made two cages of $[Zn_8L_6](OTf)_{16}$ structure, which contain six tetrakis-bidentate ligands and eight zinc(II)tris(pyridylimine) (TPE) centres, where the tetrakis units differ in size between the two cages, resulting in a TPE-faced cage with a tuneable cavity size.[55] Using these cages, the group have performed a sequential condensation and cyclization of anthranilamides with aldehydes (figure 1.1.8). This reaction produces bent shaped 2,3-dihyroquinazolinones, with a rate acceleration of 38000-fold. The unfavourable nonplanar configuration of the product expels it from the cage cavity and the acceleration is attributed to strength of binding affinity for the reactants in the cage cavity. The group has also done some work in which they have synthesised a collection of chiral coordination cages, which have been efficient supramolecular catalysts for sequential asymmetric alkene epoxidation/epoxide ring-opening reactions, which have up to 99.9% ee.[56]

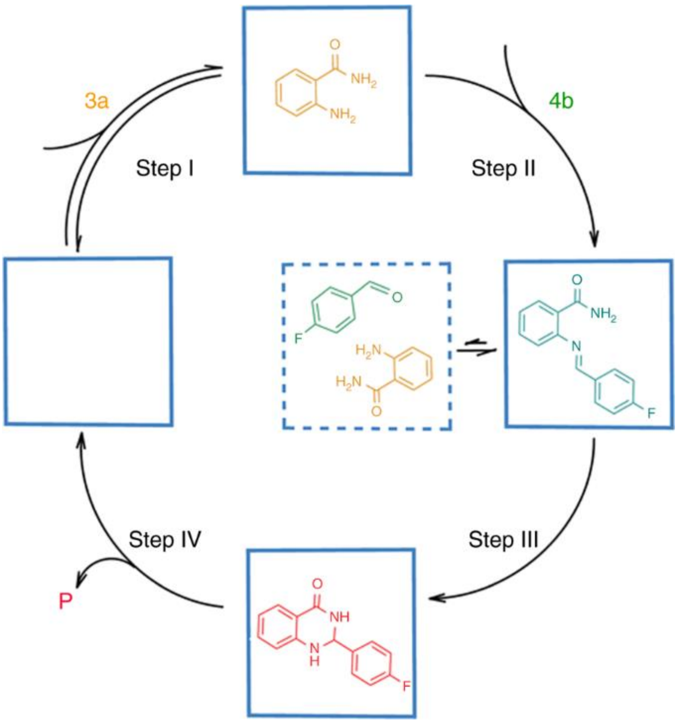

Figure 1.1.8: Cascade reaction of bound anthranilamide with an aldehyde in a Zn_8L_6 cage.[55]

1.2 Supramolecular Photochemistry

Supramolecular chemistry is associated with the intermolecular interactions between assemblies of molecules; supramolecular photochemistry, on the other hand, is related to the nature of the excited states of both the host and guest molecules formed upon photo-excitation.[57] For example, in a supramolecular system with two units, A and B, photoexcitation must either lead to a case where the excited states formed are localized on either A or B, or where the excitation leads to electron or energy transfer from A to B. The two components are spectroscopically distinct, which contrasts with the behaviour of a large molecular system where the excited state may be delocalized over the whole system.

1.2.1 Photoinduced electron transfer

Natural photosynthesis has inspired studies into photoinduced electron transfer in artificial assemblies, due to the photosynthetic processes in plants and bacteria that efficiently harvest solar energy.[58] Both photoinduced electron and energy transfer steps are involved in natural photosynthesis. Consequently, it is an appealing area in which to research as there is the potential to utilise the sun's light to produce solar fuels (when solar energy is converted into chemical energy in the form of chemicals) and perform photocatalysis.[59] If such behaviour could be mimicked in an artificial system, then it should be possible to harness solar energy in a similar way to plants, which is of prime importance due to the need of renewable energy sources to meet the world's increasing energy demand.

1.2.1.1 Artificial photosynthesis

Photosynthesis is a very complex process, in which plants successfully convert light, CO_2 and H_2O into energy (ATP) and fuel (sugars).[60] In plants, antennae systems are used that comprise a chromophore (*i.e.* chlorophyll) that strongly absorbs light and initiates the light cycle shown in figure 1.2.1. The antenna then transfers energy to the reaction centre, through the proteins, where charge separation occurs between a donor (D) and acceptor (A). This electron transfer then generates oxidising and reducing centres which then facilitates the production of carbohydrates (by reduction of CO_2) and oxygen (by oxidation of water).[61]

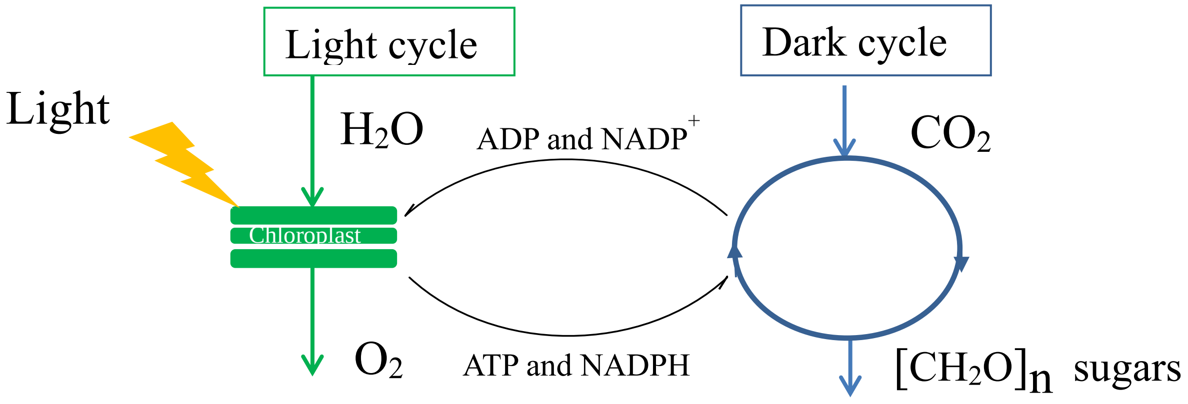

Figure 1.2.1: Light and dark (Calvin) cycles of photosynthesis.

As photosynthesis involves multiple processes it is hard to mimic, as charges need to be stored/accumulated, so they can produce enough energy to affect reactions, and can then be released on demand. In artificial photosynthesis, the aim is to split water to H_2 and O_2, and reduce carbon dioxide to produce fuels such as carbon monoxide and methanol.[61] However these reactions are multi-electron processes (table 1.2.1), and so in consequence are hard to control, as there is a need to prevent recombination of one electron / hole pair while another is generated. Therefore, for this to be successful there must be efficient separation of charges. In nature, this is achieved by a series of electron donors and acceptors held together by a protein structure, which facilitates this movement of charge.[60] Supramolecular structures are therefore an interesting possibility for mimicking photosynthesis, as they have the potential to create charge separated states which might perform useful onward reactions.

Table 1.2.1: *Multielectron reactions occurring in natural and artificial photosynthetic systems.*[62]

Energy storing reaction	**ne^-**
$2\ H_2O \rightarrow H_2 + H_2O_2$	2
$2\ H_2O \rightarrow 2\ H_2 + O_2$	4
$2\ H_2O + 2\ NAD^+ \rightarrow 2\ NADH/H^+ + O_2$	4
$CO_2 + 2\ H_2O \rightarrow CH_3OH + 3/2\ O_2$	6
$CO_2 + 2\ H_2O \rightarrow CH_4 + 2\ O_2$	8
$6\ CO_2 + 6\ H_2O \rightarrow C_6H_{12}O_6 + 6\ O_2$	24

1.2.2 Photophysical properties of coordination cages

In order for a coordination cage to be photophysically active, there must be at least one chromophoric component that absorbs light and has an excited state with a significant lifetime – whether this be through the metal ions or aromatic ligands.[63] The interest for this area is tremendous as a cage-based host/guest assembly provides a large array of chromophoric units surrounding a non-covalently bound guest molecule. This high concentration of photoactive units around a bound guest is special, as the close proximity might lead to interactions between the excited states of the individual components that could not be achieved in simpler covalently bonded assemblies. Applications arising from this new field may include solar energy harvesting, solar fuel generation and photocatalysis. For this, the ability to perform multiple photoinduced electron- transfer processes in a single assembly, with several light-harvesting units interacting with a single electron-accepting unit, is of fundamental importance.

1.2.2.1 Luminescent cages

The photophysical activity of cages is generally related to either the use of luminescent metal ions at the vertices, or the use of organic fluorophores as bridging ligands along the cage edges between the vertices; here we discuss a few examples of some different types of luminescent cages.[63]

Transition metals as luminophores in cages

The use of second or third row d-block transition metals with strong luminescence [Re(I), Ru(II), Os(II), Ir(III), Pt(II), etc.] as metal vertex units in cages has been widely researched.[63–68] However, an issue with the use of d-block metals is that as they are generally of either low-spin d^6 or d^8 electronic configuration, so they tend to be kinetically inert which precludes their use in the self-assembly reactions which normally require mild conditions; however a range of luminescent cages have been formed. Here we discuss some examples of three of the main transition metals used (ruthenium, iridium and osmium).

Beves et al. have employed the use of ruthenium(II) in preparing two cages based on $[Ru(2,2',6',2''\text{-terpyridine})_2]^{2+}$ units which have been furnished with pendant pyridyl groups; these inert components then form a cage by assembly of the pendant pyridyl units with additional square planar Pd(II) complexes (figure 1.2.2).[69] The photophysical properties of the initial ruthenium complexes are preserved on cage formation, with emission from the ^{3}MLCT excited state appearing at 640 nm, with lifetimes of between 1.2-1.3 ns.

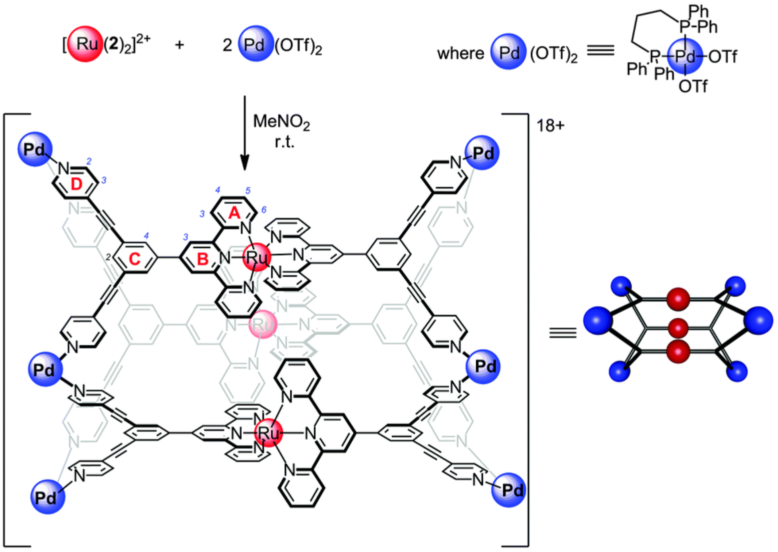

Figure 1.2.2: Ruthenium and palladium metal cornered cage. (Ref. 64 – Published by the Royal Society of Chemistry.)

This is an example of the use of pre-formed metal 'complexes-as-ligands' to self-assemble into a cage by addition of a labile metal ion (in this case palladium(II)). As previously discussed, the Ward group has also used this technique to produce mixed-metal cages with metal-based functionalities. In this case, Ru(II) and Os(II) ions have been used to lend their redox and luminescence properties to a cubic cage structure. An interesting point with both the ruthenium and osmium cages made by the Ward group (figure 1.2.3) is that the mononuclear Ru/Os tris-diimine complex units are statistically formed as a 3:1 mixture of *fac* and *mer* isomers, which is the exact combination needed to form this cubic cage. Additionally the cage $[Os_4Cd_4L_{12}](ClO_4)_{16}$ shows long-lived luminescence at 625 nm, which – together with its redox properties and the excited-state energy content – makes it a good excited-state photoelectron donor.[9,10]

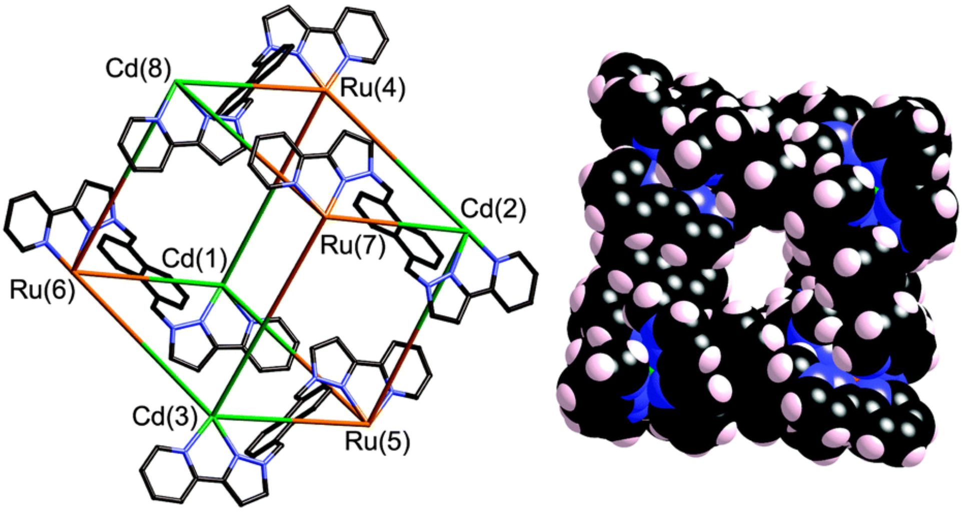

Figure 1.2.3: Crystal structure of the cubic $Ru_4Cd_4L_{12}$ cage, which is analogous to the Os(II) version. (Ref. 9 – Published by the Royal Society of Chemistry.)

As well as the use of Ru(II) and Os(II) metal ions as cage vertices, Lusby has reported an iridium(III) cage (figure 1.2.4) of octahedral shape, formed from six $[Ir(ppy_2)]^+$ units (ppy = 2-phenylatopyridine) and four 1,3,5-tricyanobenzene (tcb) faces.[70] This cage was shown to have enhanced luminescence properties compared to the mononuclear Ir(III) complex, which may be due to the inhibition of non-radiative deactivation pathways in the rigid cage.

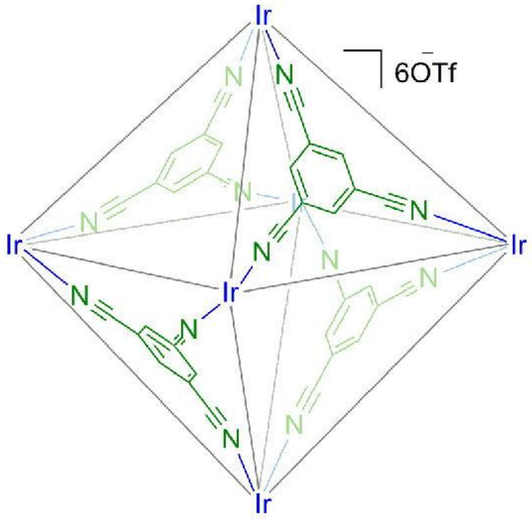

Figure 1.2.4: Lusby's $[(Ir(ppy)_2)_6(tcb)_4](OTf)_6$ octahedral cage.[70] (Adapted with permission from ref. 65. Copyright 2012 American Chemical Society.)

Lanthanides as luminophores in cages

Lanthanides are promising metal ions to be used in luminescent cages as they are labile, unlike low-spin d^6 and d^8 transition metals, and they can also be highly luminescent due to their f-f excited states.[63] The majority of cages formed in this way are tetrahedra, with many examples coming from Duan and He,[71,72] as well as the Hamacek group,[73] with examples of Eu(III) and Ce(IV) cages reported.

Another group that makes use of lanthanide ions in cages is that of Sun, using four Eu(III) ions as corners, with either 4 or 6 pyridine-2,6-dicarboxamide based ligands (figure 1.2.5).[19,74] These cages are highly fluorescent and have shown to be useful in sensing different nitroaromatic explosives, especially picric acid, which can by sensed using luminescence changes form the cage at the parts per billion (ppb) level.[75]

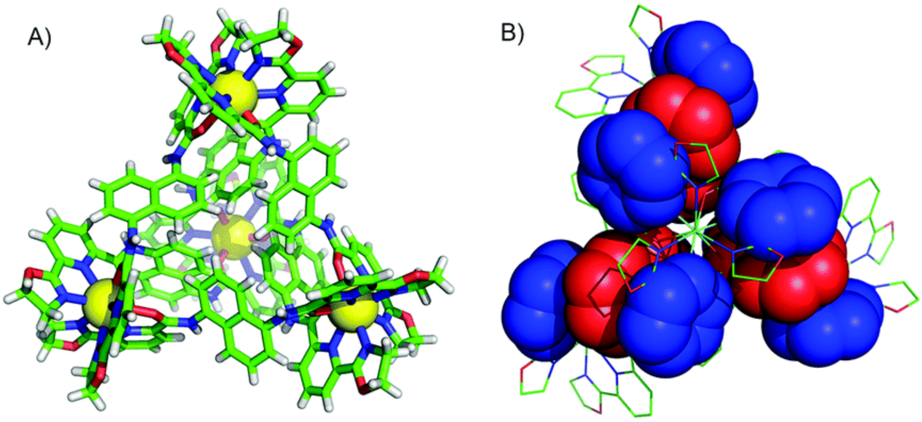

Figure 1.2.5: (a) X-ray crystal structure of a Eu_4L_6 cage and (b) highlight of the π-π stacking between the ligands of the cage. (Reproduced from ref. 70 with permission from The Royal Society of Chemistry.)

Organic ligands as fluorophores in cages

Organic fluorophores can provide a simple way of incorporating luminescence into cages.[63] When using organic fluorophores, it is essential that they are combined with metal ions that won't quench their fluorescence. The examples shown here give a range of organic ligands that make different shapes of cage and have different applications; sensing, photovoltaics and drug delivery.

Kuhn and co-workers have developed cages with rigid bis-monodentate pyridyl ligands and Pt/Pd metal (II) ions (figure 1.2.6).[35] These rigid ligands are highly fluorescent and can be used to encase cisplatin for anticancer applications; however upon cage formation the ligands' fluorescence is partly quenched. To combat this problem, so that cisplatin and other guests can be more easily sensed, the use of endo- and exo- functionalising groups have been used.[46,66] Endo- and exo- functionalisation has also been used by Crowley et al. who have used ‘click’ mechanisms to attach organic and metal based functional groups to Pd_2L_4 cages.[76,77]

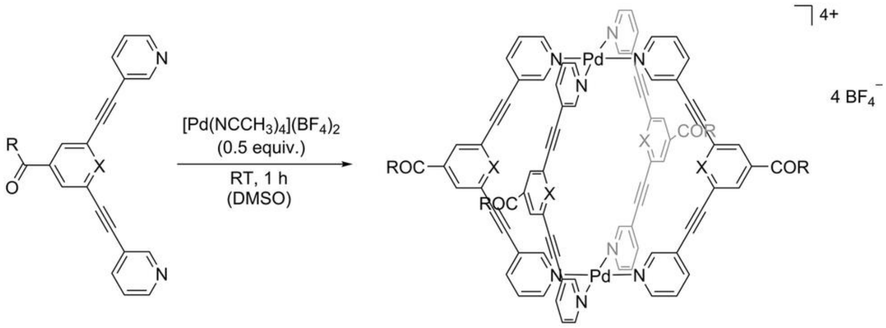

Compound	X	R	Yield [%]
a	CH	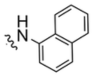	76
b	N	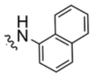	81
c	CH	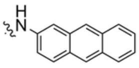	63
d	CH	OH	76

Figure 1.2.6: Kuhn group M_2L_4 cage with polyaromatic ligands. (Ref. 61 – Published by the Royal Society of Chemistry.)

Stang et al. have prepared Pt(II) cages with three types of component: eight Pt(II) acceptors, two tetraphenylethene (TPE) ligands and four linear dipyridyl ligands. The rigidity of the TPE ligands leads to strong luminescence and the ability to sense an amino acid.[20,78] The Nitschke group have additionally synthesised M_4L_6 cages based on Zn(II) or Fe(II) vertices and 4,4-difluoro-4-bora-3a,4a-diaza-s-indacene (BODIPY) and pyrene as the organic fluorophores (figure 1.2.7).[22] This collection of cages has then been tuned, along with its guest binding, to enhance its fluorescence emission and has been found to be able to sense anions: these cages can also produce white light emission by using a combination of host and guest luminophores with different emission colours.

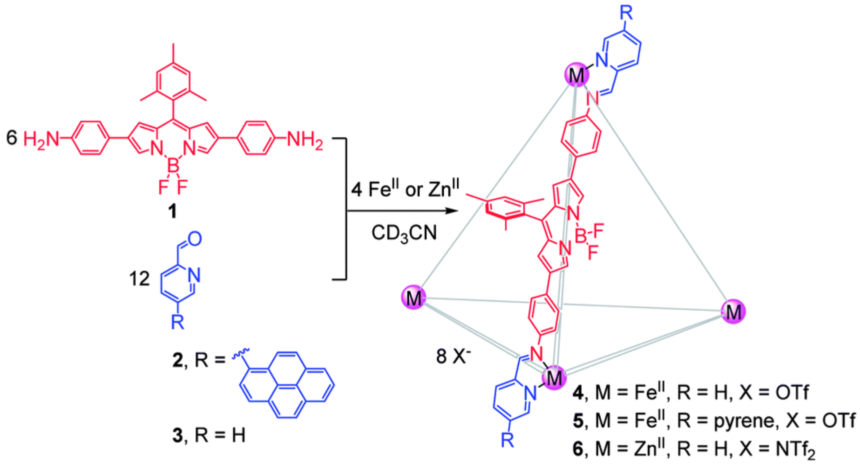

Figure 1.2.7: Self-assembly of tetrahedral M_4L_6 coordination cage from three components. (Reproduced from ref. 20 with permission from the Royal Society of Chemistry.)

Schwarzer and Clever have synthesised a set of group 10 palladium-based $[Pd_4L_8]^{8+}$ cages, with either donor and/or acceptor ligands in interpenetrated double cages (figure 1.2.8). These cages have then been studied through time-resolved IR (TRIR) spectroscopy and UV/Vis transient absorption (TA) spectroscopy.[79,80] They have been shown to form a charge-separated state when both donor and acceptor ligands are included in the architecture, as this close proximity allows for photoinduced ligand-to-ligand charge transfer (LLCT) to occur.[80] Through this unique work, they hope to apply these interpenetrated cages to photovoltaic devices and photo-/electrocatalysis.

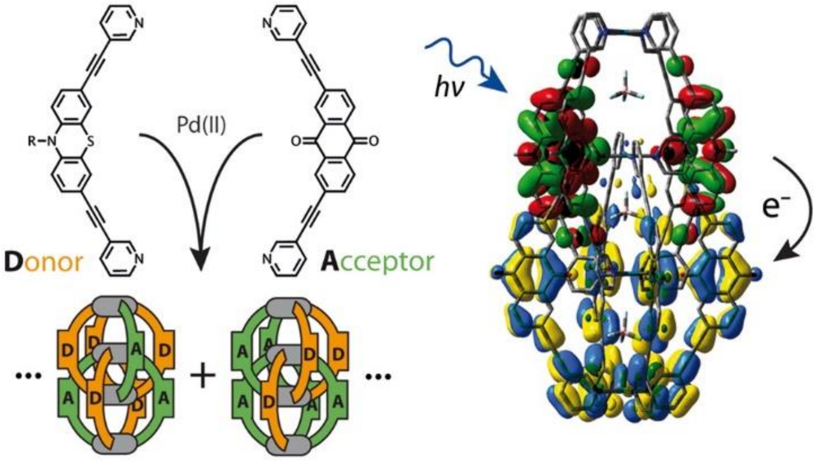

Figure 1.2.8: Mixed-ligand double cages, $[Pd_4D_mA_{8-m}]^{8+}$, with photoinduced electron transfer between the donor and acceptor ligands. (Reprinted with permission from ref. 75. Copyright 2016 American Chemical Society.)

1.2.2.2 Photoinduced processes involving both host and guest

Photoinduced reactions involving both the host and the guest are at the cutting edge of what self-assembled luminescent cages can do. This novel approach to electron and energy transfer in supramolecular assemblies merges the fields of supramolecular chemistry and photochemistry. Due to the high concentration of chromophores provided by the cage surrounding a bound guest, the potential for the photocatalysis of various reactions involving bound guests, using this unique ability to control spatial and kinetic factors associated with the electron transfer, is an exciting development for artificial photosynthesis.

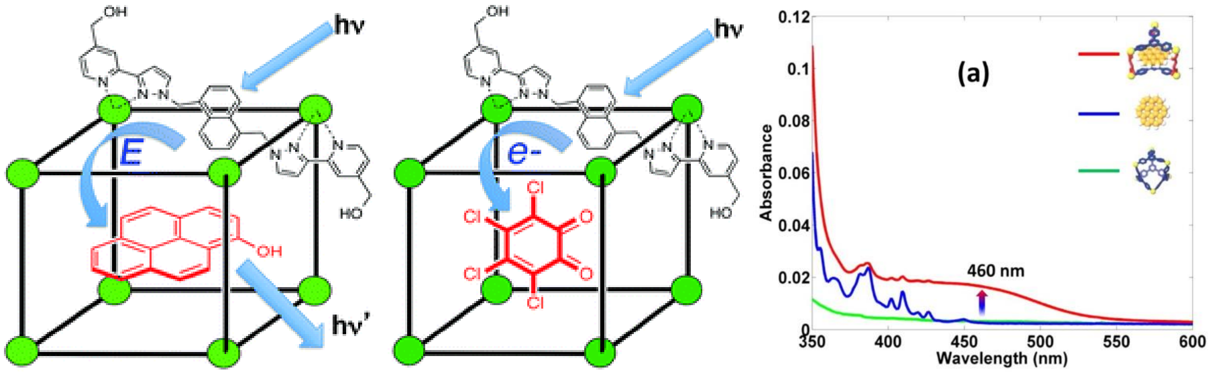

Figure 1.2.9: ***Left*****:** Ward group, energy- and electron transfer from napthyl group on ligand of cubic cage to guest compounds. (Ref. 76 – published by the Royal Society of Chemistry.) ***Right:*** Absorbance spectra of caged-coronene, free coronene, and empty trigonal prismatic host. (Reprinted with permission from ref. 77. Copyright 2015 American Chemical Society.)

The first step in this study is to study if any photoinduced interactions are occurring between a cage and guest. This can be studied using a variety of methods including transient absorption (TA) spectroscopy and time-resolved infra-red (TRIR) spectroscopy. A handful of research groups have managed to observe these processes: the Ward, Stang, Zysman-Colman and Nitschke groups, have successfully observed interactions in this way. The Ward group, as shown by figure 1.2.9 (left), have made cages based on Cd(II) vertices with fluorescent organic ligands spanning the edges, based on pyridyl groups with a naphthalene spacer group.[81] These cages are shown to exhibit energy or electron transfer from the ligand excited states to the guest, dependent on the properties of the guest. Stang and co-workers demonstrated enhanced emission of a guest coronene when bound in a Pt_6 cage.[82] The cage itself is non-emissive but due to the addition of the coronene, it then participates in a newly formed core-to-cage charge transfer state (figure 1.2.9 (right)).

The Zysman-Colman group prepared a luminescent $[Pd_6L_{12}](BF_4)_{12}$ cage with a ligand that undergoes thermally activated delayed fluorescence (TADF), that is made up of a 3,6-di(pyridine-4-yl)-9H-carboazole donor and benzophenone acceptor connected by a ligand scaffold.[83] The cage structure has been shown to encapsulate fluorescein and rose Bengal guests (figure 1.2.10); and it was shown that when fluorescein is the guest there is significant quenching of the emission from the ligand in the cage structure, suggesting that photoinduced electron transfer between the cage and the guest is occurring. However when rose Bengal is bound in the cage, there is not only quenching of the cage donor, but also enhancement of the emission of the rose Bengal guest, which suggests that an energy transfer process is happening from the cage to the guest.[83]

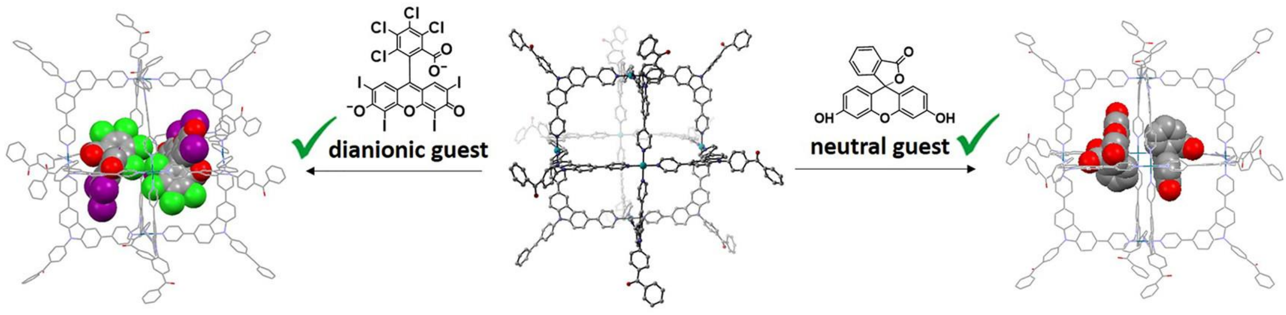

Figure 1.2.10: Luminescent $[Pd_6L_{12}]^{12+}$ cage that encapsulates dyes and displays cage-to-guest photoinduced electron/energy transfer. (Reprinted with permission from ref. 78. Copyright 2018 American Chemical Society.)

In addition to these studies, the Nitschke group have synthesised a set of $M^{II}_4L_6$ cages which contain a mixture of different bis-(aminophenyl) (BODIPY) moieties or pure BODIPY units (as seen in figure 1.2.7).[84] These BODIPY units are emissive and the cages can be synthesised with either Zn^{II} or Fe^{II} as the metal ion corners, and can encapsulate either C_{60} or C_{70} fullerenes.[84] The studies of the excited states of the cage alone proved that there are excitonic interactions between the ligands, which is due to there being electronic delocalization through the metal centres. However, when the fullerene units are encapsulated, host to guest photoinduced electron transfer occurs and this competes with the delocalization process.[84]

Moreover, a couple of groups have managed to utilise photoinduced electron transfer processes to perform hydrogen reduction. The Duan group have used a redox active Co(III) cage, which was paired with an organic dye as a guest; the encapsulation leads to electron transfer from the photosensitiser (dye) to the catalytic reduction site of the Co(III), which then has a high enough reduction potential to effect proton reduction and generate H_2 (figure 1.2.12).[85] The group has also performed some additional work on an Fe(II)-based cage which is set to encapsulate similar dyes and also perform photo-reduction.[86]

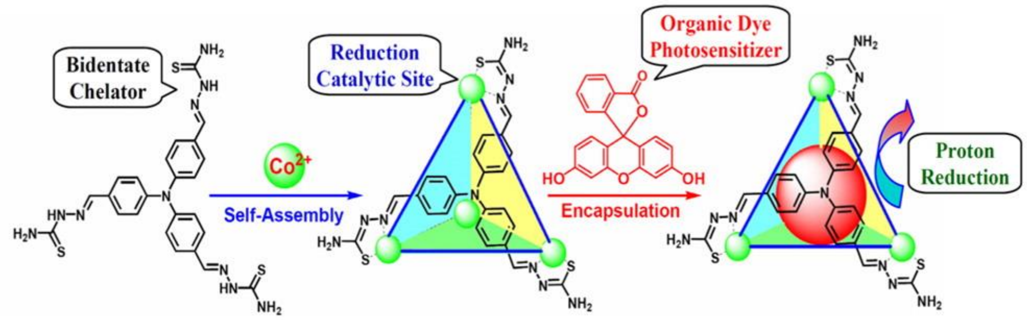

Figure 1.2.12: Scheme for the synthesis of a Co_4L_4 cage and encapsulation of dye for proton reduction. (Reprinted with permission from ref. 80. Copyright 2015 American Chemical Society.)

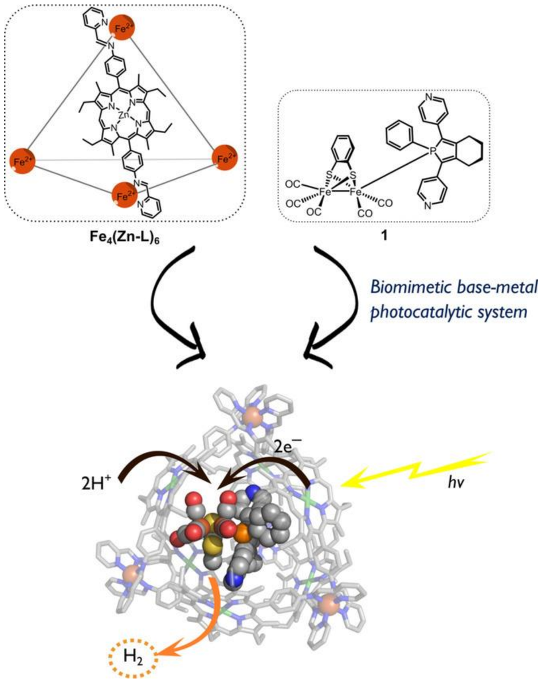

Figure 1.2.13: Photocatalytic proton reduction through [FeFe] hydrogenase encapsulated in Fe_4(Zn-L)$_6$ cage.[87]

The Reek group have used an $Fe_4(Zn\text{-}L)_6$ cage developed by the Nitschke group, containing a porphyrin-based ligand to produce molecular hydrogen (figure 1.2.13).[87] The cage encapsulates a synthetic pyridyl-phosphole-appended [FeFe] hydrogenase mimic. This was shown by TRIR studies to perform electron transfer from cage to guest; consequently, when in acidic solution and irradiated with visible light, it can catalyse proton reduction. The driving force for guest binding is the pyridyl/Zn(II)-porphyrin interaction.[87]

1.2.2.3 Photoinduced reactions of bound guests

Furthering these studies, a few groups have managed to perform photoinduced reactions on bound guests to achieve unique products. Su and Han have synthesised a novel $Pd_6(RuL_3)_8$ cage which utilises the Ru(II) units as photoactive centres.[88] They exploited the properties of this cage for hydrogen evolution, whereby the chromophoric ruthenium centre absorbs light whose energy cascades to the catalytic sites of the Pd(II) metal centres *via* electron transfer from MLCT states to an ILCT state, and then to an LMCT state which finally catalyses the reduction of water.[89] Recently these cages have also proved to show a regio- and enantioselective photodimerisation of 3-bromo-2-naphthol to give the *S*-enantiomer of the 1,4-coupled naphthol (figure 1.2.14).[90] This 1,4-coupling is unusual but is promoted by the confinement in the cage: it is however unclear whether the cage plays a part in the electron transfer process or whether it just confines the guest in a chiral environment.

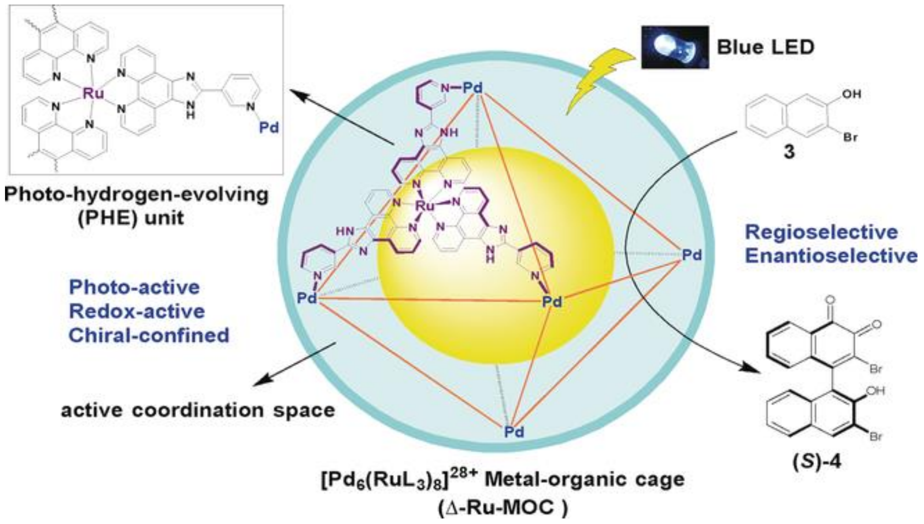

Figure 1.2.14: Regio- and enantioselective photodimerisation of 3-bromo-2-naphthol with $[Pd_6(RuL_3)_8]$.[90]

Fujita and his group have also shown evidence of a system in which both cage and guest are involved in photoinduced electron transfer. Figure 1.2.15 shows how the triazine chromophore of the cage is excited and increases its oxidative capability, at which point an electron is transferred to the excited-state of the cage from the adamantane group which forms a radical cation. This adamantane radical cation can then react with water or oxygen to give an oxidised alcohol or hydroperoxide product.[91] The Fujita group have more recently shown a unique reaction of various cyclopropane containing guest molecules in which a methylene group is cleaved from the ring, leading to an unnatural alkene molecule.[92] This occurs in a similar way to the reaction with adamantane: under UV irradiation, the cyclopropane guest transfers an electron to the photo-excited host, and then this guest radical reacts further to produce the new product molecule. They found that this reaction only worked if the cyclopropane unit was adjacent to either an alkane or a phenyl ring.[92]

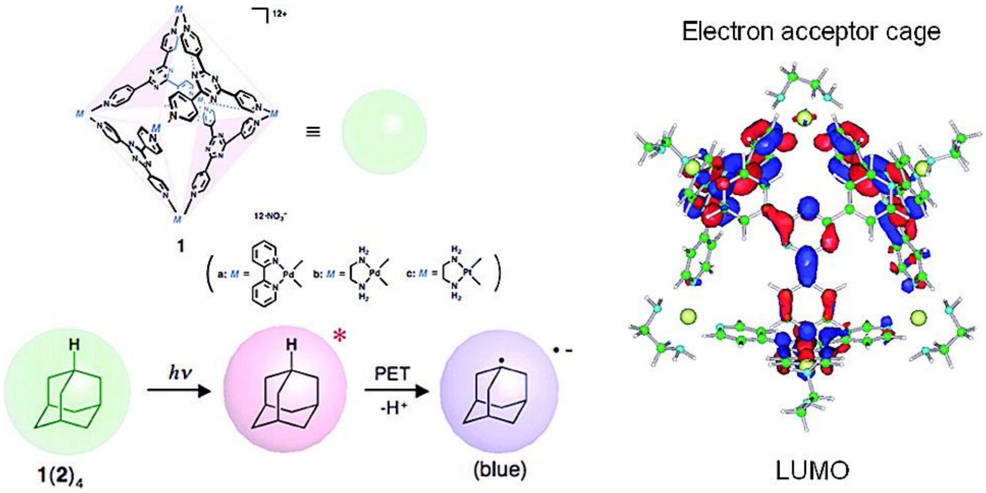

Figure 1.2.15: Structure of Fujita's M_6L_4 cage and proposed PET mechanism for the photooxidation of adamantane in the cavity. (Reprinted with permission from ref. 86. Copyright 2009 American Chemical Society.)

Finally, Raymond and co-workers used a Ga_4L_6 cage for which photoinduced electron transfer triggered pericyclic rearrangement of cinnamylammonium guest.[93] This rearrangement, like the above demethylation and photodimerisation, requires both guest encapsulation and electron transfer between cage and guest to occur (figure 1.2.16).

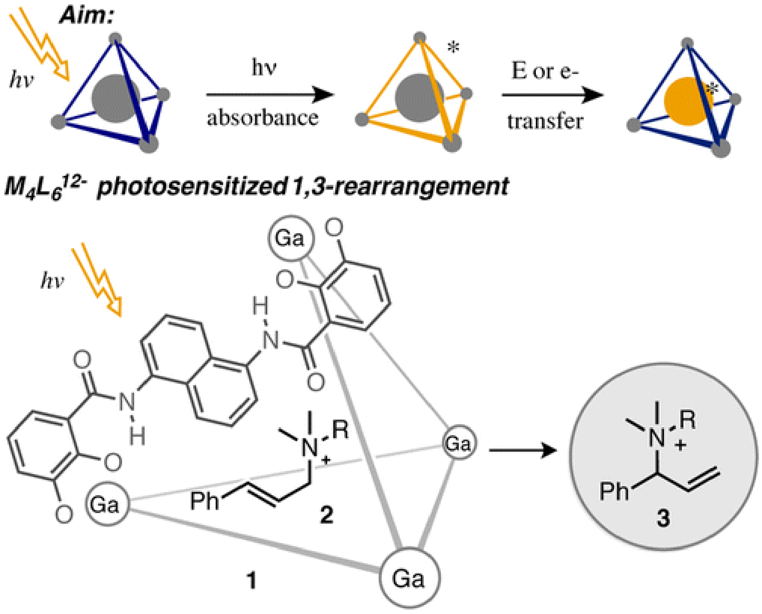

Figure 1.2.16: Photosensitization of an allylic 1,3-rearrangement of encapsulated cinnamylammonium guest using a $M_4L_6^{12-}$ cage. (Reprinted with permission from ref. 88. Copyright 2015 American Chemical Society).

These examples of photoinduced reactions of bound guests and photointeractions between host and guest are the state of the art in cage photochemistry. They show the potential of new applications of cages in hydrogen evolution, the design of photovoltaics and the catalysis of unique chemical reactions. This thesis aims to build on these ideas through the synthesis of a water-soluble osmium-based cage that can participate in photoinduced electron transfer and can photocatalyse unique reactions, for light-harvesting and photocatalysis applications.

1.3 References

1 J. W. Steed and J. L. Atwood, *Supramolecular Chemistry*, 2009.

2 J. Rebek, *Proc. Natl. Acad. Sci. U. S. A.*, 2009, **106**, 10423–4.

3 D. Philp and J. F. Stoddart, *Angew. Chemie Int. Ed. English*, 1996, **35**, 1154–1196.

4 L. A. Pray, *Nat. Educ.*, 2008, **1**, 100.

5 R. W. Saalfrank, A. Stark, K. Peters and H. G. von Schnering, *Angew. Chemie Int. Ed.*, 1988, **27**, 851–853.

6 D. Fujita, Y. Ueda, S. Sato, N. Mizuno, T. Kumasaka and M. Fujita, *Nature*, 2016, **540**, 563–566.

7 C. J. Brown, F. D. Toste, R. G. Bergman and K. N. Raymond, *Chem. Rev.*, 2015, 3012–3035.

8 A. J. Metherell and M. D. Ward, *Chem. Commun.*, 2014, **50**, 10979–82.

9 A. J. Metherell and M. D. Ward, *Chem. Commun.*, 2014, **50**, 6330–2.

10 A. B. Wragg, A. J. Metherell, W. Cullen and M. D. Ward, *Dalt. Trans.*, 2015, **44**, 17939–17949.

11 A. J. Metherell and M. D. Ward, *Chem. Sci.*, 2015, 910–915.

12 A. Stephenson, D. Sykes and M. D. Ward, *Dalt. Trans.*, 2013, **42**, 6756.

13 C. J. Pedersen, *J. Am. Chem. Soc.*, 1967, **89**, 7017–7036.

14 D. J. Cram and J. M. Cram, *Science (80-.)*.

15 E. Fischer, *Eur. J. Inorg. Chem.*, 1894, **27**, 2985–2993.

16 D. E. Koshland, *Proc. Natl. Acad. Sci. U. S. A.*, 1958, **44**, 98–104.

17 D. E. Koshland, *Angew. Chemie Int. Ed.*, 1995, **33**, 2375–2378.

18 C. J. Pedersen, *J. Am. Chem. Soc*, 1967, **2**, 209.

19 X. Z. Li, L. P. Zhou, L. L. Yan, D. Q. Yuan, C. S. Lin and Q. F. Sun, *J. Am. Chem. Soc.*, 2017, **139**, 8237–8244.

20 M. Zhang, M. L. Saha, M. Wang, Z. Zhou, B. Song, C. Lu, X. Yan, X. Li, F. Huang, S. Yin and P. J. Stang, *J. Am. Chem. Soc.*, 2017, jacs.6b12536.

21 C. L. Liu, R. L. Zhang, C. S. Lin, L. P. Zhou, L. X. Cai, J. T. Kong, S. Q. Yang, K. L. Han and Q. F. Sun, *J. Am. Chem. Soc.*, 2017, **139**, 12474–12479.

22 P. P. Neelakandan, A. Jiménez and J. R. Nitschke, *Chem. Sci.*, 2014, **5**, 908.

23 P. D. Frischmann, V. Kunz and F. Würthner, *Angew. Chemie - Int. Ed.*, 2015, **54**, 7285–7289.

24 A. Pappalardo, R. Puglisi and G. T. Sfrazzetto, *Catalysts*, 2019, **9**, 630.

25 C. M. Hong, R. G. Bergman, K. N. Raymond and F. D. Toste, *Acc. Chem. Res.*, 2018, **51**, 2447–2455.

26 C. J. Hastings, R. G. Bergman and K. N. Raymond, *Chem. - A Eur. J.*, 2014, **20**, 3966–3973.

27 Y. Fang, J. A. Powell, E. Li, Q. Wang, Z. Perry, A. Kirchon, X. Yang, Z. Xiao, C. Zhu, L. Zhang, F. Huang and H.-C. Zhou, *Chem. Soc. Rev.*, , DOI:10.1039/C9CS00091G.

28 D. Fiedler, R. G. Bergman and K. N. Raymond, *Angew. Chemie - Int. Ed.*, 2004, **43**, 6748–6751.

29 C. Tan, D. Chu, X. Tang, Y. Liu, W. Xuan and Y. Cui, *Chem. - A Eur. J.*, 2019, **25**, 662–672.

30 P. Mal, B. Breiner, K. Rissanen and J. R. Nitschke, *Science*, 2009, **324**, 1697–9.

31 M. Yoshizawa, J. K. Klosterman and M. Fujita, *Angew. Chemie - Int. Ed.*, 2009, **48**, 3418–3438.

32 M. D. Ward and P. R. Raithby, *Chem. Soc. Rev.*, 2013, **42**, 1619–1636.

33 J. E. M. Lewis, E. L. Gavey, S. A. Cameron and J. D. Crowley, *Chem. Sci.*, 2012, **3**, 778–784.

34 W. Cullen, S. Turega, C. A. Hunter and M. D. Ward, *Chem. Sci.*, 2015, **6**, 625–631.

35 F. Kaiser, A. Schmidt, W. Heydenreuter, P. J. Altmann, A. Casini, S. A. Sieber and F. E. Kuhn, *Eur. J. Inorg. Chem.*, 2016, **2016**, 5181.

36 M. D. Pluth and K. N. Raymond, *Chem. Soc. Rev.*, 2007, **36**, 161–171.

37 H. S. Frank and M. W. Evans, *J. Chem. Phys.*, 1945, **13**, 507–532.

38 M. Yoshizawa, T. Kusukawa, M. Kawano, T. Ohhara, I. Tanaka, K. Kurihara, N. Niimura and M. Fujita, *J. Am. Chem. Soc.*, 2005, **127**, 2798–2799.

39 F. Biedermann, W. M. Nau and H. J. Schneider, *Angew. Chemie - Int. Ed.*, 2014, **53**, 11158–11171.

40 A. J. Metherell, W. Cullen, N. H. Williams and M. D. Ward, *Chem. - A Eur. J.*, 2017, **24**, 1554–1560.

41 S. Mecozzi and J. Rebek, *Chem. - A Eur. J.*, 1998, **4**, 1016–1022.

42 J. Rebek, *Acc. Chem. Res.*, 2009, **42**, 1660–8.

43 J. J. Christensen, J. O. Hill and R. M. Izatt, *Science*, 1971, **174**, 459–467.

44 R. M. Izatt, J. Howard Rytting, D. P. Nelson, B. L. Haymore and J. J. Christensen, *Science (80-.).*, 1969, **164**, 443–444.

45 P. Thordarson, *Chem. Soc. Rev.*, 2011, **40**, 1305–1323.

46 A. Schmidt, M. Hollering, M. Drees, A. Casini and F. E. Kühn, *Dalt. Trans.*, 2016, 8556–8565.

47 C. G. P. Taylor, J. R. Piper and M. D. Ward, *Chem. Commun.*, 2016, **52**, 6199–6338.

48 W. Cullen, M. C. Misuraca, C. A. Hunter, N. H. Williams and M. D. Ward, *Nat Chem.*, 2016, **8**, 1–6.

49 C. J. Hastings, M. D. Pluth, R. G. Bergman and K. N. Raymond, *J. Am. Chem. Soc.*, 2010, **132**, 6938–6940.

50 V. Mouarrawis, R. Plessius, J. I. van der Vlugt and J. N. H. Reek, *Front. Chem.*, 2018, **6**, 1–20.

51 C. J. Brown, R. G. Bergman and K. N. Raymond, *J. Am. Chem. Soc.*, 2009, **131**, 17530–17531.

52 W. Cullen, A. J. Metherell, A. B. Wragg, C. G. P. Taylor, N. H. Williams and M. D. Ward, *J.*

Am. Chem. Soc., 2018, jacs.7b11334.

53 T. Murase, S. Peschard, S. Horiuchi, Y. Nishioka and M. Fujita, *Supramol. Chem.*, 2011, **23**, 199–208.

54 Y. Ueda, H. Ito, D. Fujita and M. Fujita, *J. Am. Chem. Soc.*, 2017, **139**, 6090–6093.

55 J. Jiao, Z. Li, Z. Qiao, X. Li, Y. Liu, J. Dong, J. Jiang and Y. Cui, *Nat. Commun.*, 2018, **9**, 1–8.

56 J. Jiao, C. Tan, Z. Li, Y. Liu, X. Han and Y. Cui, *J. Am. Chem. Soc.*, 2018, **140**, 2251–2259.

57 P. Ceroni and V. Balzani, in *The Exploration of Supramolecular Systems and Nanosructures by Photochemical Techniques*, 2012, vol. 78, pp. 209–225.

58 M. R. Wasielewski, *Chem. Rev.*, 1992, **92**, 435–461.

59 Y. Xu, A. Li, T. Yao, C. Ma, X. Zhang, J. H. Shah and H. Han, *ChemSusChem*, 2017, **10**, 4277–4305.

60 J. Barber, *Chem. Soc. Rev.*, 2009, **38**, 185–96.

61 J. J. Concepcion, R. L. House, J. M. Papanikolas and T. J. Meyer, *Proc. Natl. Acad. Sci. U. S. A.*, 2012, **109**, 15560–15564.

62 G. Knör, *Coord. Chem. Rev.*, 2015, **304**–**305**, 102–108.

63 M. D. Ward, in *Comprehensive Supramolecular Chemistry II*, ed. J. L. Atwood, Elsevier, Oxford, 2017, pp. 357–371.

64 D. Rota Martir and E. Zysman-Colman, *Chem. Commun.*, 2019, **55**, 139–158.

65 L. Xu, Y. X. Wang and H. B. Yang, *Dalt. Trans.*, 2014, **44**, 867–890.

66 A. Schmidt, M. Hollering, J. Han, A. Casini and F. E. Kühn, *Dalt. Trans.*, 2016, 4–7.

67 D. Rota Martir, D. Escudero, D. Jacquemin, D. B. Cordes, A. M. Z. Slawin, H. A. Fruchtl, S. L. Warriner and E. Zysman-Colman, *Chem. - A Eur. J.*, 2017, **23**, 14358–14366.

68 R. Chakrabarty, P. S. Mukherjee and P. J. Stang, *Chem. Rev.*, 2011, **111**, 6810–6918.

69 J. Yang, M. Bhadbhade, W. A. Donald, H. Iranmanesh, E. G. Moore, H. Yan and J. E. Beves, *Chem. Commun.*, 2015, **51**, 4465–4468.

70 O. Chepelin, J. Ujma, X. Wu, A. M. Z. Slawin, M. B. Pitak, S. J. Coles, J. Michel, A. C. Jones, P. E. Barran and P. J. Lusby, *J. Am. Chem. Soc.*, 2012, **134**, 19334–19337.

71 Y. Jiao, J. Wang, P. Wu, L. Zhao, C. He, J. Zhang and C. Duan, *Chem. - A Eur. J.*, 2014, **20**, 2224–2231.

72 C. He, J. Wang, P. Wu, L. Jia, Y. Bai, Z. Zhang and C. Duan, *Chem. Commun.*, 2012, 11880–11882.

73 B. El Aroussi, L. Guénée, P. Pal and J. Hamacek, *Inorg. Chem.*, 2011, **50**, 8588–8597.

74 L.-L. Yan, C.-H. Tan, G.-L. Zhang, L.-P. Zhou, J.-C. Bünzli and Q.-F. Sun, *J. Am. Chem. Soc.*, 2015, **137**, 8550–5.

75 C.-L. Liu, L.-P. Zhou, D. Tripathy and Q.-F. Sun, *Chem. Commun.*, 2017, **53**, 2459–2462.

76 J. E. M. Lewis, A. B. S. Elliott, C. J. McAdam, K. C. Gordon and J. D. Crowley, *Chem. Sci.*, 2014, 1833.

77 A. B. S. Elliott, J. E. M. Lewis, H. Van Der Salm, C. J. McAdam, J. D. Crowley and K. C. Gordon, *Inorg. Chem.*, 2016, **55**, 3440–3447.

78 X. Yan, T. R. Cook, P. Wang, F. Huang and P. J. Stang, *Nat. Chem.*, 2015, **7**, 342–348.

79 J. Ahrens, M. Frank, G. H. Clever and D. Schwarzer, *Phys. Chem. Chem. Phys.*, 2017, **19**, 13596–13603.

80 M. Frank, J. Ahrens, I. Bejenke, M. Krick, D. Schwarzer and G. H. Clever, *J. Am. Chem. Soc.*, 2016, **138**, 8279–8287.

81 J. R. Piper, L. Cletheroe, C. G. P. Taylor, A. J. Metherell, J. A. Weinstein, I. V. Sazanovich and M. D. Ward, *Chem. Commun.*, 2017, **53**, 408–411.

82 Y. Yang, J.-S. Chen, J.-Y. Liu, G.-J. Zhao, L. Liu, K.-L. Han, T. R. Cook and P. J. Stang, *J.*

Phys. Chem. Lett., 2015, **6**, 1942–7.

83 D. R. Martir, A. Pizzolante, D. Escudero, D. Jacquemin, S. L. Warriner and E. Zysman-Colman, *ACS Appl. Energy Mater.*, 2018, **1**, 2971–2978.

84 A. J. Musser, P. P. Neelakandan, J. M. Richter, H. Mori, R. H. Friend and J. R. Nitschke, *J. Am. Chem. Soc.*, 2017, **139**, 12050–12059.

85 X. Jing, C. He, Y. Yang and C. Duan, *J. Am. Chem. Soc.*, 2015, **137**, 3967–3974.

86 L. Yang, X. Jing, C. He, Z. Chang and C. Duan, *Chem. - A Eur. J.*, 2016, 18107–18114.

87 S. S. Nurttila, R. Becker, J. Hessels, S. Woutersen and J. N. H. Reek, *Chem. - A Eur. J.*, 2018, **24**, 16395–16406.

88 K. Li, L. Y. Zhang, C. Yan, S. C. Wei, M. Pan, L. Zhang and C. Y. Su, *J. Am. Chem. Soc.*, 2014, **136**, 4456–4459.

89 S. Chen, K. Li, F. Zhao, L. Zhang, M. Pan, Y.-Z. Fan, J. Guo, J. Shi and C.-Y. Su, *Nat. Commun.*, 2016, **7**, 13169.

90 J. Guo, Y.-W. Xu, K. Li, L.-M. Xiao, S. Chen, K. Wu, X.-D. Chen, Y.-Z. Fan, J.-M. Liu and C.-Y. Su, *Angew. Chemie Int. Ed.*, 2017, **100191**, 3852–3856.

91 Y. Furutani, H. Kandori, M. Kawano, K. Nakabayashi, M. Yoshizawa and M. Fujita, *J. Am. Chem. Soc.*, 2009, **131**, 4764–4768.

92 W. Cullen, H. Takezawa and M. Fujita, *Angew. Chemie - Int. Ed.*, 2019, **58**, 9171–9173.

93 D. M. Dalton, S. R. Ellis, E. M. Nichols, R. A. Mathies, F. Dean Toste, R. G. Bergman and K. N. Raymond, *J. Am. Chem. Soc.*, 2015, **137**, 10128–10131.

Chapter 2

Synthesis, Characterisation and Guest Binding of an Os(II) Coordination Cage

2.1 Introduction

The Ward group have synthesised a large variety of cages in the past few years, with various different metals and pyridyl-pyrazole based bridging ligands.[1,2,3] The cage that has offered the most functionality and stability has been the cubic-shaped cage, which contains 8 metal ions at the vertices and 12 ligand molecules spanning each of the edges. Initially this cage contained 8 Co(II) or 8 Cd(II) corners, along with the ligand (L^{nap}) in which the two pyridyl pyrazole units are separated by a 1,5-dimethyl naphthalene spacer. 16 counter ions balance the 16^+ charge of the coordinated metal ions.[4,3] This cage has many uses as it has a large enough cavity (407 $Å^3$) to encapsulate guests and a 4 Å wide portal on each of the six faces, allowing guest molecules to leave and enter. This cage has the additional bonus of being very stable in solution even over a wide pH range.[5] These properties allow the strength of different guest binding to be measured.

A limitation of this cage is poor water solubility. Solubility in water is desirable as it allows guests to bind strongly *via* the hydrophobic effect. In contrast binding in organic solvents e.g. acetonitrile, was found to be driven by hydrogen bonding interactions with the cage interior surface and is therefore much weaker.[6,7] To counteract this problem, a modified cage was synthesised where the ligand had externally-directed CH_2OH groups attached to the pyridyl ring.[6] These 24 OH groups allowed the cage to dissolve in water. Since then the group has also found that changing the counter ion associated with the cage from BF_4 or ClO_4 to Cl leads to a water-soluble cage.[8] Having optimised guest binding in this way, the next aim was to incorporate some functionality into the cage itself, rather than it being just a vessel for guest binding. Some work in the group has included the use of the Cd(II)-based cage to perform photoinduced electron or energy transfer to bound guests - through the excited-state properties of the naphthalene spacer in the ligands of the cage.[9] In addition to this Os(II) and Ru(II)-based cages have also been synthesised to incorporate transition metal properties into the cage e.g. photophysical and redox capabilities.[10–12]

As discussed in chapter 1, kinetically inert transition metals such as Ru(II) and Os(II) need to be incorporated into cage structures in a stepwise manner to generate mixed-metal systems, as they are highly kinetically inert. However, cage formation depends on lability for self assembly to occur. Stemming from this, a group of Os(II) and Ru(II) cages were synthesised, as depicted in scheme 2.1.1. Initial studies of their redox and photophysical properties was undertaken. This worked showed that these cages retain the redox activity of the separate metal centres, and the Os(II) containing cages additionally show the characteristic metal centred phosphorescence of a ^{3}MLCT excited state.

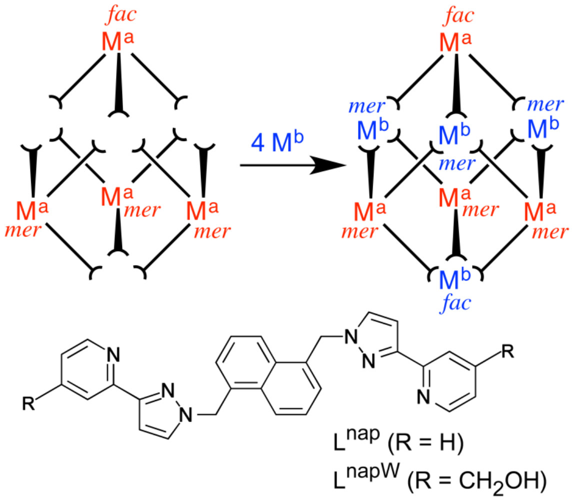

Scheme 2.1.1: The stepwise synthesis of heterometallic cubic cages: combination of four pre-formed, kinetically inert $[(M^a)(L^{nap})_3]^{2+}$ units (M^a = Ru, Os) with four labile ions $(M^b)^{2+}$ (M^b = Co, Cd) to give $[(M^a)_4(M^b)_4(L^{nap})_{12}]^{16+}$.

The work in this chapter looks at exploiting these useful metal-centred properties, as well as evaluating guest binding of the new transition metal cage complexes. In this study, the focus is on Os(II) over the more common Ru(II), as previous work showed that the Os(II) tris(pyrazolyl-pyridine) unit has a long-lived ^{3}MLCT excited state and is a good photo-electron donor. In contrast the equivalent Ru(II) complexes show no useful photophysical activity, due to the ^{3}MLCT and dd states being similar in energy, so provide a rapid deactivation pathway. The Os(II) complex, has a higher crystal field splitting due to Os(II) being a third-row ion and having more extended d-orbitals (5d instead of 4d), so the dd state is too high in energy to deactivate the ^{3}MLCT state - which is therefore long-lived and phosphorescent. This chapter focuses on the synthesis of a water soluble version of an Os_4Zn_4 based cubic cage and characterisation of the redox/photophysical properties, as well as quantifying guest binding within the cavity.

2.2 Results and Discussion

2.2.1 Synthesis and characterisation

To meet the aims of synthesising and characterising a water soluble cubic cage, incorporating Os(II) units, the mononuclear coordination 'corner complex' needs to be based on ($[Os(L^{nap})_3]X_2$ units) (where 'L^{nap}' is a bidentate pyrazole-pyridine chelating ligand). To do this, each Os(II) ion is coordinated to three bis-bidentate ligands *via* one terminus of each ligand, with each ligand having a pendant bidentate binding site: this kinetically inert 'complex ligand' can then go on to propagate the self-assembly process using coordination of the pendant sites to a labile metal ion. Figure 2.2.1 shows the target complex, which consists of three identical bis-bidentate ligands that are composed of two chelating pyridyl-pyrazole units bonded to a naphthalene-1,5-diyl aromatic spacer, which are complexed to an Os(II) ion. The ligand was synthesised according to a literature method in a high yield of 83%;[3] mononuclear $[Os(L^{nap})_3]X_2$ was also initially prepared according to a literature method, however the yield was very low, at 3%.[11] This synthesis involved the reaction of $OsCl_3.6H_2O$ with five equivalents of L in ethylene glycol at reflux for 3 days, followed by anion metathesis, and purification through column chromatography. However due to the low yield, the reaction was first optimised by use of a microwave reactor, which – as well as increasing the yield to 13% – meant that the reaction time also decreased to 6 hours.

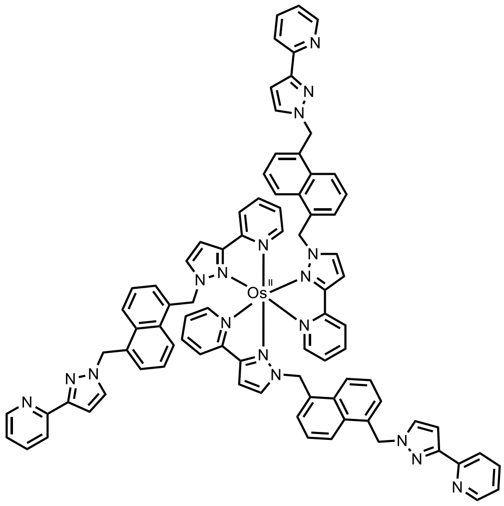

Figure 2.2.1: Diagram depicting the $[OsL_3]^{2+}$ 'corner' complex.

Despite the increased yield, 13% was still not optimum so different avenues were pursued to try to increase this. It was noted that the majority of side-products being formed were expected to be multi-nuclear complexes with a high charge as they had a high affinity to silica compared to the pure mononuclear complex with only a 2+ charge; characterisation of these by-products was attempted, however was not successful. Formation of polynuclear complexes implies that some ligands are binding two Os(II) ions, despite a 5:1 ligand:Os(II) ratio being used. In consequence of this, synthesis of the mononuclear complex was attempted via a dropping method by which a dilute solution of the starting reagent, $OsCl_3.6H_2O$ in ethylene glycol, was slowly added over 6 hours into a solution of excess ligand and left to reflux for 12 hours. This method ensures that ligand is always in large excess and should minimise formation of undesired dinuclear Os(II) complexes. This improved the yield to 24 %, which is the same as the previously published figure.[11] Figure 2.2.2 is the ^{1}H NMR spectra of $[Os(L^{nap})_3](PF_6)_2$ and shows the 1:3 ratio of *fac* and *mer* isomers, as depicted by the H^6 protons on the pyridyl group. As a consequence to this ratio, scheme 2.1.1, shows that a 1:3 fac:mer ratio is exactly what is required to form the cubic cage structure, in which the 3 *mer* OsL_3 units and 1 *fac* unit, are accompanied by 3 labile Zn(II) *mer* corners and 1 *fac* corner.

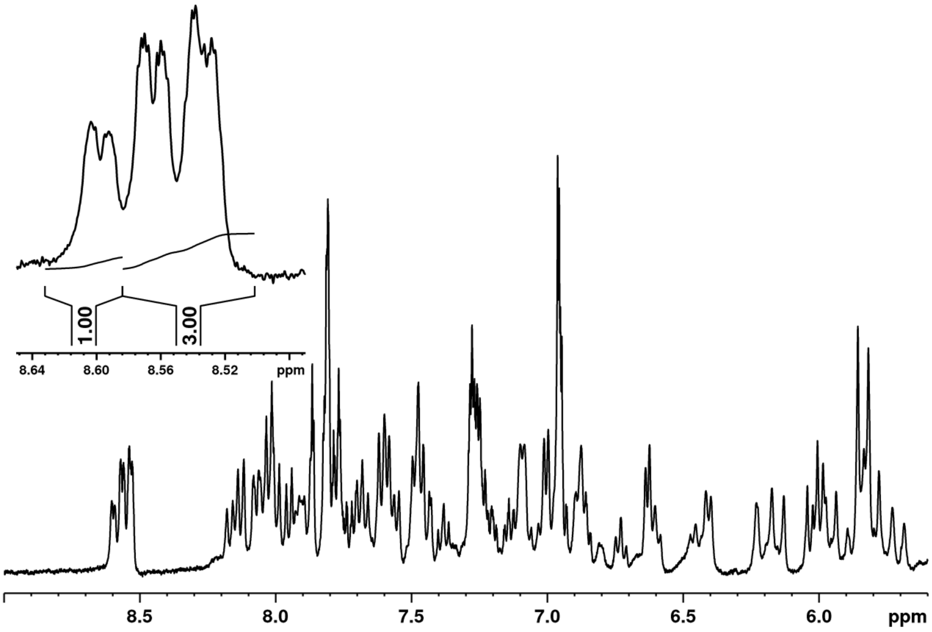

Figure 2.2.2: ^{1}H NMR spectrum of the H^6 protons on the pyridyl group of L^{nap} in the $[Os(L^{nap})_3](PF_6)_2$ in CD_3CN.

Once isolated, the $[Os(L^{nap})_3](PF_6)_2$ molecule underwent a self-assembly reaction with $Zn(ClO_4)_2$ to form the complete cage structure. This reaction can be achieved in a couple of hours by stirring the reagents in nitromethane, under ambient conditions; which is then followed by slow crystallization from nitromethane/diisopropyl ether to produce deep red X-ray quality crystals; with the only product formed being the $[Os_4Zn_4(L^{nap})_{12}](ClO_4)_{16}$ cubic cage structure shown in figure 2.2.3.

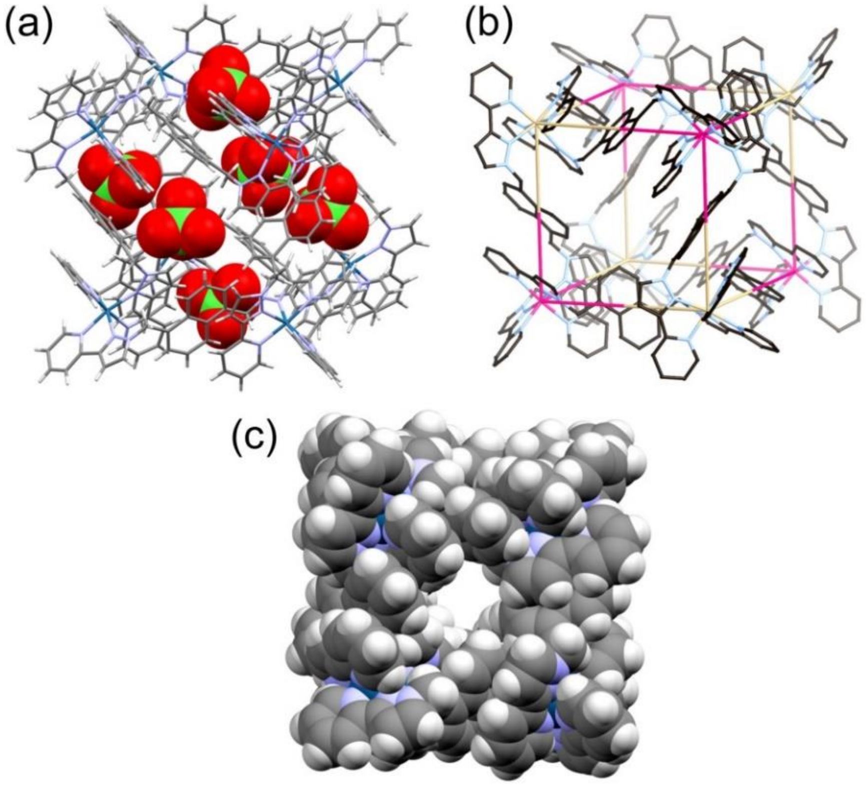

Figure 2.2.3: Crystal structures of $[Os_4Zn_4(L^{nap})_{12}](ClO_4)_{16}$. (a) 6 $[ClO_4]^-$ ions occupying each window (b) Os(II) corners in pink and Zn(II) corners in beige (c) space-filling view.

The crystals obtained from the liquid-liquid diffusion were analysed through X-ray crystallography. Figure 2.2.3 shows the structure of the cage that was determined by Alexander Metherell (University of Sheffield). This structure is similar to the approximately cubic structure of the other $[M_8L_{12}]^{16+}$ cages which have the same bridging ligand (L^{nap}) and the same 8:12 ratio of metals to ligands.[12,11] There is also similar extensive inter-ligand π-stacking with alternating arrays of electron-deficient (pyrazolyl-pyridine) and electron-rich (naphthyl) groups, with metal–metal separations of 11.2 and 11.3 Å along the edges of the cube. In this case, like the published case of $[Ru_4Co_4(L^{nap})_{12}](BF_4)_{16}$, the metal sites are indistinguishable crystallographically, as the cage is disordered over the two orientations.[11] This means that the metal occupancy at each site is 50%, which is probably due to Os(II)-N and Zn(II)-N bond distances being similar (Metal-N: mer: 2.08–2.16 Å, fac: 2.15 and 2.17 Å). As shown by structure (a), the ClO_4^- ions are located in the windows of the faces, with no guest molecule in the cavity. The S_6 symmetry arises from the arrangement of two *fac* and six *mer* tris-chelate sites such that the complex has both a C_3 axis and an inversion centre.

To adapt the cage to being water-soluble, $[Os_4Zn_4(L^{nap})_{12}](ClO_4)_{16}$ was converted from the perchlorate salt to the chloride salt, by stirring a suspension of the cage in water, with an excess of Dowex anion exchange resin, to give a red aqueous solution of $[Os_4Zn_4(L^{nap})_{12}]Cl_{16}$ (**Os•Zn)**. Unlike previous Os(II)-based cages synthesised by the group, Zn(II) is used as the second labile metal instead of Cd(II), as anion exchange with chloride to give the water-soluble chloride form of the cage does not result in decomposition. In contrast, the isostructural Os_4Cd_4 cage, that has been published previously, decomposes following anion exchange to the chloride salt, possibly due to the high affinity of chloride for Cd(II). Additionally, Cd and Zn are both d^{10} so don't quench the excited state of the Os(II) vertices, whereas Co(II) (d^7) does. Also, as described in section 2.1, the alternative ligand, L^w, used to infer water solubilty on the cages could not be used, as the $-CH_3OH$ groups do not remain intact during the $[Os(L^{nap})_3](PF_6)_2$ synthesis, which requires temperatures of 200 °C.

Characterisation of the cage by ^1H NMR spectroscopy is difficult due to the large number of proton environments. The low symmetry of the complex gives four independent ligands with no internal symmetry, generating 88 independent proton environments, mostly in the aromatic region.[12] However, formation of the **Os•Zn** cage is supported by a diffusion-ordered spectroscopy (DOSY) experiment (Fig. 2.2.4) which shows that all protons have a single diffusion rate of log D = -9.8 m^2s^{-1}; with an extra peak for the residual D_2O solvent peak at δ 4.79 ppm. This single diffusion rate is characteristic of an assembled cage and is quite different to the much less negative values of log D = -9.1 m^2s^{-1} for mononuclear $[Os(L^{nap})_3](PF_6)_2$ shown in previous work.[11] For comparison the **Os•Cd** cage diffuses at log D = -9.6 m^2s^{-1}.[11] Electrospray (ES) mass spectrometry was also used to characterise the cage and a characteristic sequence of signals for $\{Os_4Zn_4(L^{nap})_{12}(ClO_4)_{16-n}\}^{n+}$ appeared for n = 4, 5, 6 due to sequential loss of anions from the intact complex cage cation.

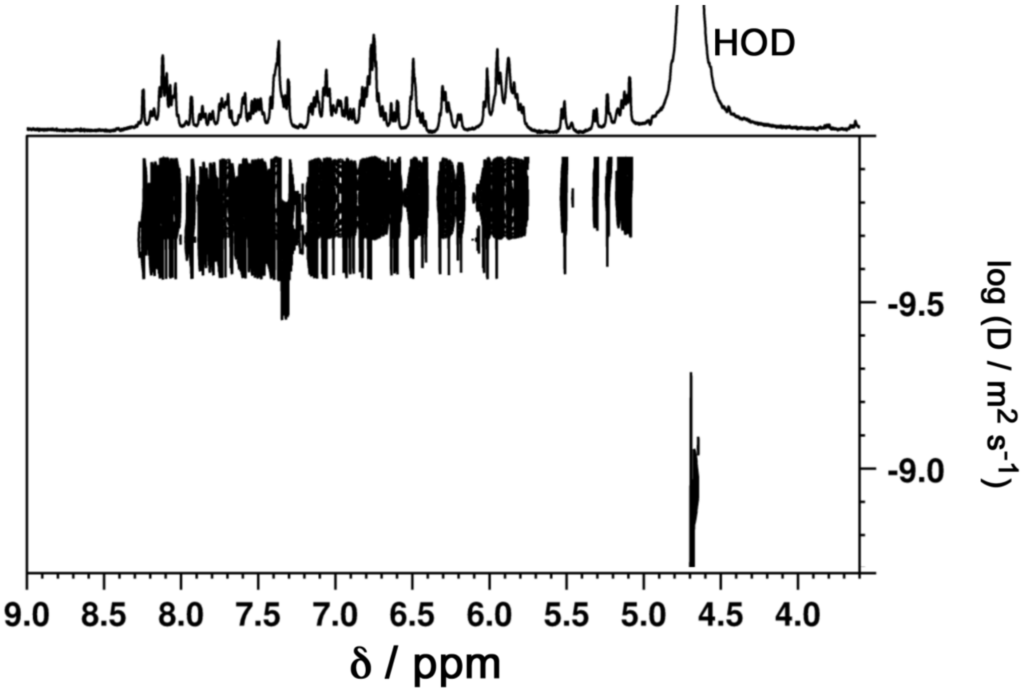

Figure 2.2.4: 400 MHz ^{1}H NMR and DOSY spectra of **Os•Zn** (chloride salt) in D_2O at 298 K.

In addition to the synthesis of $[Os(L^{nap})_3](PF_6)_2$ and $[Os_4Zn_4(L^{nap})_{12}]Cl_{16}$, a third Os(II) complex ($[Os(L^{Me})_3]^{2+}$ [L^{Me} = 1-Methyl-3-(2-pyridyl)pyrazole]) was synthesised, to be used for comparison with the two previous molecules, in terms of its spectral properties. $[Os(L^{Me})_3]^{2+}$ was produced to eliminate any substituent effects arising from the napthyl units, on the redox and photophysical properties of Os(II) complex units in the cage. The initial attempt to prepare $[Os(L^{Me})_3]^{2+}$ (figure 2.1.5), required methylation of the free ligand 3-(2-pyridyl)pyrazole, on the pyrazole ring. However, upon reaction, the doubly methylated ligand was actually the major product (figure 2.2.5), as characterized by ^{1}H NMR and mass spectrometry. Synthesis of $[Os(L^{Me})_3]^{2+}$ was then attempted by producing $[Os(pypzH)_3](PF_6)_2$ first, which effectively protects the nitrogen atom on the pyridyl ring by coordination to Os(II). Once this complex was obtained, the coordinated 3-(2-pyridyl)pyrazole ligand could then be subsequently methylated on the pyrazolyl ring. Fortunately, this route was successful. Initial preparation of $[Os(pypzH)_3][PF_6]_2$ through a microwave reaction at 200 ºC for 3 hours followed by purification through silica column chromatography gave a yield of 67%. The second step, methylation with MeI in MeCN to give $[Os(L^{Me})_3]^{2+}$, proceeded with a 96 % yield. The ^{1}H NMR spectrum showed the presence of four distinct ligand environments (figure 2.2.6), consistent with the expected 3:1 mer:fac ratio; the formulation was also confirmed by GC-MS.

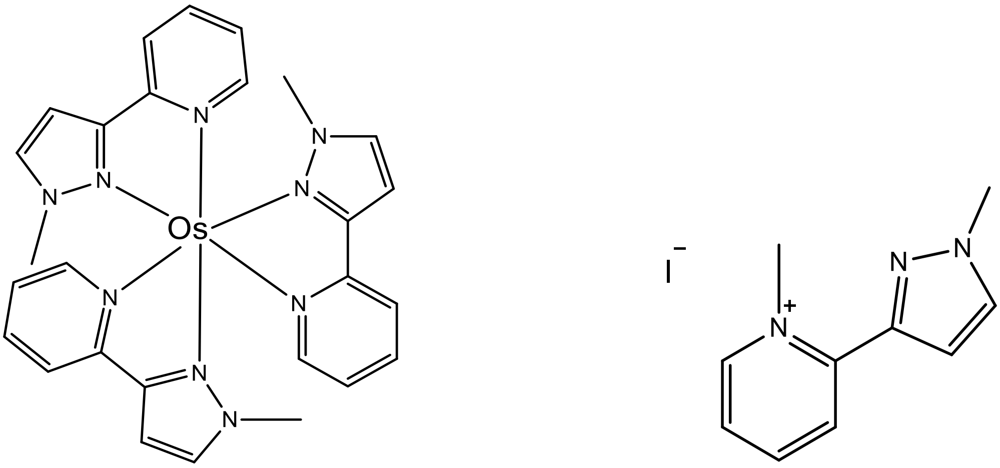

Figure 2.2.5: $[Os(L^{Me})_3]^{2+}$ and 1-Methyl-3-(2-pyridyl(1-methyl))pyrazole iodide.

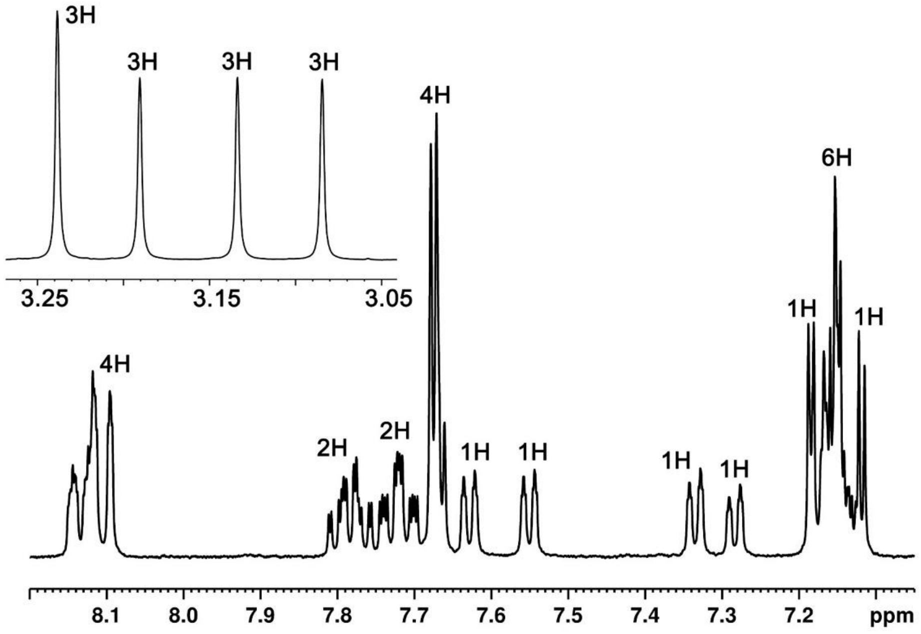

Figure 2.2.6: ^{1}H NMR (400 MHz, CD_3CN) of $[Os(L^{Me})_3](PF_6)_2$ showing the four environments for each type of proton arising from the mixture of *fac* and *mer* isomers.

2.2.1.1 Redox and photophysical properties

To enable the use of **Os•Zn** or the two mononuclear Os(II) complexes in different photochemical applications, it was first needed to determine their redox and photophysical properties. Figure 2.2.7 shows the UV/vis spectra of the three Os(II) complexes. The three molecules show similar absorption between 340 – 640 nm, with a high intensity spin-allowed ^{1}MLCT absorption between 380 - 450 nm and lower intensity spin-forbidden ^{3}MLCT absorptions between 490 – 600 nm. The spectra are similar in each case, as it is reflective of the Os(II)–tris(pyridyl-pyrazole) core unit, which all 3 complexes contain. However, the extinction coefficients of the MLCT absorptions are vastly different, with $[Os(L^{nap})_3]Cl_2$ and $[Os(L^{Me})_3]Cl_2$ having coefficients of $\varepsilon = 9300$ M^{-1} cm^{-1} and $\varepsilon = 5800$ M^{-1} cm^{-1} at 428 nm, but the **Os•Zn** cage giving an $\varepsilon = 24000$ M^{-1} cm^{-1}, reflecting the presence of four Os(II) chromophores in the cage.

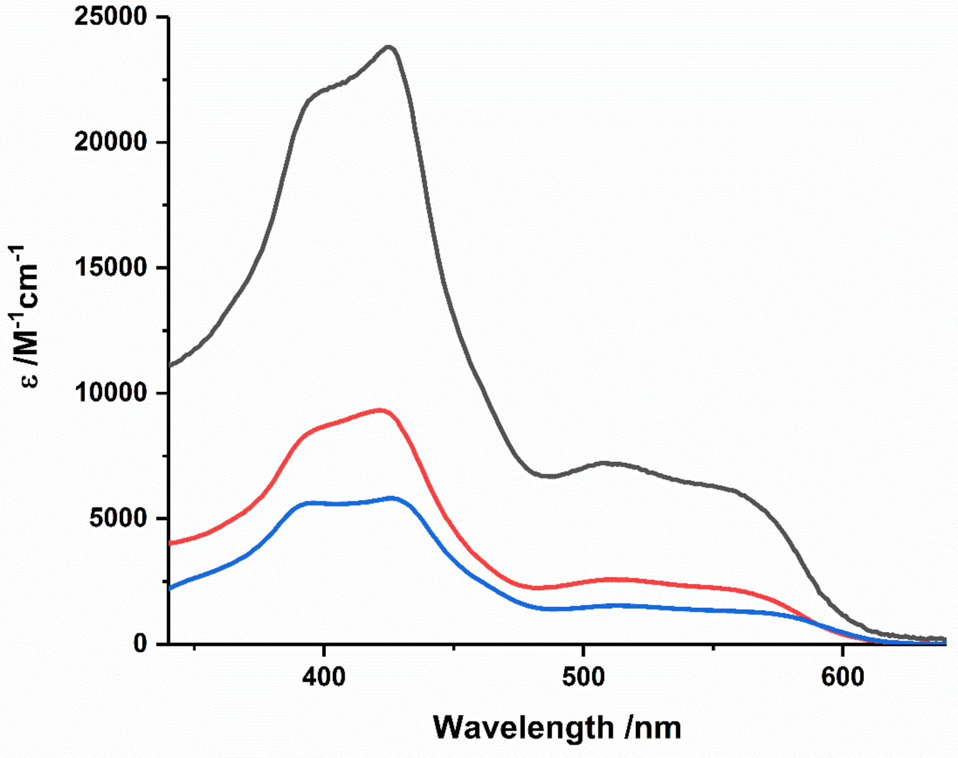

Figure 2.2.7: UV/vis spectra of $[Os_4Zn_4(L^{nap})_{12}]Cl_{16}$ (black), $[Os(L^{nap})_3]Cl_2$ (red) and $[Os(L^{Me})_3]Cl_2$ (blue).

Cyclic voltammetry of $[Os_4Zn_4(L^{nap})_{12}]Cl_{16}$ shows a chemically reversible Os(II)/Os(III) couple at 0.71 V (vs. SCE) in water (figure 2.2.8). This is less positive than a similar ruthenium based cage ($[Ru_4Cd_4(L^{nap})_{12}](ClO_4)_{16}$) where the corresponding Ru(II)/Ru(III) couple has a potential of 1.12 V (vs. SCE).[12] Differences like this are common for isostructural Ru(II) and Os(II) structures, as Os(II) has lower ionisation energy indicating its ability to be a better electron donor and is hence more easily oxidised. Also from previous work by the group, it has been shown that all four Os(II) units in the cage oxidise and reduce simultaneously, otherwise the redox wave would be broader or even split into multiple one electron components.[11] $[Os(L^{nap})_3]Cl_2$ behaves very similarly to **Os•Zn**, with only a small shift (10 mV) of the Os(II)/Os(III) couple to more positive potential compared to the cage. The reversibility of this process and the stability of Os(III) are essential prerequisites for use of **Os•Zn** as a photoredox catalyst for bound guests. The oxidation potential of $[Os(L^{Me})_3]Cl_2$ is shifted more and is roughly 100 mV less positive than that of the cage and of $[Os(L^{nap})_3]Cl_2$.

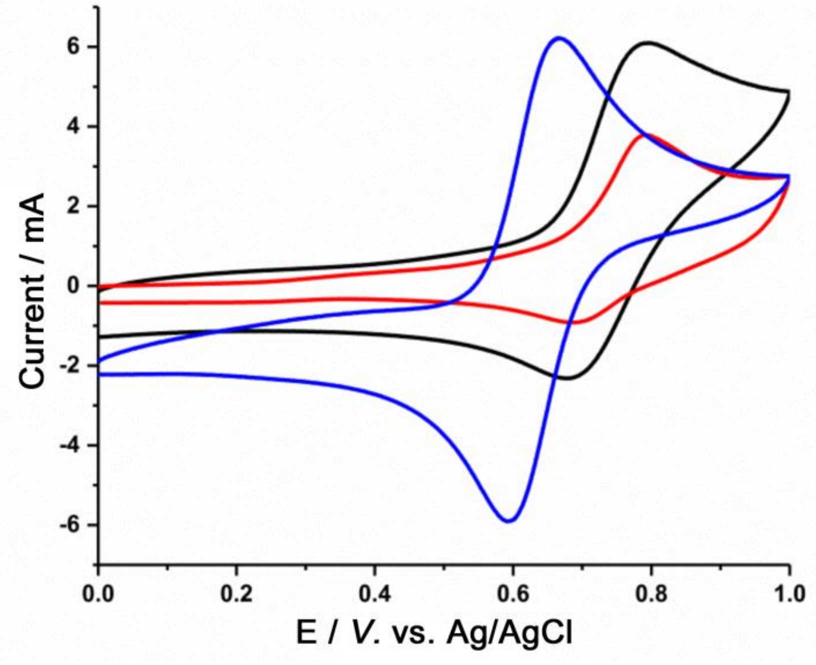

Figure 2.2.8: Cyclic voltammograms of **Os•Zn** (black), $[Os(L^{nap})_3]Cl_2$ (red) and $[Os(L^{Me})_3]Cl_2$ (blue), in H_2O, *vs.* an Ag/AgCl reference electrode.

The luminescence spectra (figure 2.2.9) of the complexes show similar emission characteristics to one another. Emission maxima vary over the narrow range of 635 – 660 nm. The broad and unstructured emission signal is typical of ^{3}MLCT-based emission, as are the long lifetimes that indicate spin-forbidden decay from the triplet state. In comparison, the standard $[Os(bipy)_3]^{2+}$ complex shows emission at 734 nm, which is lower in energy than that of these complexes. $[Os(L^{Me})_3]Cl_2$ has the lowest energy emission of the three complexes at 655 nm; it should therefore be the least good electron donor, as its excited state has the lowest energy content; however, this ability also depends on the redox potential. Luminescence spectra at 77K showed that the excited state energy of the ^{3}MLCT state of the $Os(pypz)_3$ unit is around 16000 cm^{-1} (2 eV). Therefore, according to Rehm and Weller, if the Os(II)/Os(III) couple is at +0.71 V (vs. SCE) (as shown above) then there is *ca.* 1.3 eV of energy available to reduce a guest.[11,13] No naphthalene based emission was observed when exciting the cage at 290 nm – the naphthalene based absorption maximum – only Os-based ^{3}MLCT emission was detected. This confirms that any higher-energy ligand-based excited states that may initially form, undergo fast intramolecular energy transfer to the Os(II)-diimine units at the cage vertices from which the characteristic ^{3}MLCT phosphorescence occurs.

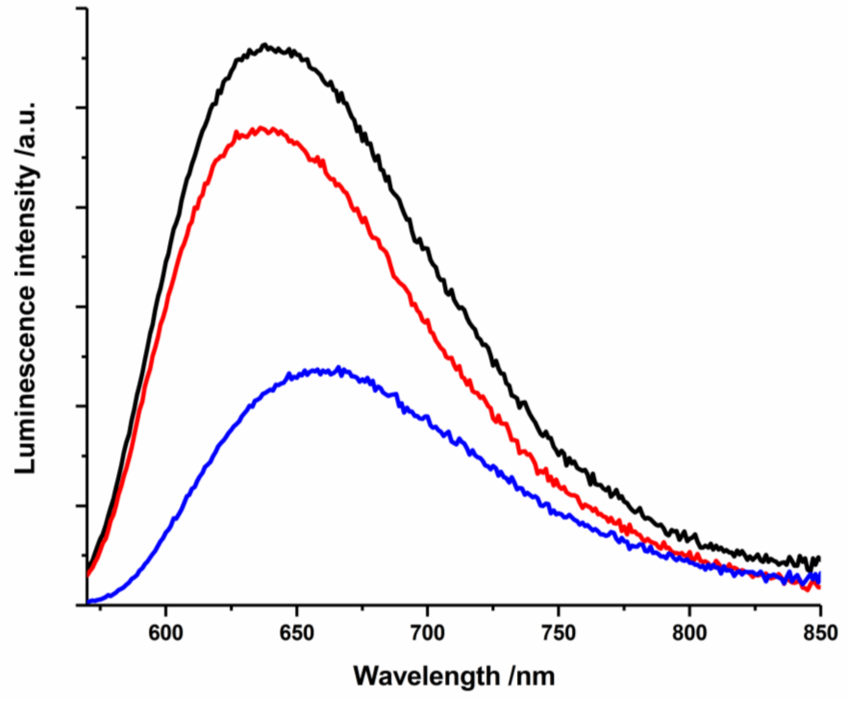

Figure 2.2.9: Luminescence spectrum of $[Os_4Zn_4(L^{nap})_{12}]Cl_{16}$ (black), $[Os(L^{nap})_3]Cl_2$ (red) and $[Os(L^{Me})_3]Cl_2$ (blue) in D_2O, excited at 550 nm (where the absorbance equalled 0.2 for all three complexes).

In addition, this luminescence in water has a monoexponential decay, with a lifetime of 337 ns: using a second lifetime component does not enhance the quality of the fit. On the other hand, the luminescence from both $[Os(L^{nap})_3]Cl_2$ and $[Os(L^{Me})_3]Cl_2$ show biexponential decay, with the ratio of the amplitudes of the components corresponding approximately to the 3:1 mixture of *fac* and *mer* isomers (as shown in figure 2.2.10). $[Os(L^{nap})_3]Cl_2$ having a lifetime of 354 ns and 183 ns and $[Os(L^{Me})_3]Cl_2$ having even shorter lifetimes of 206 ns and 97 ns.

Table 2.2.1 shows a summary of the redox and photophysical properties for the three complexes, with the three complexes having similar absorption, emission and oxidation values. However, there are distinct differences in the amplitudes of the absorption and emission of the cage compared to the mononuclear complexes.

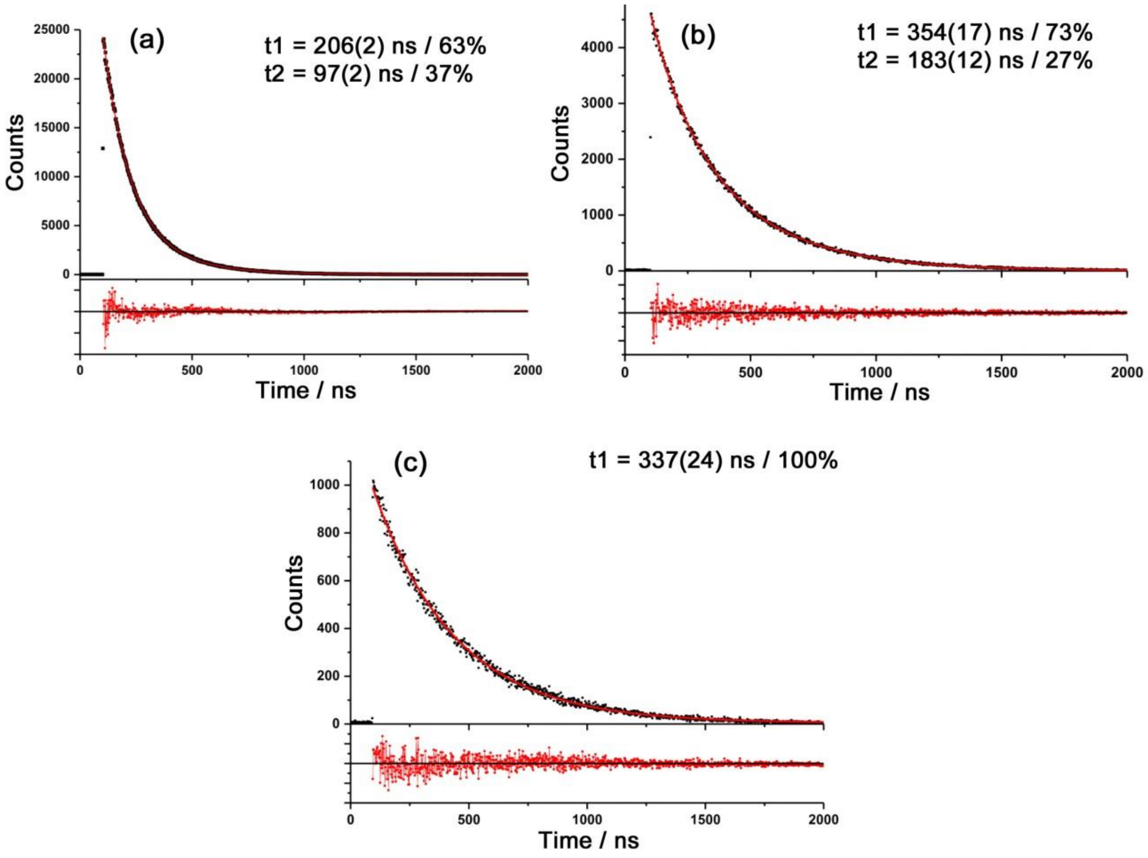

Figure 2.2.10: Time-resolved luminescence decay traces from aqueous solutions of (a) $[Os(L^{Me})_3]Cl_2$, (b) $[Os(L^{nap})_3]Cl_2$ and (c) **Os•Zn**. Measured data are black dots; best fit curves are shown by red lines; residuals from the fits are shown in red at the bottom.

Table 2.2.1: *Summary of redox and photophysical properties of* $[Os_4Zn_4(L^{nap})_{12}]Cl_{16}$, $[Os(L^{nap})_3]Cl_2$ *and* $[Os(L^{me})_3]Cl_2$*; obtained in an aerated aqueous solution at RT.*

	Absorption λ_{max} /nm ($10^{-3}\varepsilon$, L mol^{-1} cm^{-1})	Emission λ_{max} /nm^a	Emission τ /ns (esd)^b	$E_{1/2}$ (Os^{2+}/Os^{3+}) /V *vs.* SCE^c
$[Os_4Zn_4(L^{nap})_{12}]Cl_{16}$	400 (sh), 428 (23.5), 512 (7.2), 559 (sh)	638	337 (24)	0.75 (60 mV)^d
$[Os(L^{nap})_3]Cl_2$	398 (sh), 424 (9.3), 513 (2.6), 561 (sh)	636	183 (12), 354 (17)	0.74 (80 mV)
$[Os(L^{me})_3]Cl_2$	395 (sh), 430 (5.7), 515 (1.5), 565 (sh)	655	97 (2), 206 (2)	0.63 (60 mV)

[a] Excitation at 550 nm

[b] Obtained using 410 nm, *ca.* 100 ps pulsed excitation

[c] Measured *vs.* Ag/AgCl reference electrode, calculated using $E_{1/2}$(Ag/AgCl) = +0.045 V *vs.* SCE.

[d] Anodic/cathodic peak separation.

2.2.2 Guest binding

Guest binding in the central cavity is an imperative requirement for applications of cage structures. The guest binding in the Co(II)-based cubic cage $[Co_8(L^{nap})_{12}]^{16+}$, synthesised previously by the Ward group, has been well studied, so the shape and size limitations of guest binding in this cavity are well known.[4,7] This Co(II) cage is structurally analogous to the Os_4Zn_4 used for this work, only differing in the nature of metal corner atoms, [8 x Co(II) rather than four Os(II) and four Zn(II) ions]. From comparing the two crystal structures, the cages have very similar cubic structures and cavity size (volume: ~407 Å), with each face having a circular window of diameter *ca.* 4 Å to allow guest entry and exit.[5] For guest binding to occur, Rebek demonstrated that host-guest interactions are maximised when the guest fills approximately 55 % of the total volume of the cavity: therefore for this cubic cage, the ideal guest volume is around 224 Å.[14] There are a number of ways to measure guest binding and here we use both NMR and luminescence titrations.[15]

The guest molecules used for this work are in figure 2.2.11 and are all electron-accepting cyclic organic species. These guests were chosen so that future work of photophysical/photochemical applications could be exploited *via* photoinduced electron transfer between the excited state of the Os(II) units in the cage (electron donors) and bound guests (electron acceptors). To determine whether these guests are of suitable size and hydrophobicity to bind in the cage, they were screened through a modelling/calculation process using the docking programme GOLD, to estimate the binding constants of different guest molecules.[16] The guests below were all predicted to bind, with a range of binding constants from 10^2 – 10^4 M^{-1}, with the two benzyl alcohols portraying the weakest binding due to the hydrophilic hydroxy groups and with nitronaphthalene showing the strongest binding due to the delocalising nitro group allowing for high hydrophobicity.

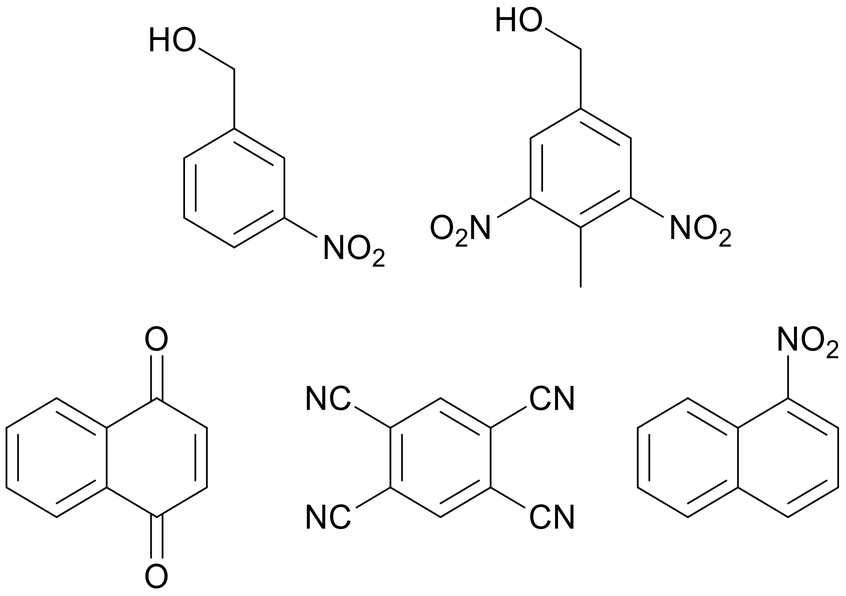

Figure 2.2.11: Chemical structures of 3-nitrobenzyl alcohol, 4-methyl -2,5-dinitrobenzyl alcohol, 1,4-naphthoquinone, 3,4,5,6-tetrachlorobenzoquinone and 1,2,4,5-tetracyanobenzene.

2.2.2.1 Luminescence quenching

From observation of the cage's photophysical properties and its ability to be a good excited-state electron donor, experiments were undertaken to look at the quenching of the luminescence of the cage, which should occur as a result of the electron-accepting guests binding in the cage cavity. We would expect quenching to occur as a consequence of photoinduced electron transfer between the cage excited state and the guest. The simplified Jablonski diagram (figure 2.2.12) shows the two routes of deactivation for the cage structure. When the guest is not present (1), the excited state decays via a radiative pathway from the ^{3}MLCT state (the normal phosphorescent emission). However, in the presence of the guest (2), electron transfer should occur to the guest to form a short-lived charge-separated cage$^{\bullet+}$/guest$^{\bullet-}$ excited state whose resultant decay is non-radiative, thereby quenching the emission. As discussed briefly in section 2.2.1, the ^{3}MLCT excited state of **Os•Zn** has an excited state energy of *ca.* 2 eV and given the ease of oxidation of Os(II) to Os(III) (0.7 V); we would expect **Os•Zn** to effect PET to any guest that has a reduction potential less negative than *ca.* -1.3 V vs SCE. All five of these guests (G) are sufficiently good electron acceptors to quench the Os-based MLCT excited state to give short-lived Os(III)/G$^{\bullet-}$ charge-separated states (table 2.2.2).

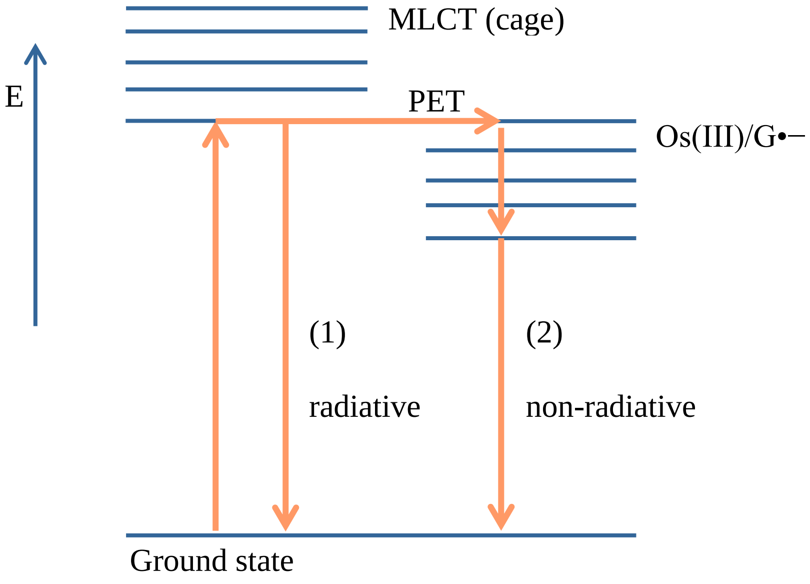

Figure 2.2.12: Illustrative Jablonski diagram to demonstrate the deactivation of the excited state of $[Os_4Zn_4(L^{nap})_{12}]Cl_{16}$ by a bound guest G.

Luminescence titrations using the **Os•Zn** cage, involving addition and binding of guests, were performed in water: increasing amounts of each guest were added to a stock concentration of the cage and through the progressive quenching of the cage luminescence as the guests bind a binding constant could be determined. Figure 2.2.13 shows an example of the quenching of the $[Os_4Zn_4(L^{nap})_{12}]Cl_{16}$ cage, with 1,4-naphthoquinone as a guest, with a steady decrease in the luminescence of the cage as more guest was added. The inset shows the 1:1 binding curve that has been fit to the data, with decrease in luminescence intensity versus the increase in guest concentration. Each guest showed similar quenching (figures included in appendices) and all of the data was fit to a 1:1 binding model, with the binding constants obtained shown in table 2.2.2.

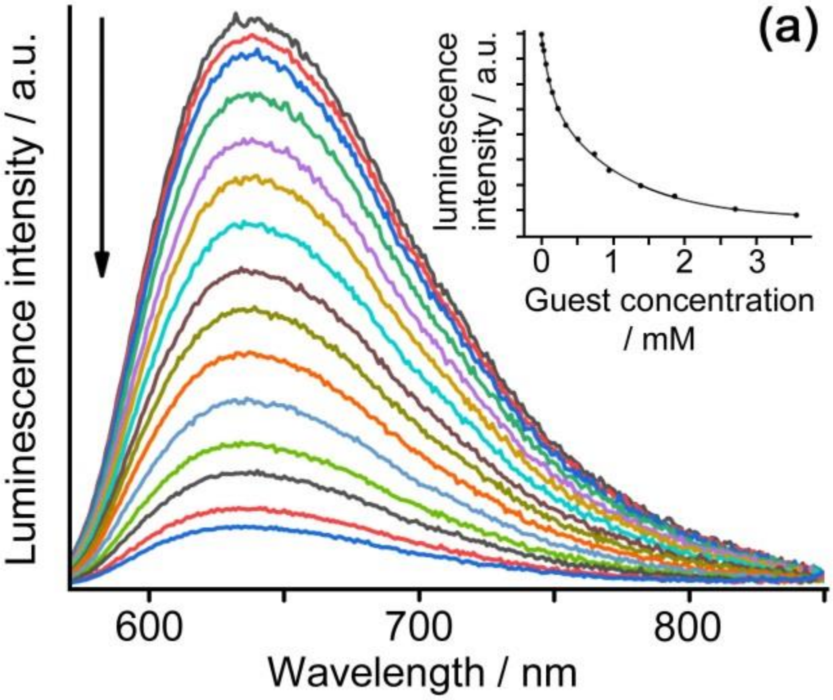

Figure 2.2.13: (a) Luminescence titration of [$Os_4Zn_4(L^{nap})_{12}$]Cl_{16} (0.025 mM) with 1,4-naphthoquinone as guest in H_2O, excitation at 550 nm, up to the point at which cage is ca. 90% occupied by guest.

Time-resolved measurements were taken during the titrations of the guests, 1,4-naphthoquinone and 1,2,4,5-tetracyanobenzene. In this system, when the encapsulated guest is an electron acceptor we would expect static quenching to occur as a complex is formed between the cage and the guest. However, there is the potential for dynamic quenching due to collision of cage with quencher in the solution. Note that these two cage/guest systems do not ever reach 100% guest occupancy, due to the limitations arising from the water solubility of the guests used. The Stern-Volmer plot, depicted in figure 2.2.14, shows that there is a mixture of static and dynamic quenching happening in both cage/guest systems, due to the curvature of the I_0/I component. In addition to this, there is also no indication of any short-lived emission components appearing associated with guest binding, which indicates that guest binding results in complete quenching of the Os-based emission from each cage.

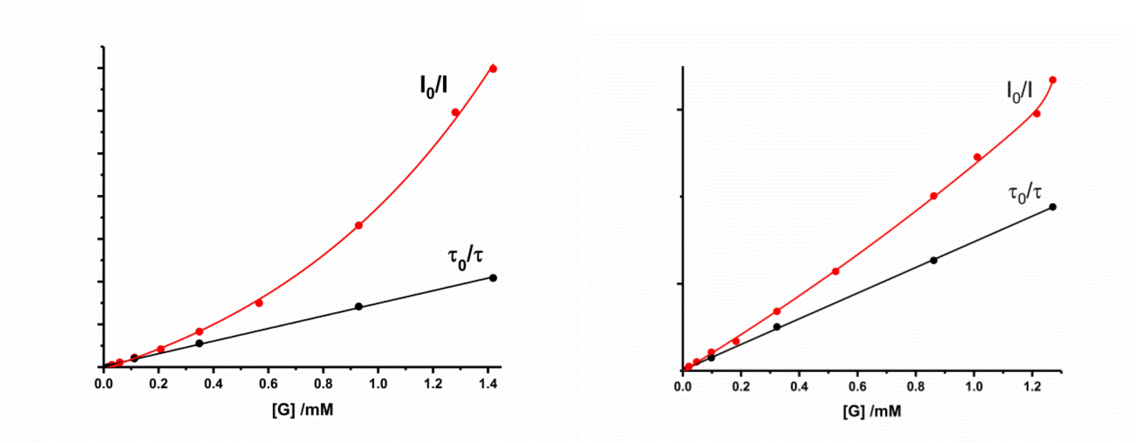

Figure 2.2.14: Stern-Volmer plots associated with quenching of **Os•Zn** by 1,4-naphthoquinone (left) and 1,2,4,5-tetracyanobenzene (right).

2.2.2.2 NMR binding studies

In addition to the luminescence quenching studies performed on the cage/guest systems, measurements of the binding of these guests was performed through NMR spectroscopy to confirm the results of the 1:1 binding constants obtained from luminescence titrations. Unfortunately, due to the substantial overlap of cage and guest peaks in the aromatic region of the NMR spectrum, and the large number of inequivalent proton environments in the Os_4Zn_4 cage, NMR titrations with this cage were not practicable. Therefore, titrations could be performed using the analogous Co(II) based cage $[Co_8 L^{nap})_{12}]Cl_{16}$ which is isostructural and paramagnetic, allowing the shift of host peaks on guest binding (fast exchange case) or the formation of new host/guest peaks on guest binding (slow exchange case) to be observed easily, enabling binding constants to be calculated (figure 2.2.15). In addition to this wide spread of ^{1}H signals; in the negative ppm region of the spectrum, -1 to -12 ppm, we can also observe new signals associated with bound guests when the host/guest complex forms. This is due to the guest now being surrounded by 8 paramagnetic Co(II) ions, which causes a substantial change in the guest protons chemical shift. Evidence for this is shown in previous work by the group where full characterisation of NMR spectra is performed to assign each peak in the spectrum of free host and host/guest complexes.[4]

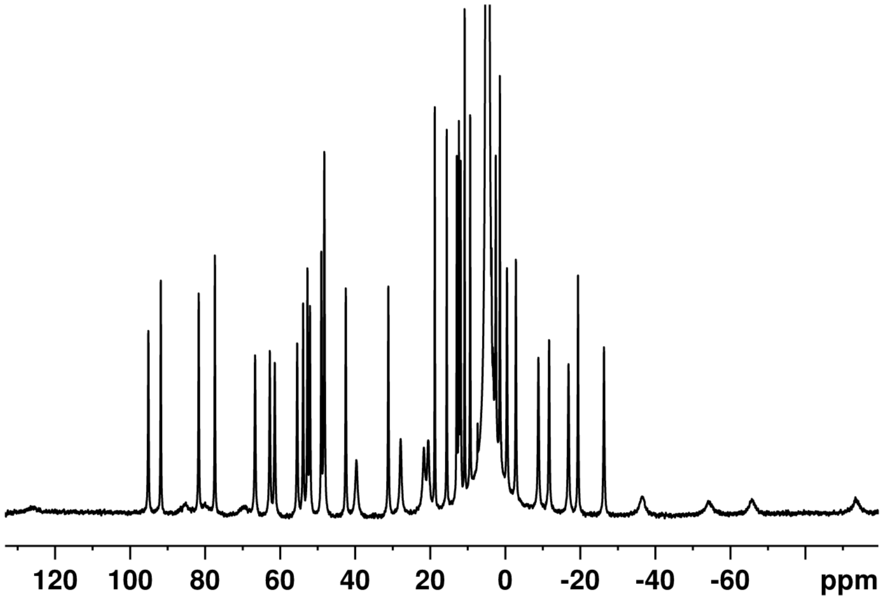

Figure 2.2.15: Paramagnetic ^{1}H NMR spectrum of ($[Co_8 L^{nap})_{12}]Cl_{16}$).

NMR titrations were performed in a similar way to the luminescence titrations: the guest was dissolved in a stock solution of cage and this is then titrated in increasing portions into a cage sample. The difference between the processing of the binding constants, associated with these experiments, is that the guest can be in either fast or slow exchange in the cage cavity on the NMR timescale. For fast exchange cases, the fitting of a 1:1 binding isotherm is the same as for the luminescence measurements, where the shift in host peaks is compared to the increase in [G]. On the other hand, for slow exchange, where separate sets of signals can be resolved of free cage and cage/guest complexes, binding constants can be determined by integration of the separate sets of signals.

For the guests in figure 2.2.11, addition of NQ, NN and TCNB to the Co_8 cage all resulted in the appearance of new peaks in the NMR spectrum relating to the host/guest complex rather than just the free host. This is shown in figure 2.2.16, where as the free host signal intensities diminish, new host.guest peaks appear for the host containing a bound guest. Deconvolution and integration of these peaks was attempted, however the results were unreliable with the binding constants for each addition varying over quite a large range, which is thought to potentially be due to the chloride counter-anion which can compete for guest binding in a way that is non-linear with concentration.[17]

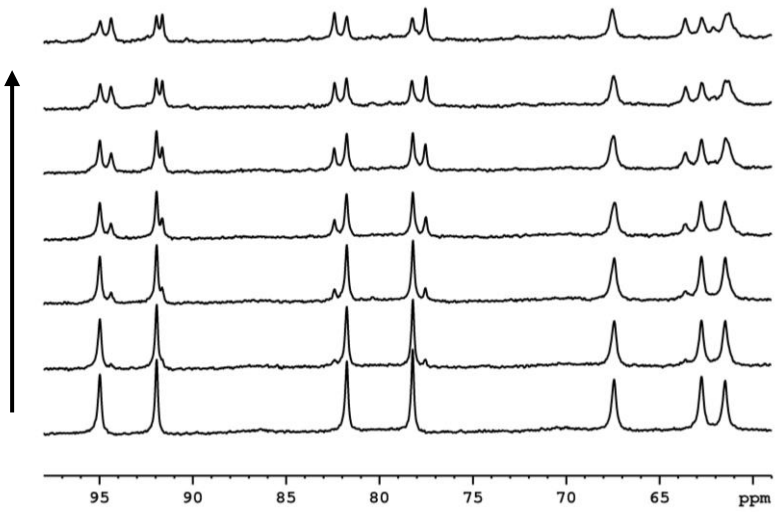

Figure 2.2.16: ^{1}H NMR spectra of titration of the addition of up to 16 equivalents of TCNB into $[Co_8(L^{nap})_{12}]Cl_{16}$ (0.15 mM in D_2O), showing the grow in of host.guest peaks.

As the binding constants could not be reliably determined through deconvolution of free/bound cage NMR signals, and as these guests actually appear to exchange in the cage in a time that borders that of the NMR timescale, there also appears to be a shift in the host peaks as more guest is added. Figure 2.2.17 shows an example of this, where the same regions of the NMR spectra, of NQ, NN and TCNB guest titrations are compared, with a clear increase in intensity of host.guest peaks as well as a change in chemical shift of the host peaks. This shift of host peaks was fit to a 1:1 binding isotherm, where comparable binding constants to that of the luminescence titration were obtained (table 2.2.2).

As described, in some cases we can also see evidence for the shifting of the bound guest signals from the aromatic region (6 - 9 ppm) to the negative chemical shift region, as the guest binds into the cage. With NQ, NN and TCNB there was evidence of these new peaks, seen in figure 2.2.17, confirming that guest binding is in slow exchange in these three cases. In contrast to these three guests, the two nitrobenzyl alcohol guest appeared to bind purely in fast exchange, with the binding constants being determined by the shift in ppm upon titration (table 2.2.2).

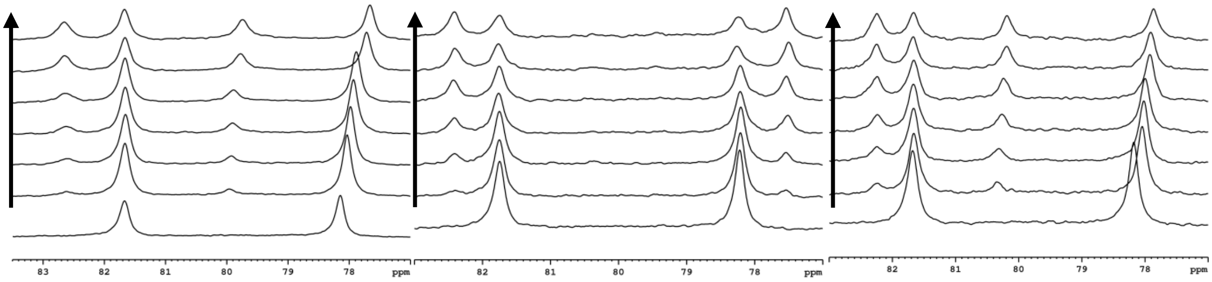

Figure 2.2.17: NMR titration of NN, TCNB and NQ into $[Co_8(L^{nap})_{12}]Cl_{16}$ (0.15 mM in D_2O) between 77-83 ppm, showing the shift of host peaks and the grow in of host.guest peaks

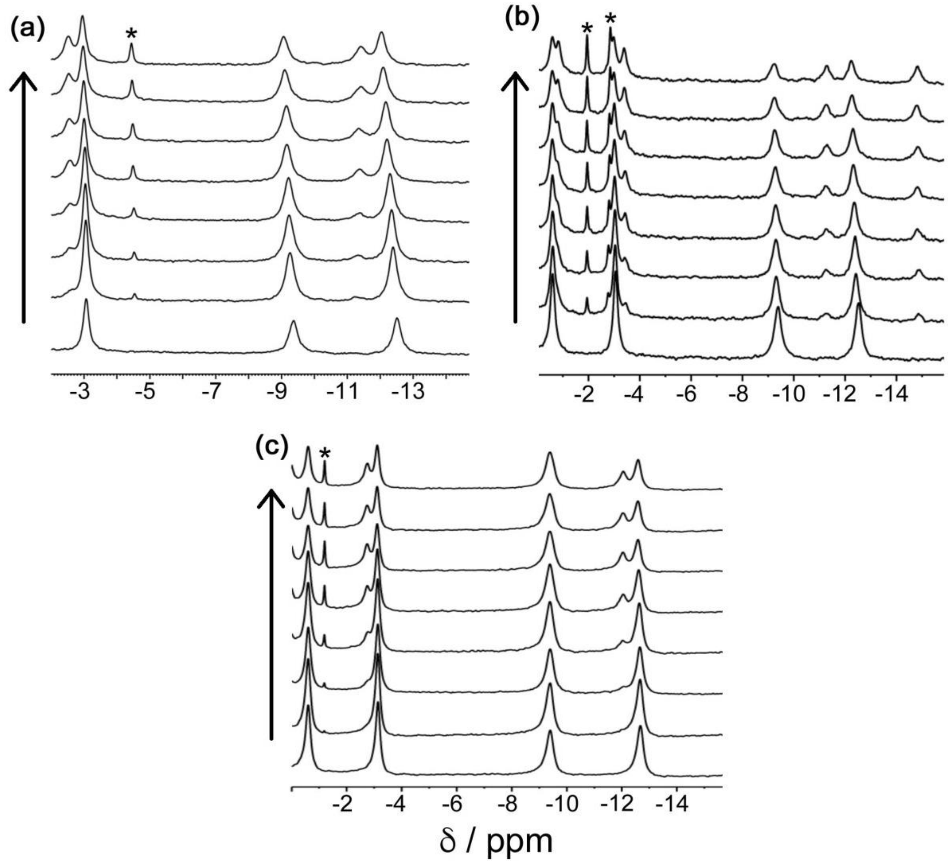

Figure 2.2.17: 400 MHz ^1H NMR spectra recorded during titration of (a) NN, (b) NQ and (c) TCNB (up to 16 equivalents of each) into $[Co_8(L^{nap})_{12}]Cl_{16}$ (0.15 mM in D_2O). Sharper new signals associated with bound guest (labelled *).

A summary of the binding constants is shown in table 2.2.2, with the binding constants determined from luminescence spectroscopy and NMR spectroscopy correlating well with each other and are of the same order of magnitude, indicating that the guests selected do bind with a 1:1 fit. The absolute values of the binding constants of *ca.* 10^3 M^{-1} are to be expected for these guests, which are of similar size to each other and have a similar hydrophobic surface area.

Table 2.2.2: *Summary of binding constants of five guests and reduction potentials.*

	K(lum) /M^{-1}	**K(NMR) /M^{-1}**	**$E_{A/A-}$ /V vs SCE**
1,4-naphthoquinone	2000	2000	-0.71[18]
1,2,4,5-tetracyanobenzene	4000	3000	-0.66[19]
1-nitronaphthalene	8000	3000	-0.99
3-nitrobenzyl alcohol	2000	2000	-0.46
4-methyl-3,5-dinitrobenzyl alcohol	2000	3000	-

2.2.2.3 X-ray crystallography

Lastly, to conclude the characterisation of the binding of these guests, X-ray crystallography techniques were employed to determine if solid state guest binding could be observed and if so, to determine how the guest might sit in the cavity. Again, for this, the Co(II) based $[Co_8(L^{nap})_{12}](BF_4)_{16}$ cage was used as an analogue for **Os•Zn**, as its use in crystal soaking methods have previously been developed by the group for X-ray studies. For this experiment, the host/guest complex of $[Co_8(L^{nap})_{12}](BF_4)_{16}$ and TCNB was prepared using a "crystalline sponge" method, where crystals of empty host are treated with a concentrated solution of guest in methanol, which are then mounted on the diffractometer.[20,7]

Figure 2.2.18 shows the crystal structure of H•TCNB, where H is the host ($[Co_8(L^{nap})_{12}](BF_4)_{16}$), with a TCNB guest positioned in the centre of the cavity, across the inversion centre. Two of the opposing cyano groups are directed into the two H-bond donor pockets of the *fac* metal vertices. This means that these two N atoms form weak CH···N interactions with the convergent set of CH protons, that lie close to the cationic metal centres and the guest is anchored by this at either end – the first time this has been seen in a cage/guest complex of this family. There are non-bonded C···N separations of 3.38-3.40 Å and CN···HC distances of the range 2.48−2.75 Å. The non-bonded N(15G)···Co(4) separation of 5.33 Å is comparable to other guests whose electron-rich regions lie in this hydrogen-bond donor pocket.

This type of H-bonding interaction occurs in all cage/guest complexes that we have structurally characterized and anchors the guests in place.[21,22]

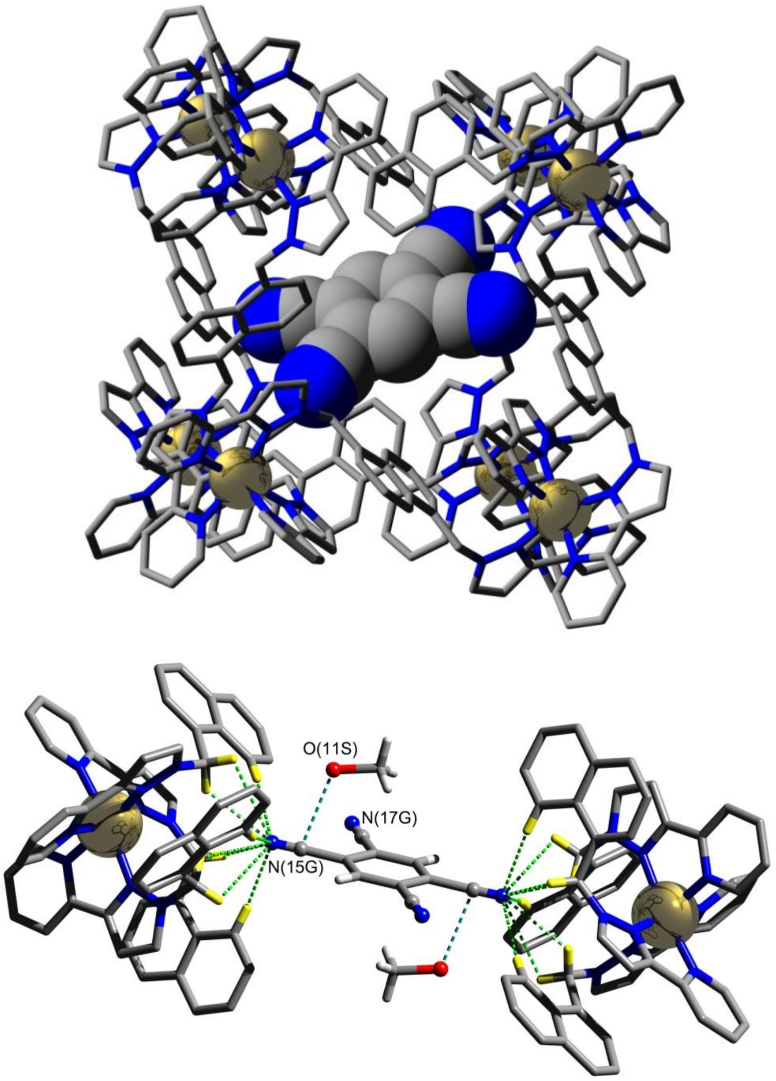

Figure 2.2.18: Crystal structure of the cage/guest adduct [$Co_8(L^{nap})_{12}](BF_4)_{16}$•0.66(TCNB)**.** Top: Complete cage. Bottom: The guest and the two opposed *fac*-tris(chelate) metal complex vertices that form the hydrogen bond donor pockets.

2.3 Conclusions

There are two main conclusions from this work. Firstly, a successful synthetic procedure has been developed to produce an Os_4Zn_4 cubic cage that contains both Os(II)-based photosensitisers and is water-soluble to facilitate guest binding. It has been characterised through DOSY NMR spectroscopy, mass spectrometry and X-ray crystallography. This cage has also been shown to have useful photophysical and redox properties, where it has the potential to be a good photo-electron donor to bound guests: it undergoes reversible Os(II)/Os(III) redox processes and shows long-lived ^{3}MLCT emission in the visible region.

The Os_4Zn_4 cage can successfully be converted to the chloride salt, which is thus soluble in water. This has allowed for studies on host-guest binding with various organic guest molecules. This has shown that the bound electron-accepting guests can quench the emission of the cage, which suggests that there is photo-induced electron transfer that can occur between the components of the cage/guest complexes. In addition to this, guest binding has also been proven through NMR titrations, where the shift of cage signals has been monitored and an X-ray crystal of Cage.TCNB confirms guest binding.

2.4 Experimental

2.4.1 Experimental Techniques

Nuclear Magnetic Resonance (NMR) Spectroscopy

One-dimensional ^{1}H NMR and two-dimensional DOSY spectra were recorded using a Bruker Avance III HD 400 spectrometer. Spectroscopic grade deuterated solvents were used and all spectra were calibrated using residual solvent peaks. All chemical shifts are quoted in ppm and the following abbreviations are used when reporting the spectra; br – broad, s – singlet, d – doublet, dd – doublet of doublets, ddd – doublet of double doublets, t – triplet, td – triplet of doublets, tt – triplet of triplets, m – multiplet.

Mass Spectrometry

Mass spectra were obtained from the University of Sheffield Mass Spectrometry Service. Electrospray ionisation (ES) spectra were recorded on an MicroMass LCT spectrometer and Electron ionisation (EI) spectra were recorded on a VG AutoSpec mass spectrometer. All measurements were taken at room temperature.

UV-visible Absorption Spectroscopy

UV/vis spectra were recorded on a Varian Cary 50 Bio UV-visible spectrophotometer and were baseline corrected, with the samples in solution in a quartz cuvette, with a 1 cm path length. Extinction coefficients (ε) were calculated from a linear plot of absorbance (at a particular wavelength) against concentration in accordance with the Beer Lambert law (equation 2.1).

$$A = \varepsilon c l$$

Equation 2.1: The Beer Lambert law. A = absorbance, ε = extinction coefficient (M^{-1} cm^{-1}), l = path length (cm), c = concentraion (M)

Emission Spectroscopy

Emission spectra were obtained from a Horiba John Yvon Fluoromax-4 spectrofluorometer and were corrected using correction files included within the FluorEssence^{TM} software. Analyte solutions were contained within quartz cuvettes of 1 cm pathlength and of sufficient dilution with an optical density of no more than 0.2 at the excitation wavelength.

Lifetime measurements

Luminescence lifetimes were measured in air-equilibrated H_2O solutions by the time-correlated single-photon counting method, using an Edinburgh Instruments 'Mini-τ' instrument using a 405 nm, ~70 ps pulsed diode laser excitation source, and with the decay data fitted using the supplied software.

Cyclic Voltammetry

Cyclic voltammetry was performed in an electrolyte solution of water and 0.1 M NaCl. The potential was controlled with an Emstat^{3+} Potentiostat using PSTrace software. A solvent saturated atmosphere of nitrogen was used to degas the sample and all samples were recorded under an inert atmosphere of nitrogen. The electrodes used were a glassy carbon working electrode, a platinum wire counter electrode and an Ag/AgCl reference electrode. All potentials are quoted versus SCE and scan rates of 10-100 mV s^{-1} were used.

NMR titrations

$[Co_8(L^{nap})_{12}](Cl)_{16}$ was prepared according to previously published methods.[23] For all host/guest binding experiments samples were prepared as follows. A stock host solution of $[Co_8L_{12}](Cl)_{16}$ (0.1 – 0.2 mM) in D_2O was used and each guest is individually dissolved in 2.5 ml of the host solution; the mass of guest used varied with the desired concentration and solubility of each guest. All binding experiments were performed three separate times; the values for binding constants quoted are the average of the three measurements rounded to 1 significant figure. For the fast exchange cases, the changes in chemical shift were plotted and fitted to a 1:1 host:guest binding model. For the slow exchange cases, where separate sets of signals for free cage and cage/guest peaks are observed, binding constants were determined by deconvolution and integration of the signals. The NMR data was processed using either Bruker Topspin 3.2 or 4.0.3 and was fitted to binding isotherms using 14allMaster.xls, which is a macro-based Excel fitting program written by Christopher A. Hunter (University of Cambridge).

Luminescence titrations

Luminescence titrations were performed by preparing a stock solution of $[Os_4Zn_4(L^{nap})_{12}](Cl)_{16}$ (0.025 mM) in deionised water. Guest solutions (0.3 - 3 mM) were made up using stock host solution (5 ml) and added in small portions to the quartz cuvette containing the host solution, with a luminescence spectrum measured after each addition. Luminescence spectra were recorded on a Horiba Jobin Yvon Fluoromax 4 spectrophotometer, with excitation at 550 nm and an emission window of 570 – 850 nm. Changes in luminescence intensity with added guest concentration were fitted to a 1:1 host:guest binding model.

X-ray crystallography

$[Os_4Zn_4(L^{nap})_{12}](ClO_4)_{16}$ diffraction data was collected by Alex Metherell (University of Sheffield) on a Bruker Apex-II diffractometer at the University of Sheffield. In each case a crystal was removed from the mother liquor, coated with oil, and transferred quickly into a stream of cold nitrogen, on the diffractometer to prevent any decomposition due to solvent loss. In all cases, after integration of the raw data, and before merging, an empirical absorption correction was applied (SADABS) based on comparison of multiple symmetry-equivalent measurements.[24] The structures were solved by direct methods and refined by full-matrix least squares on weighted F2 values for all reflections using the SHELX suite of programs.[25]

$[Co_8(L^{nap})_{12}](BF_4)_{16}$•0.66(TCNB) diffraction data was collected by Stephen Argent and Christopher Taylor (University of Warwick) on beamline i-19 at the Diamond Light Source. Single crystals of $[Co_8(L^{nap})_{12})](BF_4)_{16}$ used for determination of the structure of the $[Co_8(L^{nap})_{12})](BF_4)_{16}$•TCNB adduct were prepared as described previously.[7] The details of the refinement performed by Christopher Taylor are described in the published paper associated with this chapter.[26]

2.4.2 Synthetic procedures

Starting Materials

Metal salts, all organic reagents and guests were purchased from Alfa or Sigma-Aldrich and used as received. The ligand L and $[Co_8(L^{nap})_{12})]Cl_{16}$ were prepared according to the published methods.[3]

Synthesis of $[Os(L^{nap})_3](PF_6)_2$

L (0.68 g, 1.49 mmol) was dissolved in ethylene glycol (70 ml) by heating to reflux for 1 hour. Then $OsCl_3.6H_2O$ (0.05 g, 0.14 mmol), dissolved in additional ethylene glycol (70 ml) and water (2 ml) was slowly dropped into the solution of L for 6 hours and left to reflux for 24 hours. After cooling to room temperature a saturated aqueous solution of KPF_6 was added to precipitate the crude product, which was collected by filtration. The filtrate was washed with water and then was dissolved in acetonitrile and purified by column chromatography on silica by elution with acetonitrile (MeCN)/water/saturated aqueous KNO_3 (100 : 4 : 2, v/v/v). The main red band was collected and solvent was removed to give a dark red precipitate. The product was dissolved in water and aqueous KPF_6 was added and solvent extraction was performed using dichloromethane (DCM) to yield pure $[Os(L^{nap})_3](PF_6)_2$, from which the solvent was removed in vacuo. Yield: 0.06 g, 0.03 mmol, 24%. ESMS: m/z 1664 $(M - PF_6)^+$, 760 $(M - 2PF_6)^{2+}$. UV/Vis in MeCN [λ_{max}/nm (10^{-3} ε/M^{-1} cm^{-1})]: 555 (sh), 510 (sh), 425 (12.5), 400 (sh), 283 (80.4), 226 (149). For conversion to the water-soluble chloride salt, $[Os(L^{nap})_3](PF_6)_2$ (30 mg, 0.015 mmol) was mixed with 1x2 Dowex, in distilled water (15 ml) and left to stir at room temperature for 4 hours, until the complex had completely dissolved. The sample was filtered through a microporous filter before use.

Synthesis of $[Os_4Zn_4(L^{nap})_{12}](ClO_4)_{16}$

$[Os(L^{nap})_3](PF_6)_2$ (0.032 g, 0.018 mmol) and $Zn(ClO_4)_2{\cdot}6H_2O$ (0.067 g, 0.18 mmol) were stirred in nitromethane (15 ml) overnight. The mixture was filtered and then crystallised by slow diffusion of di-isopropyl ether into the $MeNO_2$ solution. The pure crystalline product was collected by filtration and washed with di-isopropyl ether, methanol, and diethyl ether. Yield: 0.050 g, 0.005 mmol, 21%. ESMS: *m/z* 1220.4 $(M - 6ClO_4)^{6+}$; 1482.2 $(M - 5ClO_4)^{5+}$; 1881.3 $(M - 4ClO_4)^{4+}$ (most intense component of isotope cluster given in each case). For conversion to the water-soluble chloride salt **Os•Zn**, $[Os_4Zn_4(L^{nap})_{12}](ClO_4)_{16}$ (26 mg, 0.004 mmol) was mixed with 1x2 Dowex, in distilled water (15 ml) and left to stir at room temperature for 4 hours, until the complex had completely dissolved. The sample was filtered through a microporous filter before use. UV/Vis in H_2O [λ_{max}/nm (10^{-3} ε/M^{-1} cm^{-1})]: 555 (sh), 510 (sh), 426 (48), 400 (sh), 287 (310), 227 (560).

Synthesis of $[Os(L^H)_3](PF_6)_2$ (mixture of fac and mer isomers).

3-(2-Pyridyl)pyrazole (0.166 g, 1.14 mmol), $OsCl_3.6H_2O$ (0.106 g, 0.30 mmol) and ethylene glycol (7 ml) were combined in a 10 ml microwave tube, which was then heated in a microwave synthesiser (Discovery S, CEM Microwave Technology) to 200 °C for 3h. The solution was allowed to cool and an aqueous solution of KPF_6 (30 ml) was added. The resulting suspension was then filtered over celite to yield a brown precipitate and a red solution. The solution was then extracted with several portions of DCM and the solvent was removed *in vacuo*. The resultant precipitate was next purified using column chromatography on silica by elution with MeCN/water/saturated aqueous KNO_3 (100:5:1, *v/v/v*) and the first red band was collected and the solvent removed *in vacuo*. The product was dissolved in water, and aqueous KPF_6 and DCM were added to perform a solvent extraction of the hexafluorophosphate salt of the complex into DCM. The solvent was removed by evaporation and the pure product was then dried *in vacuo*. Yield: 0.185 g, 0.20 mmol, 67 %. The ^1H NMR spectrum is broadened by hydrogen-bonding aggregation in solution, but the number of signals is consistent with the 1:3 ratio of *fac:mer* isomers which results in four distinct ligand environments with equal likelihood.[15] ^1H NMR (400 MHz, CD_3CN): δ 8.12 (m, 4H), 7.75 (m, 4H), 7.72 (m, 4H), 7.59 – 7.50 (m, 2H), 7.42 (m, 2H), 7.21 – 7.04 (m, 8H). ESMS: *m/z* 626.1 $(M - 2PF_6 - H^+)^{1+}$, 313.6 $(M - 2PF_6)^{2+}$.

Synthesis of $[Os(L^{me})_3](PF_6)_2$.

$[Os(L^H)_3](PF_6)_2$ (0.185 g, 0.2 mmol) was dissolved in MeCN (50 ml), to which Cs_2CO_3 (0.470 g, 1.4 mmol) and methyl iodide (0.67 ml, 10.8 mmol) were added and the solution was left to reflux for 18 hours. The mixture was left to cool, excess Cs_2CO_3 was filtered off, and then the solvent was removed *in vacuo*. The resultant precipitate was then purified using column chromatography on silica by elution with MeCN/water/saturated aqueous KNO_3 (100:10:2, *v/v/v*). The main red band was collected and dissolved in water; addition of aqueous KPF_6 and

DCM allowed solvent extraction of the hexafluorophosphate salt into DCM to be performed. Evaporation of the solvent afforded a pure red precipitate. Yield: 0.184 g, 0.19 mmol, 96 %. ^{1}H NMR (400 MHz, CD_3CN): δ 8.14 (m, 4H), 7.86 – 7.70 (m, 4H), 7.68 (m, 4H), 7.66 (d, 1H), 7.57 (d, 1H), 7.36 (d, 1H), 7.31 (d, 1H), 7.24 – 7.10 (m, 8H), 3.21 (s, 3H), 3.16 (s, 3H), 3.11 (s, 3H), 3.06 (s, 3H). ESMS: *m/z* 334.6 (M – $2PF_6)^{2+}$. $[Os(L^{me})_3](PF_6)_2$ could be converted to its water-soluble chloride salt by ion-exchange with Dowex 1x2 resin, as described above for the **Os•Zn** cage.”

2.5 References

1 S. Turega, M. Whitehead, B. R. Hall, M. F. Haddow, C. A. Hunter and M. D. Ward, *Chem. Commun.*, 2012, **48**, 2752–2754.

2 W. Cullen, C. A. Hunter and M. D. Ward, *Inorg. Chem.*, 2015, **54**, 2626–2637.

3 I. S. Tidmarsh, T. B. Faust, H. Adams, L. P. Harding, L. Russo, W. Clegg and M. D. Ward, *J. Am. Chem. Soc.*, 2008, **130**, 15167–15175.

4 S. Turega, M. Whitehead, B. R. Hall, A. J. H. M. Meijer, C. A. Hunter and M. D. Ward, *Inorg. Chem.*, 2013, **52**, 1122–1132.

5 S. Turega, M. Whitehead, B. R. Hall, M. F. Haddow, C. A. Hunter and M. D. Ward, *Chem. Commun.*, 2012, **48**, 2752–2754.

6 M. Whitehead, S. Turega, A. Stephenson, C. A. Hunter and M. D. Ward, *Chem. Sci.*, 2013, **4**, 2744–2751.

7 S. Turega, W. Cullen, M. Whitehead, C. A. Hunter and M. D. Ward, *J. Am. Chem. Soc.*, 2014, **136**, 8475–8483.

8 W. Cullen, A. J. Metherell, A. B. Wragg, N. H. Williams and M. D. Ward, *J. Am. Chem. Soc.*, 2018, **140**, 2821–2828.

9 J. R. Piper, L. Cletheroe, C. G. P. Taylor, A. J. Metherell, J. A. Weinstein, I. V. Sazanovich and M. D. Ward, *Chem. Commun.*, 2017, **53**, 408–411.

10 A. J. Metherell and M. D. Ward, *Chem. Commun.*, 2014, **50**, 10979–82.

11 A. B. Wragg, A. J. Metherell, W. Cullen and M. D. Ward, *Dalt. Trans.*, 2015, **44**, 17939–17949.

12 A. J. Metherell and M. D. Ward, *Chem. Commun.*, 2014, **50**, 6330–2.

13 D. Rehm and A. Weller, *Isr. J. Chem.*, 1970, **8**, 259–271.

14 J. Rebek, *Acc. Chem. Res.*, 2009, **42**, 1660–8.

15 P. Thordarson, *Chem. Soc. Rev.*, 2011, **40**, 1305–1323.

16 W. Cullen, S. Turega, C. A. Hunter and M. D. Ward, *Chem. Sci.*, 2015, **6**, 2790–2794.

17 W. Cullen, A. J. Metherell, A. B. Wragg, C. G. P. Taylor, N. H. Williams and M. D. Ward, *J. Am. Chem. Soc.*, 2018, jacs.7b11334.

18 I. Amada, M. Yamaji, S. Tsunoda and H. Shizuka, *J. Photochem. Photobiol. A Chem.*, 1996, **95**, 27–32.

19 M. Fagnoni, S. Protti, D. Ravelli and A. Albini, *Beilstein J. Org. Chem.*, 2013, 800–808.

20 C. G. P. Taylor, J. R. Piper and M. D. Ward, *Chem. Commun.*, 2016, **52**, 6225–6228.

21 M. D. Ward, C. A. Hunter and N. H. Williams, *Chem. Lett.*, 2016, 1–8.

22 A. J. Metherell and M. D. Ward, *Dalt. Trans.*, 2016, **45**, 16096–16111.

23 W. Cullen, S. Turega, C. A. Hunter and M. D. Ward, *Chem. Sci.*, 2015, **6**, 625–631.

24 G. M. Sheldrick, 2008.

25 Sheld, *Acta Crystallogr.*, 2008, 112.

26 J. S. Train, A. B. Wragg, A. J. Auty, A. J. Metherell, D. Chekulaev, C. G. P. Taylor, S. P. Argent, J. A. Weinstein and M. D. Ward, *Inorg. Chem.*, 2019, **58**, 2386–2396.

2.6 Appendix

2.6.1 Luminescence titration curves

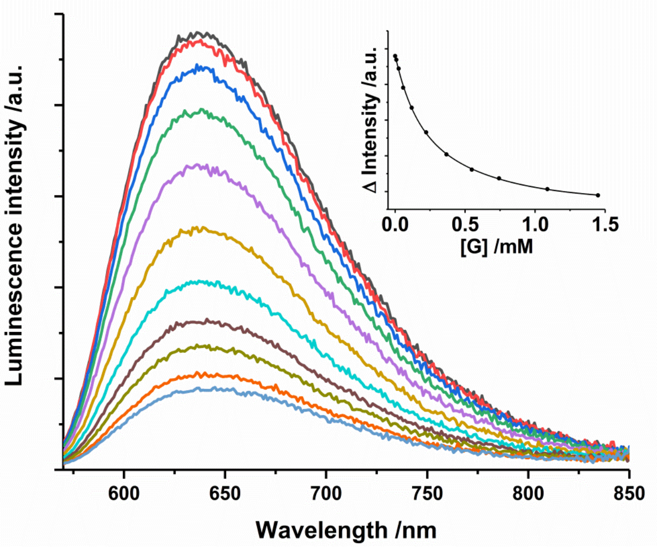

Figure 2.6.1: Luminescence titration of $[Os_4Zn_4(L^{nap})_{12}]Cl_{16}$ with 1,2,4,5-tetracyanobenzene as guest in H_2O, and an inset of the associated 1:1 binding curve.

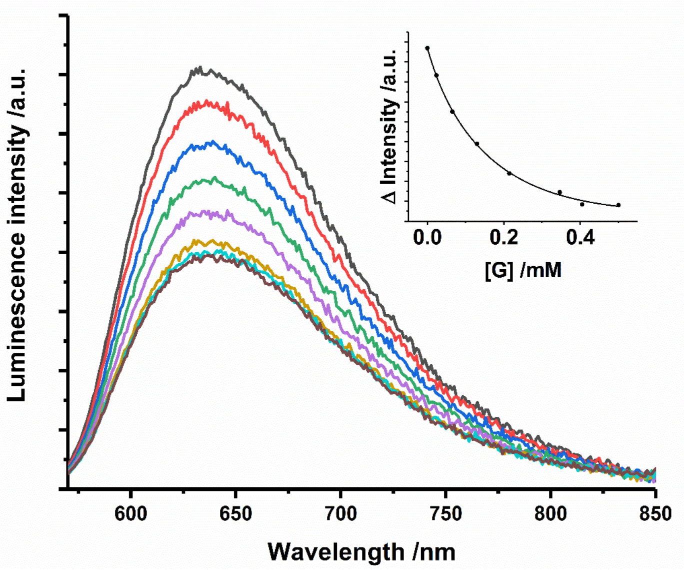

Figure 2.6.2: Luminescence titration of $[Os_4Zn_4(L^{nap})_{12}]Cl_{16}$ with 1-nitronaphthalene as guest in H_2O, and an inset of the associated 1:1 binding curve (quenching limited by solubility).

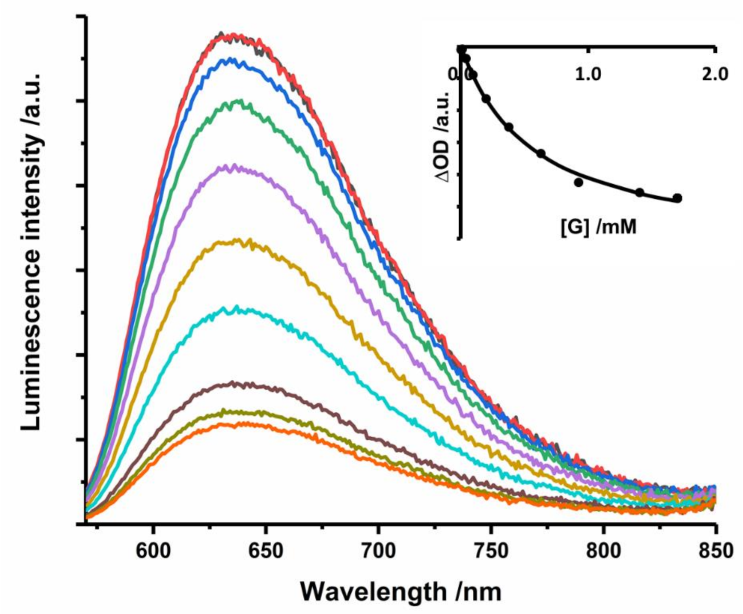

Figure 2.6.3: Luminescence titration of $[Os_4Zn_4(L^{nap})_{12}]Cl_{16}$ with 3-nitrobenzyl alcohol as guest in H_2O, and an inset of the associated 1:1 binding curve.

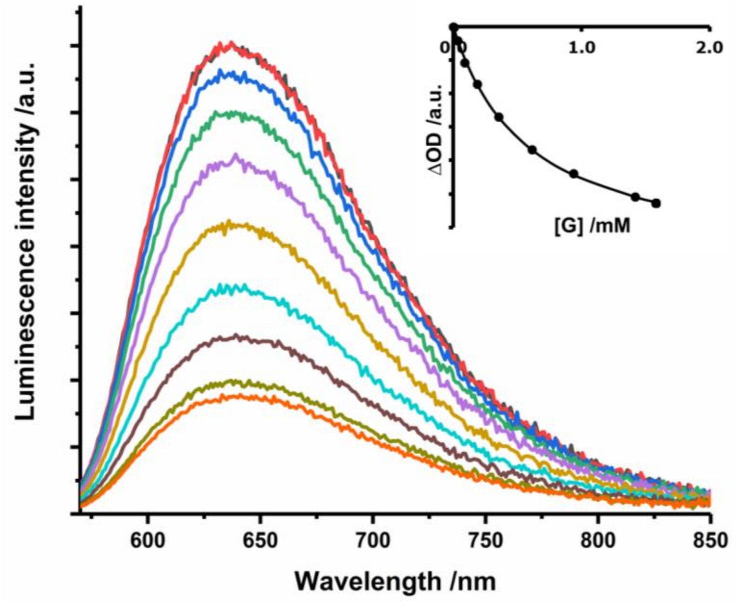

Figure 2.6.4: Luminescence titration of $[Os_4Zn_4(L^{nap})_{12}]Cl_{16}$ with 3-methyl-4,5-dinitrobenzyl alcohol as guest in H_2O, and an inset of the associated 1:1 binding curve.

2.6.2 X-ray crystallography data

Table 2.6.1: *Crystal data and structure refinement for* ***Os•Zn*** *(perchlorate salt).*

Nominal formulation	$[Os_4Zn_4(L^{nap})_{12}](ClO_4)_{16}•2MeNO_2•4H_2O$
Empirical formula	$C_{338}H_{278}Cl_{16}N_{74}O_{72}Os_4Zn_4$
Formula weight	8117.80
Temperature	100(2) K
Wavelength	0.71073 Å
Crystal system	Trigonal
Space group	R-3
Unit cell dimensions	a = 28.814(2) Å α = 90° b = 28.814(2) Å β = 90° c = 52.971(4) Å γ = 120°
Volume	38087(6) $Å^3$
Z	3
Density (calculated)	1.062 Mg/m^3
Absorption coefficient	1.328 mm^{-1}
Crystal size	0.32 x 0.21 x 0.16 mm^3
Theta range for data collection	0.902 to 19.826°
Index ranges	-27<=h<=27, -24<=k<=27, -50<=l<=49
Reflections collected	86465
Independent reflections	7688 [R(int) = 0.1465]
Completeness to theta = 19.826°	99.6 %
Absorption correction	Semi-empirical from equivalents
Refinement method	Full-matrix least-squares on F^2
Data / restraints / parameters	7688 / 582 / 726
Goodness-of-fit on F^2	1.616
Final R indices [$I > 2\sigma(I)$]	R1 = 0.134, wR2 = 0.393
R indices (all data)	R1 = 0.193, wR2 = 0.438

Data were collected at the University of Sheffield on a Bruker Apex II diffractometer with a CCD detector. CCDC deposition number: 1871131 14

Table 2.6.2: *Crystal data and structure refinement for* $[Co_8(L^{nap})_{12}](BF_4)_{16}$•*0.66(TCNB).*

Nominal formulation	$[Co_8(L^{nap})_{12}](ClO_4)_{16}$•$(TCNB)_{0.66}$•$(MeOH)_{38}(H_2O)_2$
Empirical formula	$C_{380.4}H_{421.3}N_{74.6}O_{40}B_{16}Co_8$
Formula weight	8538.07
Temperature	100(2) K
Wavelength	0.6889 Å (synchrotron)
Crystal system	Monoclinic
Space group	*C*2/c
Unit cell dimensions	a = 32.99046(15) Å α = 90˚ b = 29.89184(14) Å β = 95.8843(4)˚ c = 39.71423(18) Å γ = 90˚
Volume	38957.7(2) $Å^3$
Z	4
Density (calculated)	1.456 Mg/m^3
Absorption coefficient	0.41 mm^{-1}
Crystal size	0.80 x 0.70 x 0.16 mm^3
Theta range for data collection	0.89 to 36.091˚
Index ranges	-55<=h<=54, -50<=k<=49, -64<=l<=67
Reflections collected	420787
Independent reflections	94621 [R(int) = 0.058]
Completeness to theta =	92.8 %
Absorption correction	Semi-empirical from equivalents
Refinement method	Full-matrix least-squares on F^2
Data / restraints / parameters	94621 / 5859 / 2331
Goodness-of-fit on F^2	0.974
Final R indices [$I > 2\sigma(I)$]	R1 = 0.080, wR2 = 0.259
R indices (all data)	R1 = 0.132, wR2 = 0.292

Data were collected at beamline i-19 at the Diamond Light Source. CCDC deposition number: 1884249

Chapter 3

Photoinduced Electron Transfer Between an Os(II) Cage and Bound Guests

3.1 Introduction

Photoinduced electron transfer from the array of chromophores in a cage assembly, to bound guests, is an important topic to study as it can give rise to the possibility of new photo-catalytic reactions of host/guest complexes. As the inside of a cage is quite a different environment from the bulk solution phase where reactions normally happen, reactions that can occur in this environment have the potential to follow different pathways from those occurring in the bulk solution.[1] Combining this with the availability of chromophores incorporated in the cage structure means that, with the possibility of cage-to-guest photoinduced electron transfer new avenues can be opened in the area of photochemistry and photocatalysis. For this to be possible, we first need to demonstrate that photoinduced electron transfer can occur within the host/guest systems.

To do this, and detect potentially very short-lived species, pump-probe techniques can be employed. Pump-probe spectroscopy is used to study the dynamic processes in chemical compounds.[2] It operates by 'pumping' the desired complex with a short-lived pulse of electromagnetic radiation to produce the excited state, and then detecting ('probing') the resultant excited state with a separate pulse at a range of different time delays after the excitation.[3] Also known as transient absorption spectroscopy, this technique is used to observe the dynamics and electronic properties of the excited state in question. Often this may just be information on the lifetime of the excited state, which corresponds to how long it takes for the charges to recombine and the transient absorption signal associated with the excited state to disappear. This information is very useful for understanding how complexes interact with light and the processes that are involved with this.

3.1.1 Previous group work

Previous work in the group has included the study of an octanuclear cadmium-based cage ($[Cd_8(L^{napW})_{12}]^{16+}$), which has naphthalene-based emission from the array of twelve ligands.[4] This cage has been shown to perform photoinduced electron transfer or photoinduced energy transfer to bound guests. Fluorescence titrations showed quenching of the cage fluorescence on titration with energy- or electron-accepting guests which occupy the cavity. In addition, in in one instance, UV/vis transient absorption spectroscopy demonstrated the appearance of a short-lived charge-separated (naphthyl)$^{\bullet+}$/(TCNB)$^{\bullet-}$ state arising from cage-to-guest photoinduced electron-transfer following excitation of the naphthyl groups.[4]

3.1.2 Aim

From the work in chapter 2, given the substantial quenching of the cage luminescence (**Os•Zn**), in the presence of appropriate guests, the studies reported in this chapter explore the excited-state behaviour of the **Os•Zn** cage and the cage/guest assemblies using ultrafast UV/vis transient absorption (TA) spectroscopy. Due to the relative redox potentials of **Os•Zn** and the guests (the excited-state Os unit is a good electron donor and the guests are good electron acceptors), we would expect PET to occur from the cage to the guest, generating charge-separated H^+/G^- pairs (scheme 3.1.1). These can then be detected using TA spectroscopy and their lifetimes measured, as the characteristic spectroscopic signatures of the radical species that are formed can be probed and analysed. These results can then inform further potential developments, such as possible photo-redox catalysis or simultaneous multiple electron transfer. In this work, the transient absorption experiments were performed in aqueous solutions, with ~40 fs pulses at 400 nm excitation wavelength.

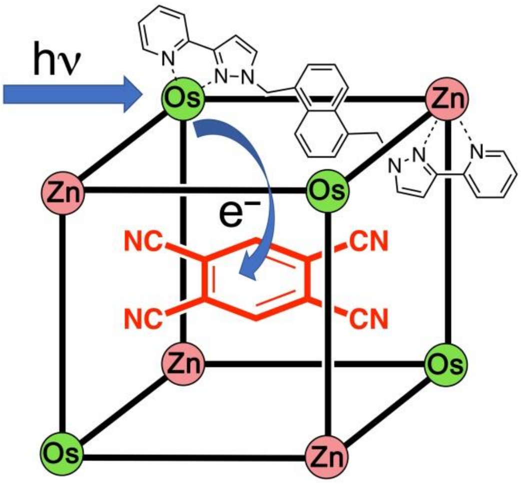

Scheme 3.1.1: Scheme to show general process of guest encapsulation and photoinduced electron transfer between host and guest.

3.2 Results and Discussion

3.2.1 Transient absorption studies of Os•Zn and Os(L^{me})$_3$

Firstly, UV/Vis transient absorption spectra of **Os•Zn** were recorded. The aqueous cage solution was excited at 400 nm, using 3 mW / 40 fs pulses, and probed in the UV/vis absorption range (350-700 nm) at a sequence of time delays up to 7.5 ns after excitation. The set of spectra shown in figure 3.2.1 was produced. The major bleaches at 425 nm and 490 – 590 nm reflect the loss of the MLCT absorptions of the ground state absorption spectrum, whereas the peaks at 360 nm and 620 nm are associated with new transient species being formed. The absorption at 360 nm has been tentatively assigned to the pyridyl-pyrazole$^{•-}$ (pypz) radical anion as this is the spectral region characteristic of ligand-centred radicals: however, there is no definite confirmation of this assignment, as the reduction of pypz complexes is irreversible, so they cannot be investigated by spectro-electrochemistry. Nevertheless, we would expect changes in the π-π* absorption manifold in the UV/Vis region when a ligand is transiently reduced to its radical anion in the excited state.

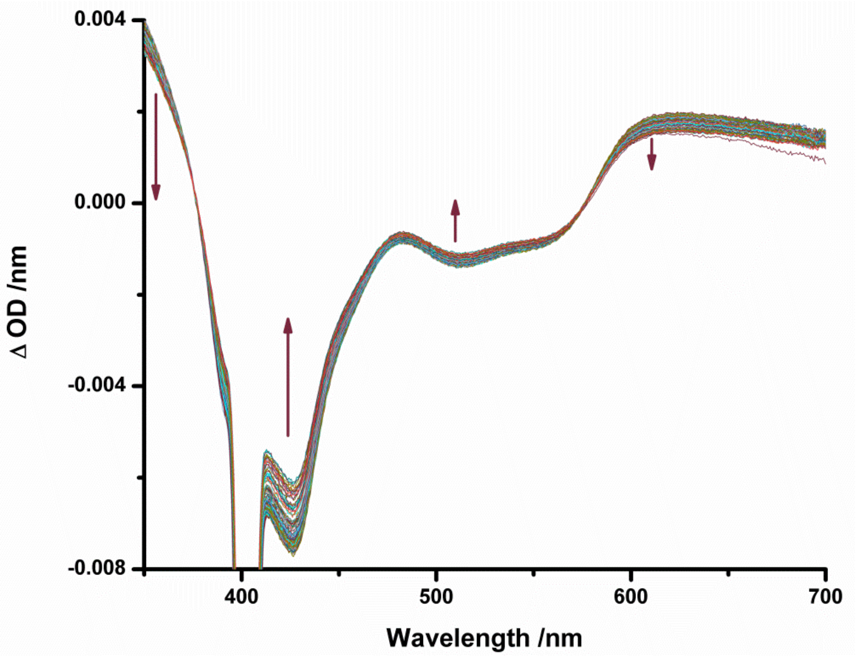

Figure 3.2.1: Transient absorption spectra of **Os•Zn** at a series of time delays from 1 ps - 5 ns in H_2O, following 400 nm, 40 fs pulse excitation.

Assignment of the 620 nm excited-state absorption comes from the analysis of previous spectro-electrochemical studies of an analogous cage, $[Os_4Cd_4(L^{nap})_{12}](ClO_4)_{16}$, performed by Ashley Wragg (figure 3.2.2). This experiment showed the formation of the Os^{III} cage species using UV/vis absorption spectroscopy. As is clear in figure 3.2.2a, the Os^{II}-based MLCT bands at 400-600 nm reduce in magnitude and a new band relating to the Os^{III} oxidised species appears at ~650 nm. This difference is made even clearer when the Os^{II} cage spectrum is subtracted from that of the Os^{III} cage (figure 3.2.2b): the changes in the spectra following metal-centred oxidation now match the appearance of the TA spectrum in figure 3.2.1. Therefore, the transient at 620 nm can reasonably be assigned to the transient oxidation of an Os^{II} vertex to Os^{III} in the MLCT excited state.

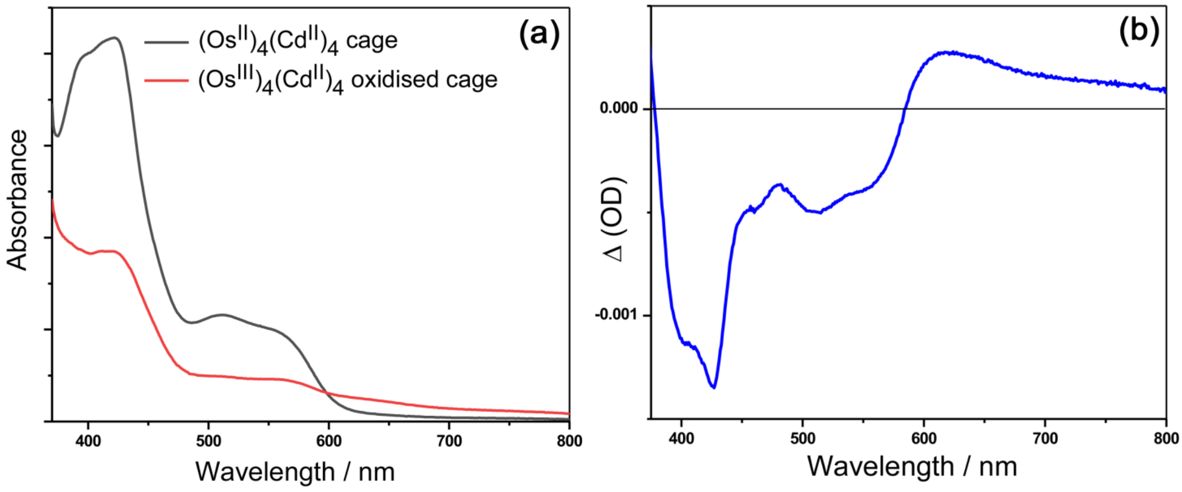

Figure 3.2.2: (a) UV/Vis spectra of the Os_4Cd_4 cage in the fully reduced Os^{II} form (black), and the fully oxidised Os^{III} form (red). (b) Difference between the two UV/Vis spectra showing spectroscopic changes associated with oxidation of Os^{II} to Os^{III}.

To study the kinetics of the **Os•Zn** cage excited state, global analysis was performed on the TA data, using the program Glotaran v.1.5.1.[5] The lifetime data could be fitted to a 3-component model. A long-lived (>50 ns) component is ascribed to the normal slow decay of the ^{3}MLCT excited state. In principle this lifetime should match what we see form luminescence emission (337 ns, chapter 2). A large difference in these two values is expected however, as the short 5 ns time scale of the TA experiment cannot extrapolate the data for a large enough time period to give an accurate (337 ns) value of this very long-lived component.

The global analysis of the data also revealed two additional faster processes that were not detected by time-resolved luminescence measurements, one with a lifetime of <1 ps and the other with a lifetime of ~1 ns. The shorter of these lifetimes is likely to be due to vibrational cooling;[6] and the 1 ns component is proposed to be due to a structural distortion of the metal coordination sphere in the excited state, which decays fairly slowly due to the rigidity of the cage structure. Figure 3.2.3 shows the decay-associated spectra of the complex, *i.e.* the absorption profile associated with each of the lifetime components of the system.

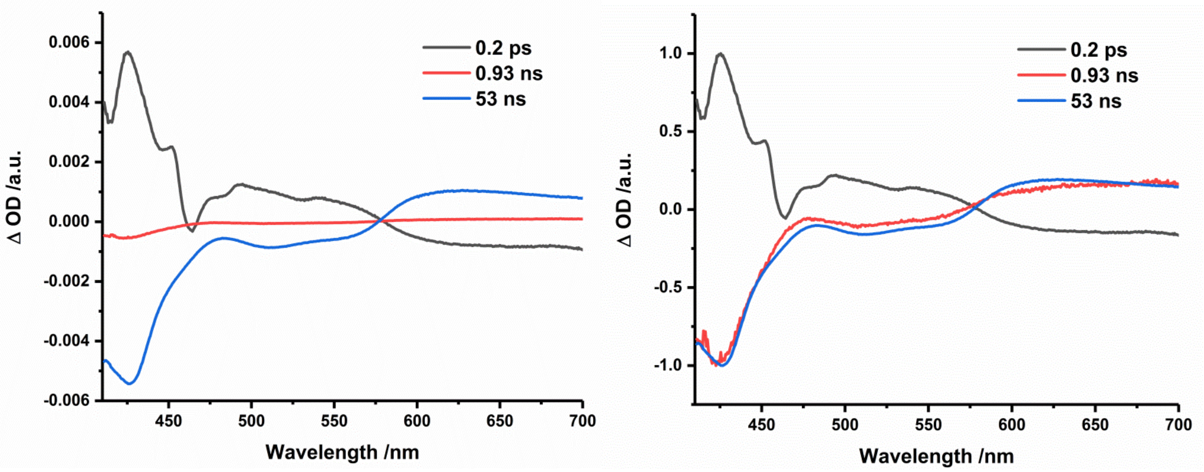

Figure 3.2.3: Decay-associated spectra for the free cage Os•Zn in aqueous solution fitted to a 3-component sequential model. The figure on the left shows the original spectra, whereas the figure on the right is normalised.

The mononuclear complex $[Os(L^{me})_3]Cl_2$ is a good mononuclear model for the Os^{II} corner units of the cage, and its behaviour can be compared with those of **Os•Zn** to determine the origins of the excited state behaviour. Figure 3.2.4 shows the set of TA spectra at different time delays after excitation of $[Os(L^{me})_3]Cl_2$, which are very similar to the spectra of **Os•Zn**, with the same bleaches at 435 and 490-590 nm, as well as the equivalent transients at 360 nm and 620 nm, showing the typical formation and decay of a ^{3}MLCT state.

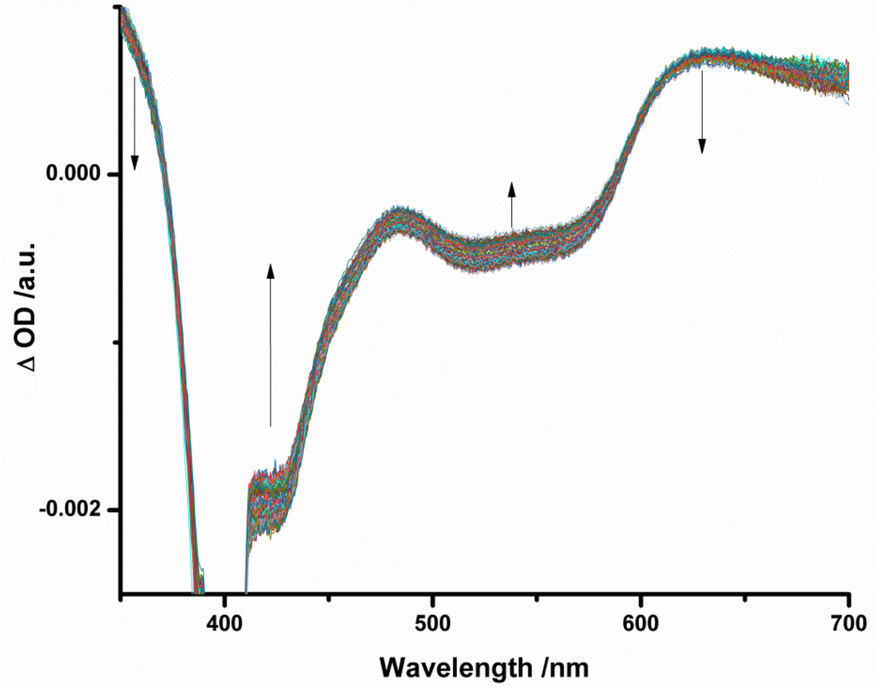

Figure 3.2.4: Transient absorption spectra of [Os(L^{me})$_3$]Cl_2 at a series of time delays from 1 ps - 5 ns in H_2O, following 400 nm, 40 fs pulse excitation.

As with **Os•Zn**, the transient spectrum does not decay completely within the 5 ns time scale, with neither the transients nor the bleaches returning fully to the ground state. This again suggests the presence of a much longer-lived component: as it has already been determined through emission experiments, from which the lifetimes of [Os(L^{me})$_3$]Cl_2 were found to be 97 and 206 ns (relating to the *fac* and *mer* isomers, chapter 2). For this work, the data was modelled using global analysis, with a 3-component model being used and the 2 long-lived components (97 and 206 ns) were fixed as just one long-lived component. Figure 3.2.5 shows the decay-associated spectra of [Os(L^{me})$_3$]Cl_2, in which the long lifetime component has fit to the value of 30 ns, and there are two shorter-lived species of 1 ps and 140 ps. Again, the shortest decay constant is attributed to vibrational cooling; and the 140 ps constant is potentially associated with a distortion of the metal coordination sphere in the excited state. Overall, the excited-state behaviour of the Os(II) centre in [Os(L^{me})$_3$]Cl_2 is very similar to that of the Os(II) centres in **Os•Zn**, which confirms that the naphthalene spacer of L^{nap} and the pendant pyrazolyl-pyridine units, that are coordinated to Zn(II) ions which complete the cage assembly, have very little effect on the photophysical properties of the Os^{II} units in the complete cage.

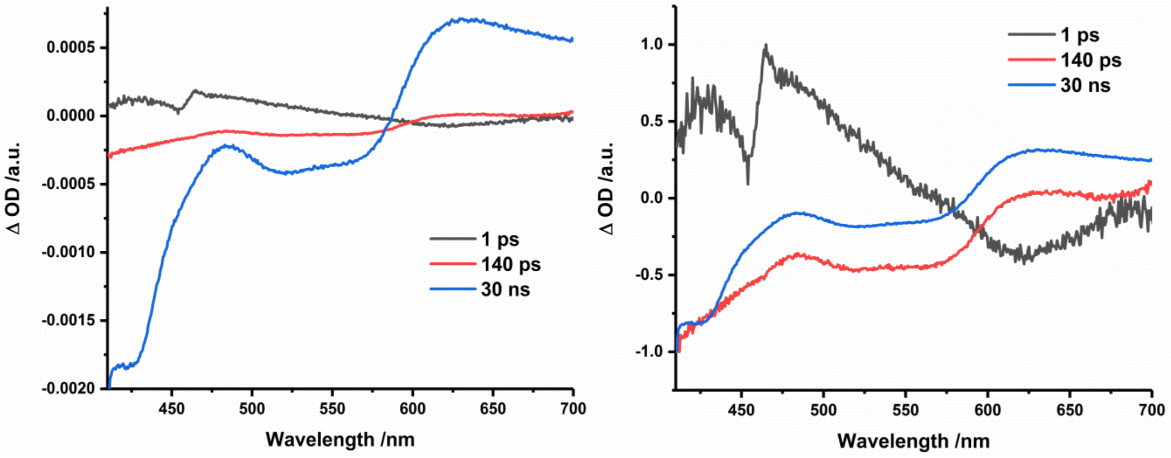

Figure 3.2.5: Decay-associated spectra for $[Os(L^{me})_3]Cl_2$ in aqueous solution fitted to a 3-component sequential model. The figure on the left shows the original spectra, whereas the figure on the right is normalised.

3.2.2 Photoinduced electron transfer within host/guest assemblies

As shown in chapter 2, it has been proven by NMR, luminescence spectroscopy and X-ray crystallography that a variety aromatic organic molecules can bind inside the **Os•Zn** cavity. For studying the photoinduced electron transfer in these cage/guest assemblies, there are some requirements of the guests as follows; they need to bind in the cage (size, shape, water solubility), they need to be sufficiently electron accepting (electron-deficient aromatic ring) and also that their associated radical anion has a characteristic absorption in the UV/visible region of the electromagnetic spectrum to allow detection by UV/Vis TA spectroscopy.

As discussed previously, when the guest binds in the cage and the cage is irradiated with light to photo-excite the Os(II) units, it is expected that photoinduced electron transfer will occur from the cage to the electron accepting guest, to form a cage$^{\bullet+}$/guest$^{\bullet-}$ state. Therefore, to observe this transition state, the absorption profile of the guest radical anion needs to be determined, as well as the oxidised cage profile. The latter was discussed in section 3.2.1, with the cage oxidation appearing at ~620 nm. For this work, 3 guests have been selected (as depicted in scheme 3.2.1), including 1,2,4,5-tetracyanobenzene (TCNB), 1,4-naphthoquinone (NQ) and 1-nitronaphthalene (NN). These guests are all of appropriate size and hydrophobicity to bind in the cage and their properties that were discussed in chapter 2 and are described in table 3.2.1. They are all sufficiently electron accepting to quench the Os-based MLCT excited state (reduction potentials <1.3 V vs. SCE).

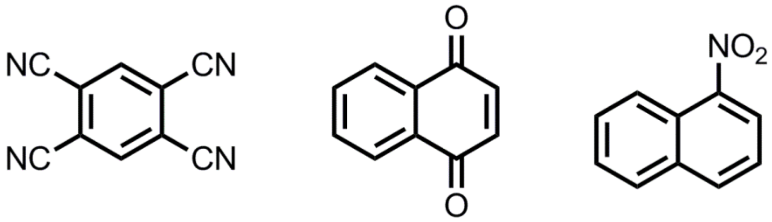

Scheme 3.2.1: Structural formulae of guests used in this work [1,2,4,5-tetracyanobenzene (TCNB), 1,4-naphthoquinone (NQ), and 1-nitronaphthalene (NN)].

Table 3.2.1: *Redox and photophysical properties of the three guest molecules; TCNB, NQ, NN, and their binding constants inside the cage cavity (all determined in this work, unless referenced).*

	E_{A/A^-} / V *vs.* SCE	***K* (lum) /M^{-1}**	***K* (NMR) /M^{-1}**	**λ_{max} /nm (G)**	**λ_{max} /nm (G radical anion)**
TCNB	-0.66[7]	4 x 10^3	3 x 10^3	300, 330[7]	462 (436, 414, 375, 354)[7]
NQ	-0.71[8]	2 x 10^3	2 x 10^3	340, 440[8]	390, 550[8]
NN	-0.99	8 x 10^3	3 x 10^3	340	465, 272

The absorption spectrum of each guest radical anion needs to be determined, so that the TA spectra of the $H^{\bullet+}/G^{\bullet-}$ states can be assigned. For TCNB and NQ these values were readily found in literature from previous studies on these molecules.7,8 However, for NN these values were less easily found, so a spectroelectrochemistry experiment was performed, where a solution of NN in acetonitrile was cooled to -20 °C and reduced *in situ* at a potential beyond its first reduction potential (-1.0 V) potential, until the absorption spectrum had stopped changing. The spectrum in figure 3.2.6 was achieved, which shows the neutral NN absorption as a dark grey line and the reduced species as a red line. There is a clear increase in absorption at 465 nm, where there is a new sharp peak, as well as an increased absorption at 220 nm.

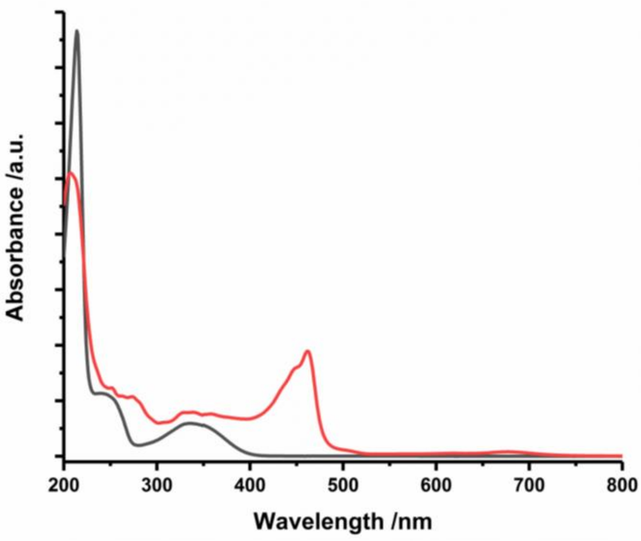

Figure 3.2.6: UV/Vis absorption data from a spectroelectrochemistry experiment showing neutral NN (black line) and the mono-reduced radical anion NN$^{\bullet-}$ (red line).

3.2.2.1 Transient absorption spectra of the host/guest assemblies

To perform the transient absorption studies on the host/guest complexes (H•G), a maximum concentration of guest (0.4-1.5 mM) was dissolved in cage solution (0.15 mM) in water, so that a significant proportion of cage molecules were filled with bound guest (>70%, determined through the individual binding constants (table 3.2.1)). Ideally, close to 100% of the cage would contain bound guest, however this was prevented by the lack of water solubility of the guests that limited the concentrations that could be achieved. To be consistent with the studies of free **Os•Zn**, all of the experiments were performed by exciting the solution at 400 nm, with 3mW / 40 ps pulses, and a random stepping order of delay times was used to minimise any compounding effects of probing the sample at consequent delay times. The delay periods were -5 to 5000 ps, and all of the solutions were stirred whilst the experiments were performed to minimise any spot degradation from the laser. The occurrence of any photoinduced electron transfer will be signalled by differences between the TA spectral features and the kinetic behaviour of free **Os•Zn** and the **Os•Zn**/guest complexes.

1,2,4,5-Tetracyanobenzene as guest

TCNB was the first guest to be studied, due to its high intensity sharp absorption band of the radical anion at around 460 nm. Upon excitation of the **Os•Zn**/TCNB complex, the TA spectra in figure 3.2.7 were observed, which on initial inspection, look very similar to that of the free cage **Os•Zn**. The strong excited-state absorption from the *ca.* 30% of unoccupied cage in the solution masks any less intense and shorter-lived cage/guest signals that may be occurring. However, when looking more closely, there is a small bulge in the TA spectra in the region of 450-460 nm, where you would expect to see a transient signal associated with the radical anion of the guest.

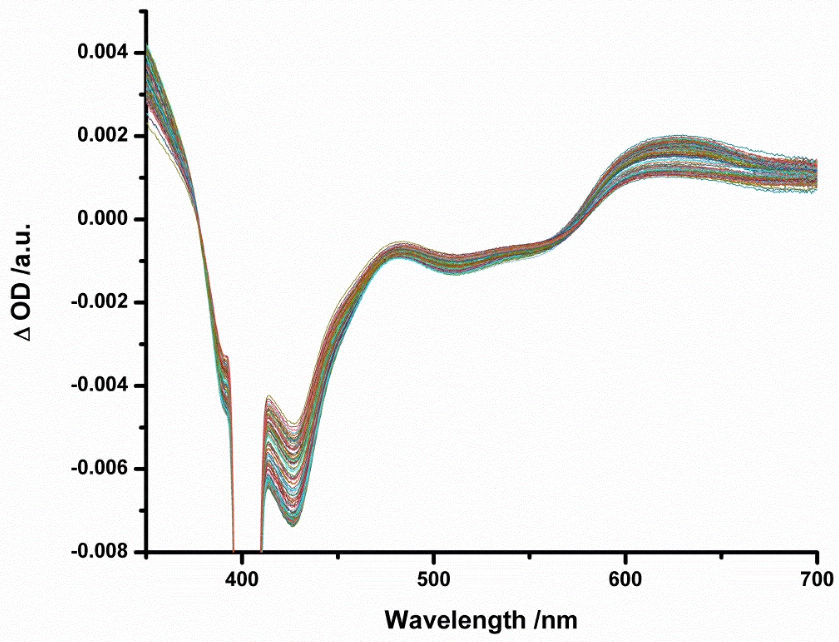

Figure 3.2.7: Transient absorption spectra of **Os•Zn**/TCNB at a series of time delays from 1 ps – 5 ns.

To determine if there is any indication of PET, further analysis needed to be completed to remove any contribution of the unoccupied cage. To do this, subtractions of the data were performed, taking the spectrum associated with the longest time delay (5 ns) from the spectra recorded at shorter delay times, to try to uncover any shorter-lived components. Figure 3.2.8 shows the result of this, starting at a minimum of 1 ps up to 1 ns, with arbitrary delays chosen in between. There is a large transient signal appearing at about 465 nm and a smaller peak at 640 nm. The peak at 465 nm clearly relates to the radical anion absorbance of TCNB (462 nm in the literature), and the broad peak at 640 nm can be assigned to the formation of Os^{III} as previously discussed. What is also clear is that there appears to be a grow-in of the 465 nm peak between 1 ps to 50 ps: it grows to maximum intensity by 50 ps and has decayed by 1 ns.

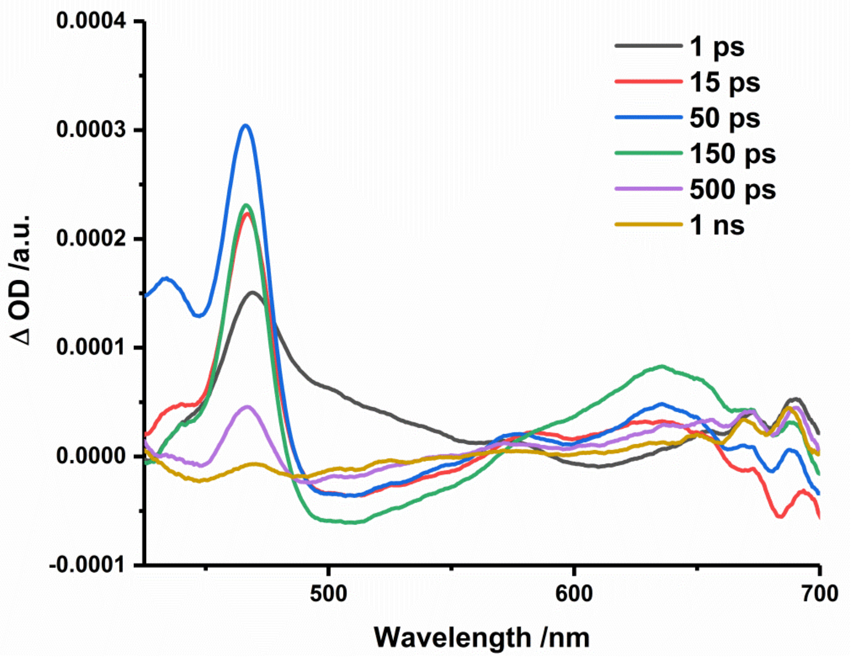

Figure 3.2.8: Spectral subtractions of **Os•Zn**/TCNB TA spectrum at 5 ns delay from various shorter time delays

To then uncover the decay kinetics of this state, global analysis was performed and the results compared with the kinetic behaviour of free **Os•Zn**. A 4-component model was fit (figure 3.2.9). A long lifetime component (>20 ns) was attributed to the unoccupied cage; and the sub-ps component was again assigned to vibrational cooling. In addition to these decay constants, two additional constants were associated with the spectra, with values of 40 ps and 170 ps. The shorter of these is assigned to the grow-in of the Os^{3+}/guest$^{\bullet-}$ charge-separated state, as a consequence of forward PET from the ^{3}MLCT state of one of the Os^{II} units of the cage to the guest molecule. The 170 ps component is then attributed to the decay of this Os^{3+}/guest$^{\bullet-}$ excited state by back electron-transfer and is consistent with "geminate recombination" of a short-lived charge-separated state. The spectral features of the decay-associated spectra associated with these lifetime components also confirms the assignment of the decay constants to these states, as we can see a negative bleach at 465 nm relating to the grow-in of the radical anion and a transient of the decay of this radical anion at 465 nm (similar to figure 3.2.8 above).

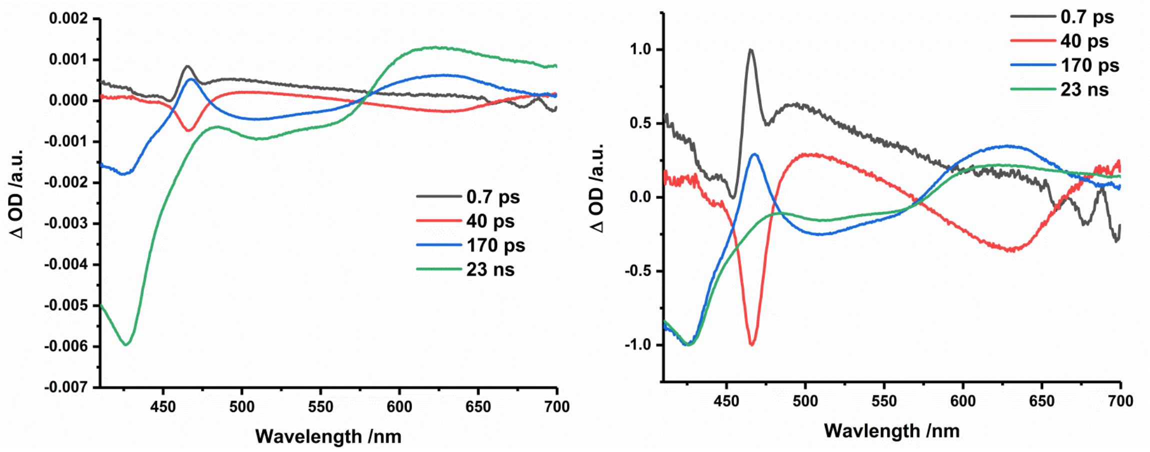

Figure 3.2.9: Decay-associated spectra (DAS) derived from TA data of **Os•Zn**/TCNB system showing the spectra associated with the four components of the global fit. Left: original DAS data, Right: normalised DAS with maximum positive and negative features fitting within a scale of ΔOD ±1.

To double check this assignment, single point kinetic analysis at 465 nm was also performed (figure 3.2.10) using Origin 2017 software. We can clearly see a grow-in of this signal until ~50 ps and then a decay which occurs over *ca.* 200 ps, subsequently leading into the long-lived decay of the ^{3}MLCT of **Os•Zn**. This complete set of analysis shows strong evidence for PET from the cage to the guest that was initially proposed.

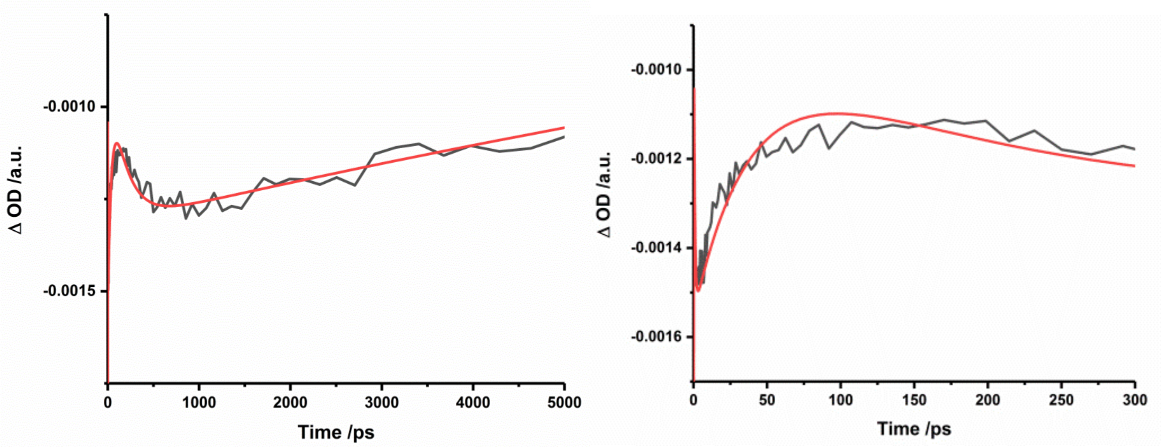

Figure 3.2.10: Left: observed single-point kinetics at 465 nm (black trace) with the result of the 4-component sequential global fit (red trace) superimposed. Right: an expansion of the early-time data showing the grow-in of the charge-separated state.

1,4-Naphthoquinone as guest

To extend the scope of this study two more cage/guest systems were analysed. The radical anion of 1,4-naphthoquinone (NQ) $^{\bullet-}$ has a very different anion absorption spectrum from that of (TCNB)$^{\bullet-}$: rather than a sharp absorption peak at *ca*. 460 nm it has a broader absorption band centred at 390 nm and a less intense broad band between 500 - 600 nm. Initially, it was hoped that the absorption band at 390 nm would be visible in the charge-separated excited state as it has a higher intensity than the broad band between 500 – 600 nm, however due to the sample being excited at 400 nm, the scatter from the excitation beam masked the 390 – 410 nm region in the TA spectrum, obscuring this signal.

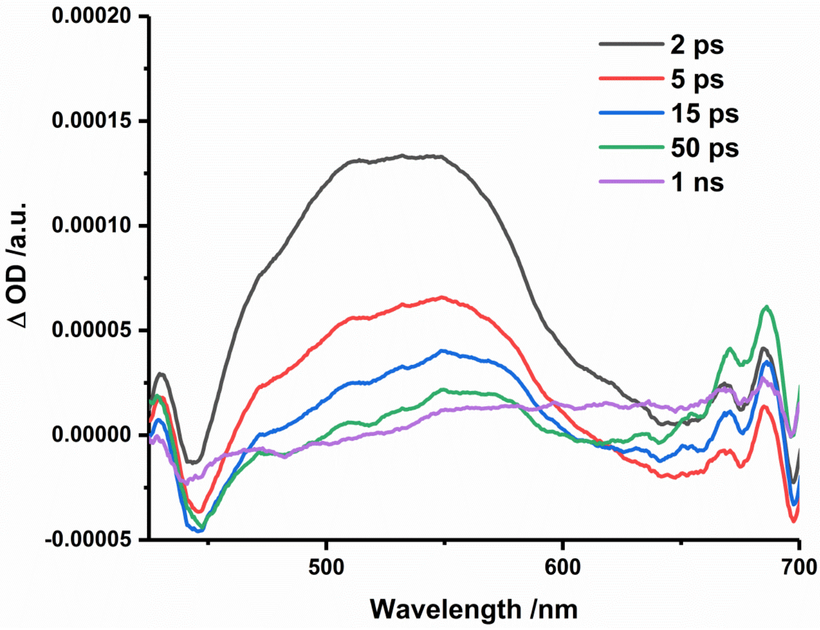

Figure 3.2.11: Spectral subtractions of **Os•Zn**/NQ TA spectrum at 5 ns delay from spectra recorded at various shorter time delays, revealing the absorption feature generated by the (NQ)$^{\bullet-}$ species

As shown with TCNB, no obvious differences were apparent in the primarily-generated TA data, between free **Os•Zn** and the **Os•Zn**/NQ systems, so careful subtractions of the data were once again necessary to detect any evidence of the Os^{3+}/guest$^{\bullet-}$ charge-separated state. Subtractions of the spectrum recorded after the longest time delay (5 ns) from the spectra recorded at a series of shorter time delays (figure 3.2.11), were performed and revealed a broad transient signal between 500 – 600 nm. This peak is consistent with the corresponding broad peak in the absorption spectrum of the radical anion of $(NQ)^{\bullet-}$.[8] In contrast to the **Os•Zn**/TCNB system, the **Os•Zn**/NQ system does not provide clear evidence of the expected grow-in of the charge-separated state. The reason for this is unclear, but it may be due to the lower intensity of the signal being monitored in the $(NQ)^{\bullet-}$ absorption spectrum.

To ascertain the kinetic profile of the **Os•Zn**/NQ system and to see if there is any evidence of a grow-in and decay of the $Os^{3+}/(NQ)^{\bullet-}$ state, global analysis was once again performed. A four-component model was fit - with the decay-associated spectra shown in figure 3.2.12. Once again, there is a long lifetime component of >20 ns associated with the free cage present in the cage/guest equilibrium; and a sub-ps lifetime component due to vibrational cooling. These are joined by a 14 ps component, which we can now attribute to the grow-in of the $Os^{3+}/(NQ)^{\bullet-}$ charge-separated state, and a 240 ps component attributed to the decay of $Os^{3+}/(NQ)^{\bullet-}$ by back electron-transfer. The shape of these spectra are harder to match to the absorption profile of free $NQ^{\bullet-}$, due to their broadness, as they do not stand out clearly against the background decay of unoccupied **Os•Zn** cage.

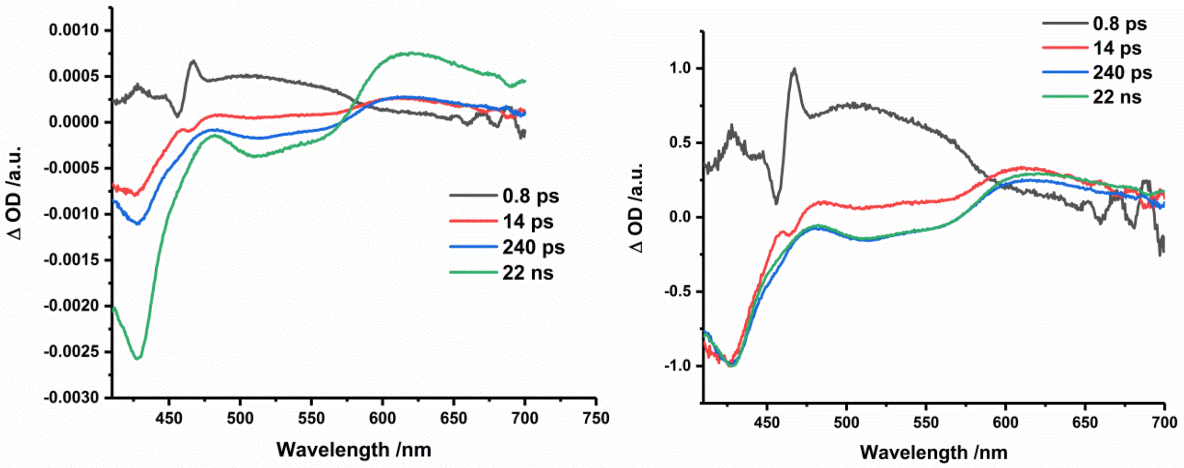

Figure 3.2.12: Decay-associated spectra (DAS) derived from TA spectroscopic data of the **Os•Zn**/NQ system showing the spectra associated with the four components of the global fit. Left: DAS data, Right: normalised DAS with maximum positive and negative features fitting within a scale of ΔOD ±1.

Single point kinetic analysis at 550 nm (the middle of the $NQ^{\bullet-}$ radical anion peak), was performed, which show a grow-in of the peak until ~20 ps and then a decay until ~500 ps (figure 3.2.13). This is in reasonable agreement with the DAS and shows comparable behaviour to the **Os•Zn**/TCNB system.

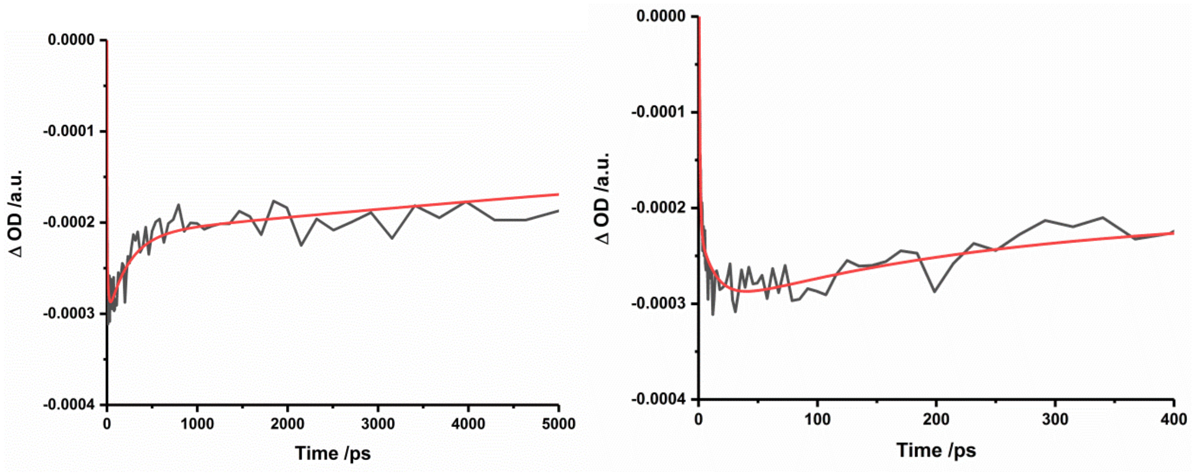

Figure 3.2.13: Left: observed single-point kinetics at 550 nm (black trace) with the result of the 4-component sequential global fit (red trace) superimposed. Right: an expansion of the early-time data showing the grow-in of the charge-separated state.

1-Nitronaphthalene as guest

1-nitronaphthalene (NN) was the final system to be tested and it proved challenging to use as a guest, due to its poor water solubility. Therefore, the concentration of NN that could be used was only 0.4 mM compared to 1.5 mM with TCNB and NQ. This meant that the fraction of **Os•Zn** cages that had guests bound was only 65 % compared to >77% for TCNB and NQ, meaning in turn that any signals arising from the **Os•Zn**$^{\bullet+}$/NN$^{\bullet-}$ charge-separated state should be weaker. Despite this, TA experiments were performed and, as before, subtractions of the TA spectrum recorded after a 5 ns delay, from spectra recorded with shorter time delays, was achieved (figure 3.2.14) and revealed a clear transient signal characteristic of NN$^{\bullet-}$. As expected from the spectro-electrochemistry experiment, this radical anion peak is at around 470 nm, confirming the presence of NN$^{\bullet-}$. In addition to this, there is a corresponding broad signal at 630 nm, which is assumed to be associated with the presence of Os^{3+}.

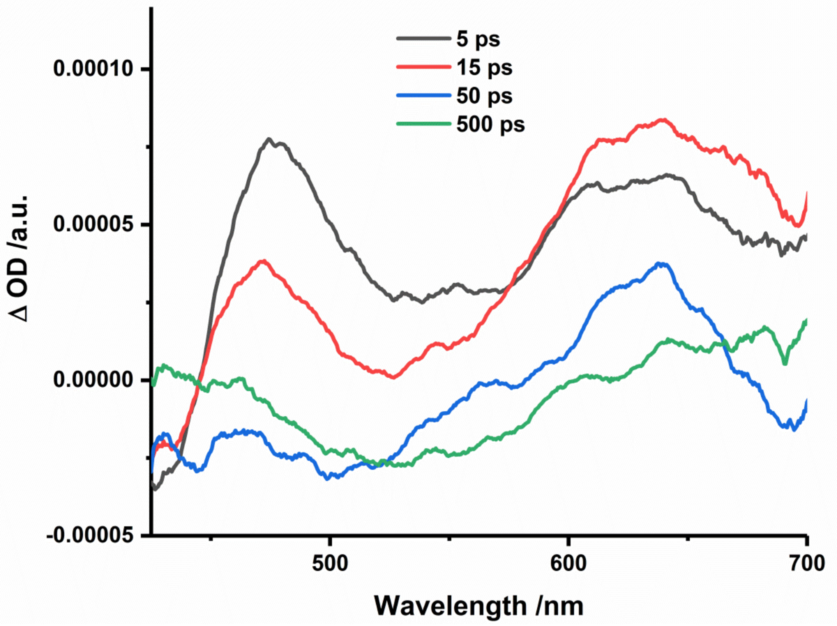

Figure 3.2.14: Spectral subtractions of **Os•Zn**/NN TA spectrum at 5 ns delay from various shorter time delays.

The time-resolved decay of the **Os•Zn**/NN complex was fit to a 4-component decay model, revealing four associated decay lifetimes (figure 3.2.15): unoccupied cage (67 ns), vibrational cooling (1.2 ps), grow-in of **Os•Zn**$^{\bullet+}$/NN$^{\bullet-}$ state (19 ps) and decay of **Os•Zn**$^{\bullet+}$/NN$^{\bullet-}$ state (225 ps). This behaviour is exactly similar to what was observed in the other two cage/guest systems with the grow-in and decay lifetimes for the charge-separated state consistent with what was observed using TCNB and NQ. With the spectra associated with these decays, there is the usual shape for the very short and long lifetime components; and we can also observe a maximum in the spectra of the 225 ps component at ~470 nm, which can be plausibly assigned to the transient signal of the NN$^{\bullet-}$ species.

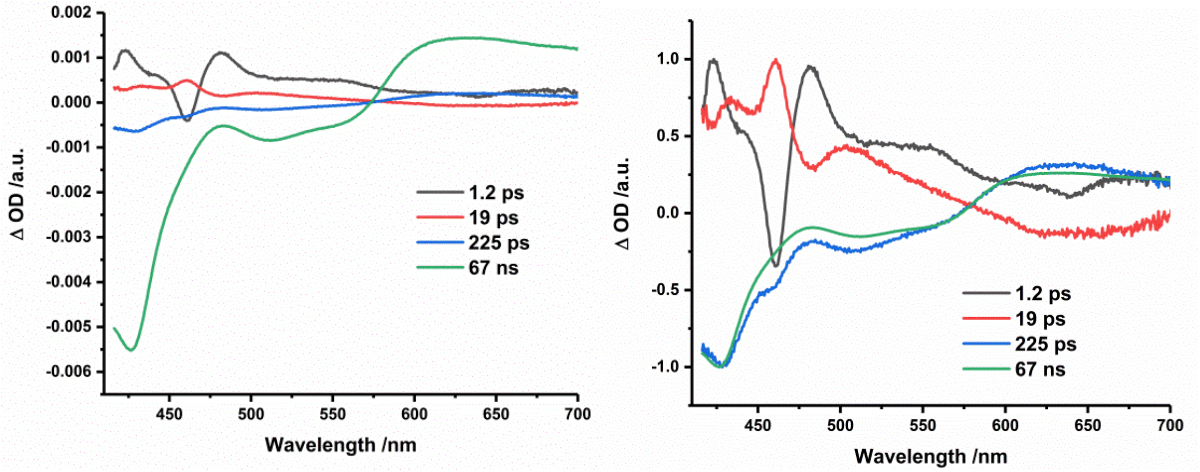

Figure 3.2.15: Decay-associated spectra (DAS) derived from TA spectroscopic data of the **Os•Zn**/NN system showing the spectra associated with the four components of the global fit. Left: original DAS, Right: normalised DAS with maximum positive and negative features fitting within a scale of ΔOD ±1.

The single point kinetic traces were also recorded for the peak at 470 nm, where once again a grow-in with a lifetime of ~20 ps is revealed, which then decays with a lifetime of ~200 ps, indicative of the "geminate recombination" of the charge-separated state (figure 3.2.16).

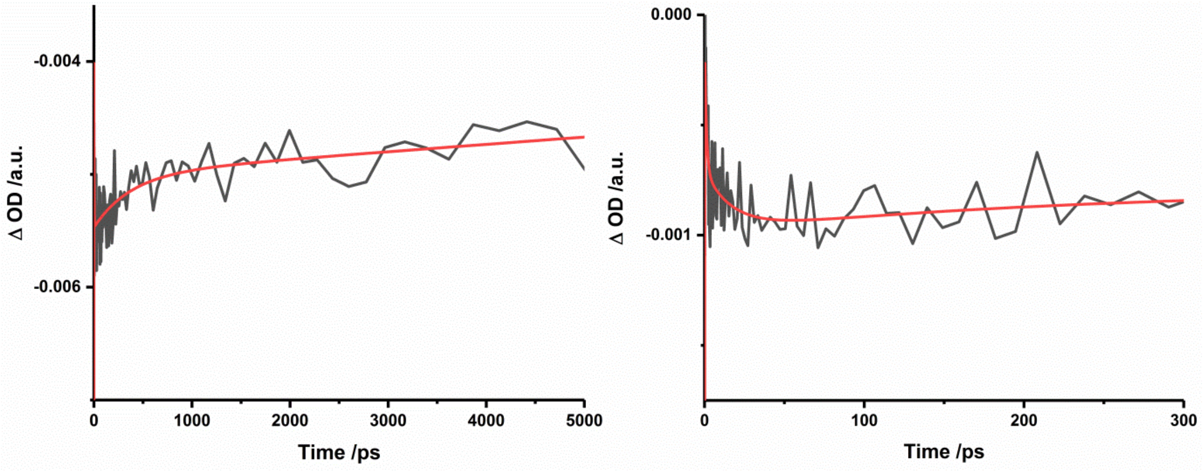

Figure 3.2.16: Left: observed single-point kinetics at 470 nm (black trace) with the result of the 4-component sequential global fit (red trace) superimposed. Right: an expansion of the early-time data showing the grow-in of the charge-separated state.

3.2.2.2 Comparison of three cage/guest assemblies

As a summary and comparison of the three different guest assemblies used, figure 3.2.17 shows the key transient signals of the charge-separated state, relating to the spectrum of the oxidised cage (Os^{3+} centre) cage cation and to the spectrum of each radical anion. This figure provides a clear illustration of the similarities/differences between the transient absorption spectra of the three cage/guest assemblies.

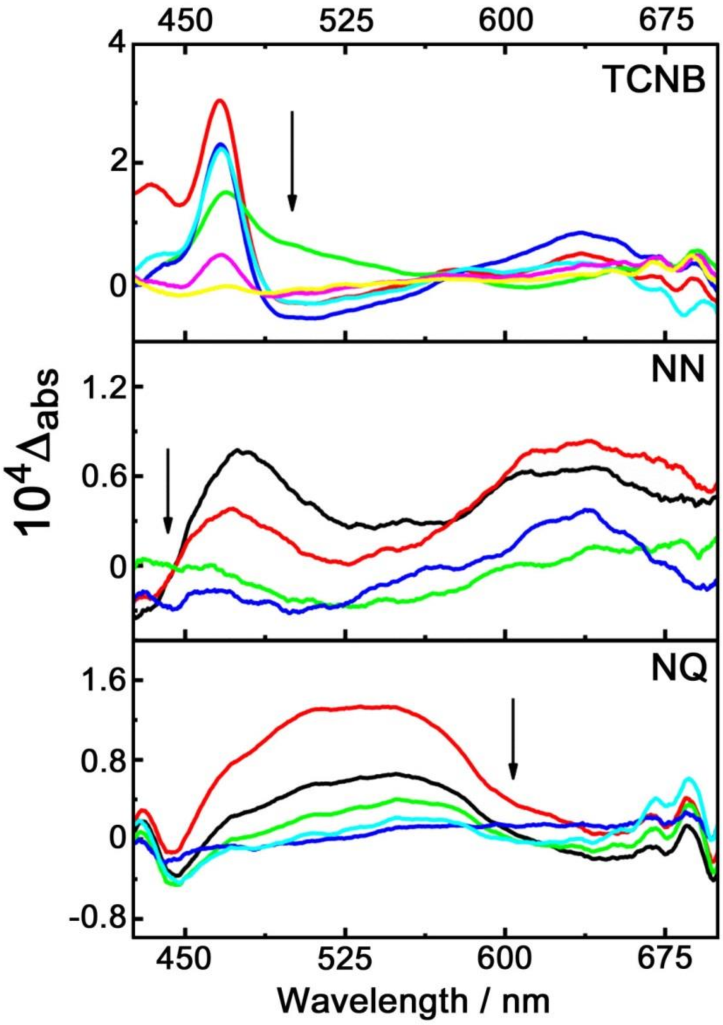

Figure 3.2.17: Transient absorption spectra obtained by subtracting spectra at selected shorter time delays (5 ps to 1 ns) from a spectrum with a time delay of 5 ns, for the complexes of **Os•Zn** with the 3 different guests (i) TCNB, (ii) NN and (iii) NQ. Arrows denote the direction of change with time.

Table 3.2.2 provides a summary of the lifetimes of the grow-in and decay processes of the charge-separated states. These values are from the analyses of different samples, which have all undergone multiple independent fits, and averaged to get a mean value and standard deviation. The values of these lifetimes are all within error of each other and the grow-in averages to ~20 ps, with the subsequent decay rate being ~200 ps. This would suggest that the same forward PET and geminate recombination processes are happening within each sample. The small variations in these values could be due to the different electron accepting ability of the guests (table 3.2.1), and different geometries for the cage/guest complexes.

Table 3.2.2: *Summary of lifetimes of the grow-in and decay of the* ***Os•Zn***$^{\bullet +}$*/guest*$^{\bullet -}$ *charge-separated state*

	Grow-in and decay lifetimes for Os^{3+}/G$^{\bullet -}$ state /ps
TCNB	21 ± 14 (grow-in) 205 ± 60 (decay)
NQ	13 ± 4 (grow-in) 185 ± 95 (decay)
NN	18 ± 5 (grow-in) 185 ± 75 (decay)

To fully analyse the appearance of the decay-associated spectra of the geminate recombination step, the respective decay associated spectra of the >20 ns constant was subtracted from the ~200 ps component for each of the 3 guests (figure 3.2.18). This analysis proves that the ~200 ps decay component is conclusively related to the disappearance of the transient of the TA spectrum of the charge-separated $Os^{3+}/G^{\bullet-}$ species in every case.

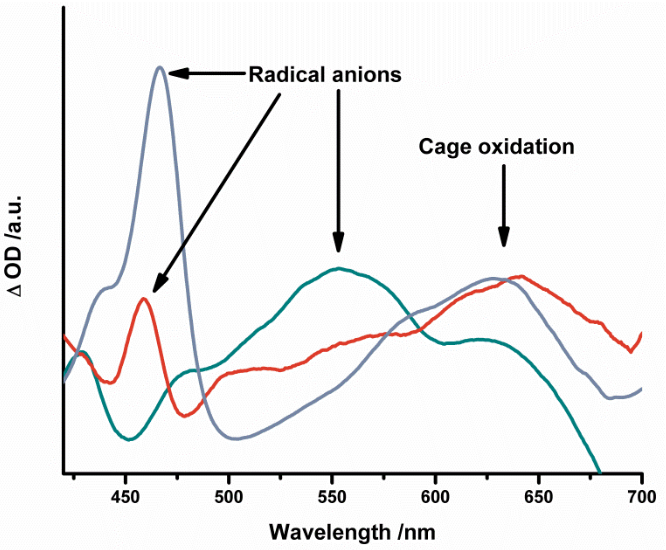

Figure 3.2.18: Excited-state spectra of each of the three Os•Zn/guest complex assemblies, obtained by subtracting the spectrum associated with the long decay constant from the spectrum associated with short decay constant to emphasize the short-lived components (TCNB, purple; NN, red; NQ, green).

3.2.2.3 Control experiments

Finally, control experiments were performed to confirm that the features in the TA spectra were due to PET in the cage/guest assemblies and not just from excitation of the guest alone. Control experiments also confirm that the charge-separated states arise because of the guest being bound inside the cage cavity and are not just associated with guest interaction with the external surface of the cage or by collisional interactions of the chromophore and quencher in solution.

Firstly, the guests were excited in TA experiments on their own, in an aqueous solution, without the presence of the cage, and probed using the same experimental conditions. As TCNB and NN don't absorb/absorb very minimally in the ground state at 400 nm the resultant spectra had no significant new peaks, and it can therefore be concluded that the $TCNB^{\bullet-}$ and $NN^{\bullet-}$ peaks observed in the presence of **Os•Zn** cage were not due to direct excitation of these guest molecules. NQ on the other hand, does absorb at 400 nm, however, as shown in figure 3.2.19, the transient feature that occurs is at 650 nm, which doesn't overlap with the 500 - 600 nm transient region that is present in the **Os•Zn**/NQ system. It is therefore clear that direct excitation of NQ was not responsible for the results discussed in section 3.2.2.

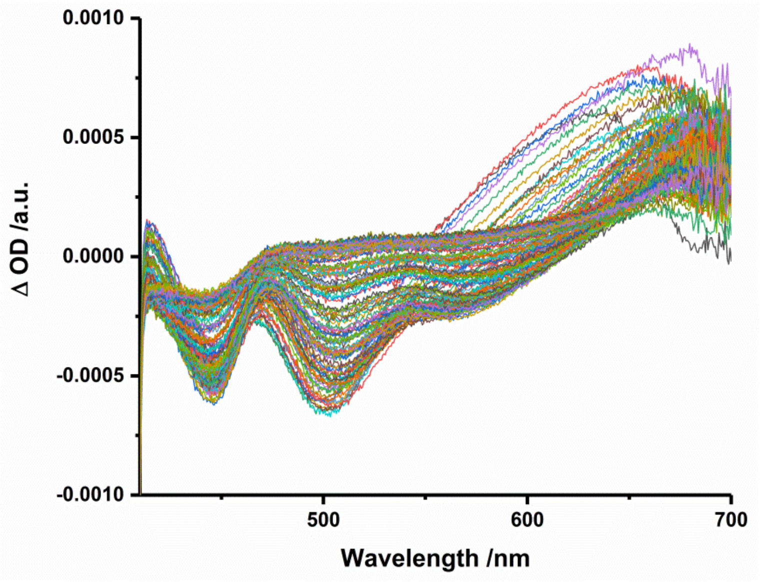

Figure 3.2.19: Transient absorption spectra of 1,4-naphthoquinone in water, at time delays of 1 ps – 5 ns.

Secondly, to prove that this excited state was being formed from interactions that are happening within the cage, as opposed to just collisional effects, a strongly binding non-redox active competing guest was added to the solution. Cylcoundecaonone (C_{11}) is known to bind in the cage with binding constants of the order of 10^6 M^{-1}, which is far higher to that of the guests used in this study, so will displace the other guests from the cage and allow the original free cage dynamics to be restored.

For this experiment, the **Os•Zn**/TCNB complex was used, as its charge-separated state showed the most prominent spectral differences compared to free **Os•Zn**, due to the sharp and intense absorption peak of $(TCNB)^{\bullet-}$ and the reasonable water solubility of this guest. Figure 3.2.20 (blue line) shows the single point kinetics of **Os•Zn**/TCNB at 460 nm after excitation, as seen before in figure 3.2.10, with clear grow-in and decays of the charge separated state. As well as this, the black line represents the single point kinetics of the empty **Os•Zn** cage at 460 nm, with the charge-separated state clearly being absent. The green line represents the single point kinetic curve recorded at 460 nm which is observed when cycloundecanone is added to the solution of **Os•Zn**/TCNB, displacing the guest from the cavity. From this, the loss of the short-lived grow-in and decay components of the charge-separated state are clearly apparent and the restoration of the free cage excited state kinetics is observed. This confirms that the ~20 ps and ~200 ps components in each case (*cf.* blue line in Fig. 3.2.20), are associated with PET from the cage to the guest inside the cavity and this does not occur when C_{11} is bound and the TCNB guest is free in solution.

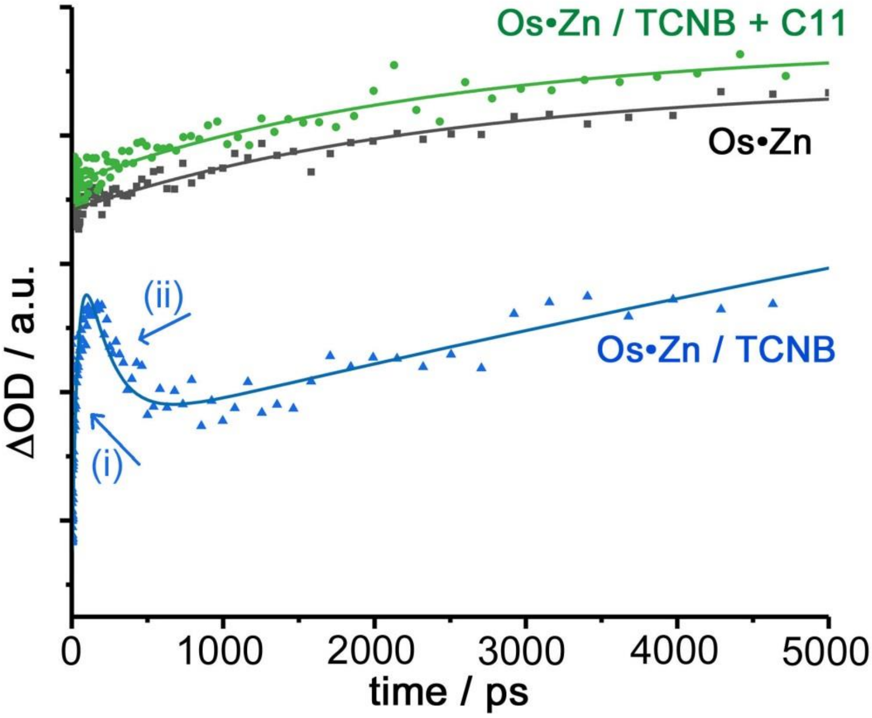

Figure 3.2.20: Excited state decay kinetics obtained from transient absorption spectroscopy data from the **Os•Zn**/TCNB complex in water, at 460 nm. The traces correspond to free **Os•Zn** (black); the **Os•Zn**/TCNB complex (blue); and **Os•Zn**/TCNB/cycloundecanone (green).

Finally, the results of the TA experiment from the **Os•Zn**/TCNB system were compared with those from a similar experiment on the $[Os(L^{me})_3]Cl_2$/TCNB. For this, **Os•Zn** was replaced with 4 equivalents of $[Os(L^{me})_3]Cl_2$, so that the same number of Os^{II} chromophores were present in solution and so that there was the same optical density of the solution upon excitation. Figure 3.2.21 shows the data subtractions that were a result of this, showing that there is no longer a peak at 465 nm associated with the $(TCNB)^{\bullet-}$ radical anion. This confirms that it is not only the presence of the Os^{II} chromophores in the cage, that accounts for the

$Os^{3+}/G^{\bullet-}$ excited state formation, and that the assembly of these chromophores into the cage structure is actually essential for the PET process to occur.

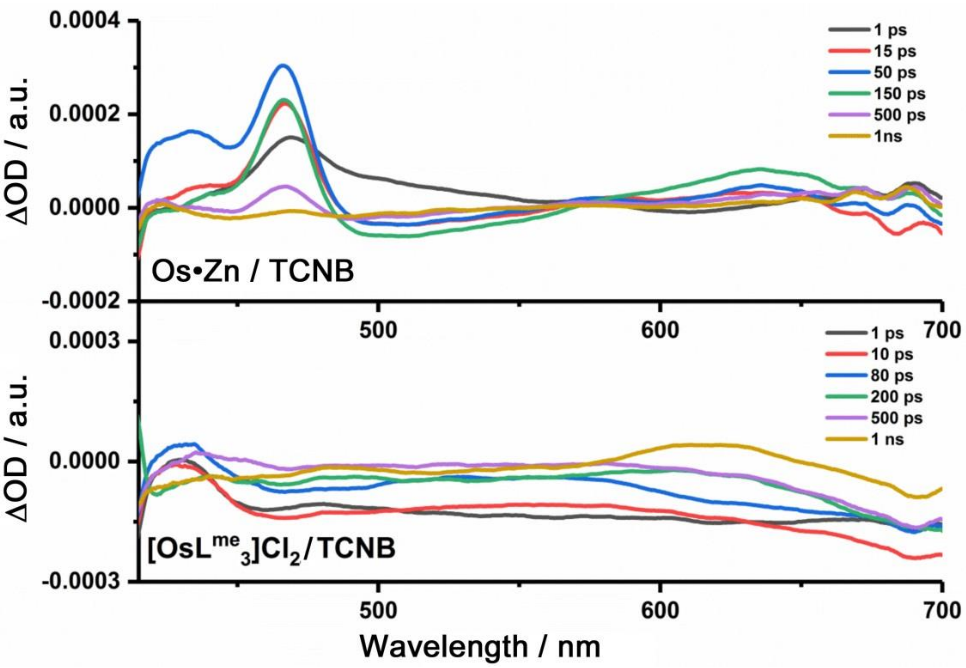

Figure 3.2.21: Transient absorption spectra obtained by subtracting the spectrum recorded of the longest time delay (5 ns) from the spectra at shorter time delays (1 ps to 1 ns). Top: **Os•Zn**/TCNB system. Bottom: $[Os(L^{me})_3]Cl_2$ /TCNB system.

3.3 Conclusions

The **Os•Zn** cage and $[Os(L^{me})_3]Cl_2$ complex exhibit similar transient absorption profiles, with long-lived decay kinetics (>20 ns) associated with decay of the expected ^{3}MLCT state, as well as shorter lived components (1 ns and 140 ps respectively), assigned tentatively to the distortion of the metal coordination sphere, as well as an additional sub-ps vibrational cooling component. The cage/guest assemblies are capable of effecting photoinduced electron-transfer from the **Os•Zn** cage to any of three different electron-deficient aromatic guests. These guests bind in the cage cavity, and in each case give an **Os•Zn**$^{\bullet+}$/guest$^{\bullet-}$ charge-separated state with a lifetime of ~200 ps. The transient absorption spectra identified spectral features associated with the guest radical anion for each system and separate grow-in and decay processes were seen for each of these states. Control tests proved that the guest needed to be bound inside the cage cavity for these processes to occur, because addition of a competing (photophysically innocent) guest removed the short-lived spectral features associated with **Os•Zn**$^{\bullet+}$/guest$^{\bullet-}$ formation and additionally, the control experiment where the cage was replaced with $[Os(L^{me})_3]Cl_2$ units, confirms this.

The ability of these photoactive cages to bind a guest in a cavity surrounded by multiple luminophores, and to then be involved in photophysical processes with bound guests, offers interesting possibilities in areas such as photoredox catalysis of bound guests, and even multiple accumulative electron transfer.

3.4 Experimental

3.4.1 Experimental techniques

UV/Vis Spectroelectrochemical measurements

Spectroelectrochemical measurements were performed using a home-built OTTLE cell in dry acetonitrile at 253 K,[9] with a Pt mesh working electrode, a Pt wire counter electrode and Ag wire pseudo-reference electrode. The UV/vis spectra were performed using a Cary 5000 spectrophotometer.

Transient Absorption Spectroscopy

The ultrafast transient absorption setup used consists of a commercial detection instrument (Helios, Ultrafast Systems) and the following laser system: a Ti:Sapphire regenerative amplifier (Spitfire ACE PA-40, Spectra-Physics) providing 800 nm pulses (40 fs fwhm, 10 kHz, 1.2mJ). Sample excitation was provided by doubling a portion of the 800 nm output, in a β-barium borate crystal within a commercially available doubler/tripler (TimePlate, Photop Technologies), yielding 400 nm pulses. White light supercontinuum probe pulses were generated *in situ* using a portion of the Ti:Sapphire amplifier output, focused onto a CaF_2 crystal, allowing for the generation of light spanning 340 nm – 720 nm. Detection was performed with a CMOS sensor for UV/Vis spectra. The pump and probe polarisations were set to a magic angle geometry. The data processing was performed using Origin 2017 and Glotaran 1.5.1.[5]

Samples were all made up in distilled water, with $[Os_4Zn_4(L^{nap})_{12}]Cl_{16}$ (0.15 mM) or $[Os(L^{me})_3]Cl_2$ (0.6 mM), and guests 1,2,4,5-tetracyanobenzene (1.5 mM), 1,4-naphthoquinone (1.5 mM) and 1-nitronaphthalene (0.4 mM).

3.5 References

1 J. Guo, Y.-W. Xu, K. Li, L.-M. Xiao, S. Chen, K. Wu, X.-D. Chen, Y.-Z. Fan, J.-M. Liu and C.-Y. Su, *Angew. Chemie Int. Ed.*, 2017, **100191**, 3852–3856.

2 S. Archer and J. A. Weinstein, *Coord. Chem. Rev.*, 2012, **256**, 2530–2561.

3 J. Best, I. V Sazanovich, H. Adams, R. D. Bennett, E. S. Davies, A. J. H. M. Meijer, M. Towrie, S. A. Tikhomirov, O. V Bouganov, M. D. Ward and J. A. Weinstein, *Inorg. Chem.*, 2010, 10041–10056.

4 J. R. Piper, L. Cletheroe, C. G. P. Taylor, A. J. Metherell, J. A. Weinstein, I. V. Sazanovich and M. D. Ward, *Chem. Commun.*, 2017, **53**, 408–411.

5 J. J. Snellenburg, S. P. Laptenok, R. Seger, K. M. Mullen and I. H. M. van Stokkum, *J. Stat. Softw.*, 2012, **49**, 1.

6 M. Delor, I. V Sazanovich, M. Towrie, S. J. Spall, T. Keane, A. J. Blake, C. Wilson, A. J. H. M. Meijer and J. A. Weinstein, *J. Phys. Chem. B*, 2014, **118**, 11781–11791.

7 M. Fagnoni, S. Protti, D. Ravelli and A. Albini, *Beilstein J. Org. Chem.*, 2013, 800–808.

8 I. Amada, M. Yamaji, S. Tsunoda and H. Shizuka, *J. Photochem. Photobiol. A Chem.*, 1996, **95**, 27–32.

9 S. Lee, R. Kowallick, M. Marcaccio, J. A. Mccleverty and M. D. Ward, *Dalt. Trans.*, 1998, 3443–3450.

Chapter 4

Photophysical Interactions and Binding of Aryl Disulfides in Cubic Cages

4.1 Introduction

Single electron transfer has been well studied for many years, with photo-induced electron transfer reactions being some of the best understood processes in chemistry.[1] While single electron transfer is important in many chemical and biological systems, the exploration of electron transfer (ET) is developing from single one-electron reactions to coupled multistep and multi-particle processes, for example, multi-electron redox chemistry. Multi-electron events are vital for the applications of molecular electronics, solar energy conversion and fuel cells.[1] Biological enzymes partake in multi-electron catalysis, for example, cytochrome oxidase reduces O_2 by four electrons; these reactions are very complex and the enzymes organise multi-electron delivery and stabilize reactive intermediates, as well as coupling covalent bond chemistry.[1]

Coupled electron transfer reactions also play a key role in biological energy conversion processes, most importantly the synthesis of adenosine triphosphate (ATP) from adenosine diphosphate (ADP) using primary energy sources (*e.g.* light/food).[2] Multi-electron transfer is also of upmost importance for solar energy photochemistry, e.g. CO_2 reduction and water oxidation, which are multi-electron redox processes.[3] For these reasons, the research into multi-electron processes in both molecules and molecular assemblies is a topic of high current importance.

One area that is of key interest is the competition between sequential and concerted mechanisms. Stepwise ET mechanisms typically occur through the process summarised in equation 1, where two-electron transfer happens through the formation of an intermediate radical anion, or less typically through equation 2, which mimics a concerted mechanism (equation 3), where both one-electron transfer steps occur within a collision complex and no evidence of a radical anion reaction intermediate appears.[4]

$$D^{2-} + A \leftrightharpoons [D^{2-}\cdots A] \leftrightharpoons [D^{-}\cdots A^{-}] \leftrightharpoons D^{-} + A^{-} \leftrightharpoons [D^{-}\cdots A^{-}] \leftrightharpoons [D\cdots A^{2-}] \leftrightharpoons D + A^{2-} \tag{1}$$

Conventional stepwise mechanism

$$D^{2-} + A \leftrightharpoons [D^{2-}\cdots A] \leftrightharpoons [D^{-}\cdots A^{-}] \leftrightharpoons [D\cdots A^{2-}] \leftrightharpoons D + A^{2-} \tag{2}$$

Unconventional stepwise mechanism

$$D^{2-} + A \leftrightharpoons [D^{2-}\cdots A] \leftrightharpoons [D\cdots A^{2-}] \leftrightharpoons D + A^{2-} \tag{3}$$

Concerted mechanism

In photo-redox catalysis, multi-electron transfer can potentially lead to products that are inaccessible via single-electron transfer mechanisms. The aim of this work is to use the cage to bind a substrate in the cavity so that it is close to a large number of sensitisers (much higher effective local concentration than in solution). This will then allow multiple photo-induced electron transfer (PET) to/from a guest, thus opening up the possibility of a wide range of photo-induced reactions. The transfer of two (or more) electrons to a single acceptor is a major challenge in photocatalysis. Two sequential 1 e^- transfers might be possible if the 1st and 2nd reduction potentials of the guest are similar, with the mono-reduced species being stabilised (e.g. by a structural rearrangement) before the second reduction takes place. Or simultaneous transfer of 2 e^- might occur, this can be done heterogeneously using semiconductors e.g. TiO_2 as an electron reservoir.[5] However, to do this homogenously, the requirement is that two chromophores must be close to the substrate at the same time and be excited simultaneously as illustrated by the example of two porphyrins donors linked by a naphthalenediimide (NDI) acceptor, which gives doubly reduced $(NDI)^{2-}$ under high laser intensities.[6] This could potentially be achieved with a cage/guest system, where there are multiple chromophores that surround a single guest.

If two electron transfer processes occur, then it would provide unprecedented examples of multi-electron, homogeneous, photocatalytic reductions that use the energy of light to build up multiple electron equivalents in the form of stable reduced species to form new types of solar fuel, arising from the use of a coordination cage as both host and multi-electron photosensitiser. Another interest would be to look at guests that might undergo a reaction after initial one-electron reduction. If the guest radical anion can undergo a reaction, and the products are more weakly bound in the cage cavity than the starting material to allow turnover, then we have the possibility for a photocatalytic cycle. Importantly, whatever reaction that occurs, needs to proceed on a timescale that is fast compared to the lifetime of the charge-separated state, or it will not be able to compete with back electron-transfer (geminate recombination), which suggests that a unimolecular reaction such as bond cleavage for the initially-generated radical anion might be a good target. We have therefore examined the guest binding properties of a range of aromatic Ar-S-S-Ar (Ar = aryl group) disulfides, with different substituents, in the cage cavity. Disulfides are known to interconvert between disulfides and thiols in a two-electron / two-proton process, this reversible process is important in a variety of chemical and biochemical situations, including the oxidation of cysteine and the vulcanization of rubber.[7–10] The general reaction scheme for this conversion is shown in equation 4.

$$RSSR + 2H^+ + 2e^- \rightarrow 2RSH \tag{4}$$

There are two different methods for the two-electron transfer. The first is in equation 5, with two electrons moving to the disulphide to generate two thiolate anions. This process generally happens in aprotic solvents and is irreversible.[4]

$$RSSR + 2e^- \rightarrow 2RS^- \tag{5}$$

Secondly, the reaction can also proceed via a three-step mechanism (eq. 6, 7) where the radical anion of the disulfide is initially formed: this can then dissociate to a radical thiol and a thiolate anion. The radical can then be reduced further *via* a second electron step, which generally occurs at a potential 0.5 V more positive than the first reduction of the disulphide.[11]

$$RSSR + e^- \leftrightharpoons RSSR^{\bullet -} \rightarrow RS^{\bullet} + RS^- \tag{6}$$

$$RS^{\bullet} + e^- \rightarrow RS^- \tag{7}$$

This mechanism is more thermodynamically and kinetically likely than the simultaneous $2e^-$ process. $RSSR^{\bullet -}$ has a unique 3-electron bond between the two sulphur atoms: $(RS\therefore SR)^-$; where two of the electrons are in a σ-bonding orbital, but the third is in the antibonding σ* orbital, and the electronic σ-σ* transition typically occurs between 380-450 nm.[12] This bond formally has a bond order of 0.5 and so is weaker than a normal 2-electron bond, so dissociates fairly easily to $RS^{\bullet} + RS^-$.

4.1.1 Aims

The aims of this work are to use the photo-active cages $[Os_4Zn_4(L^{nap})_{12}]Cl_{16}$ and $[Cd_8(L^w)_{12}](NO_3)_{16}$ as hosts for hydrophobic disulfide guests, to determine whether cage-to-guest photoinduced electron transfer processes are possible; which then might give photocatalytic cleavage of the guest disulfide, with the interesting possibility of a two-electron process being possible.

4.2 Results and Discussion

4.2.1 Binding of disulfide guests

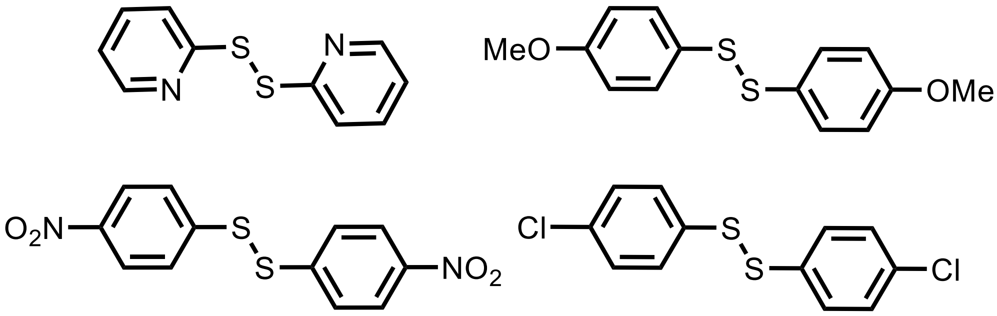

Scheme 4.2.1: Chemical structures of the 2,2’-dipyridyl disulfide (**G^{2py}**), bis(4-methoxyphenyl)disulfide (**G^{4OMe}**), 4-nitrophenyl disulfide (**G^{4NO2}**) and bis(4-chlorophenyl)disulfide (**G^{4Cl}**).

The set of disulfide guests used in this study are illustrated in scheme 4.2.1. These various aryl disulfides show different electron accepting abilities for example: the nitro group is electron withdrawing and the methoxy group is electron donating, thereby allowing a variety of situations to be studied. Some of these guests had their binding constants in the cage predicted using the GOLD molecular docking software.[13] The results of these calculations, in table 4.2.1, show that the predicted binding constants are quite high (10^4 – 10^6 M^{-1}). The algorithm takes into account a range of factors to predict guest binding, including steric clashes between cage and guest, burial of polar groups in a non-polar environment, torsional strain induced on the ligand, matching of hydrophobic surfaces and loss of ligand flexibility.[13] With this set of aryl disulfide guests, the high binding constants were shown to be mainly due to the high hydrophobicity of the guests and in the case of bis(4-methoxyphenyl)disulfide (**G^{4OMe}) -** which has a slightly lower predicted binding constant than the others – there was also a larger loss of ligand mobility compared to the other guests, as the molecule contains a larger number of rotatable bonds.

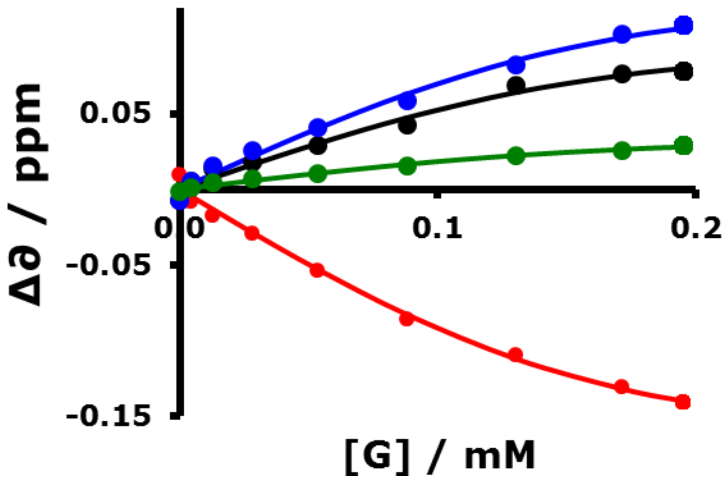

Figure 4.2.1: 1:1 binding curve of a ^{1}H NMR titration of **G^{4Cl}** into [$Co_8(L^{nap})_{12}]Cl_{16}$, fitting multiple host peak shifts at different ppm (31 ppm (blue), 66 ppm (black), 15 ppm (green), -11 ppm (red)) against [**G^{4Cl}**].

Real binding constants of guests in the cage cavity were measured using ^{1}H NMR spectroscopic titrations. As with previous work, the paramagnetic [$Co_8(L^{nap})_{12}]Cl_{16}$ cage was used to perform these titrations due to the dispersion of host peaks over a wide chemical shift range due to the cage paramagnetism. The results of this showed that all four disulfides were in fast exchange on the NMR timescale with just a steady shift in the position of some of the host cage signals observed as the titration progressed and not separate signals of free and bound cage, which would occur if free and bound guests were in slow exchange. The $\Delta\delta$ shifts for each guest were plotted against guest concentration and a binding constant was determined, assuming a 1:1 binding stoichiometry (figure 4.2.1). The titrations were repeated three times each and the binding constants were fit to shifts of more than three of the host signals.

Table 4.2.1 indicates the binding constants for each guest, which range from 10^3 – 10^4 M^{-1}, with 2,2'-dipyridyl disulfide (**G^{2py})** having the lowest value: $K = 10^3$ M^{-1}. This is due to **G^{2py}** being more hydrophilic than the other substituted disulfides because of the 2-pyridyl units, therefore it binds less strongly. The prediction of the binding constants from GOLD differs slightly to the measured results, apart from in the case of **G^{4OMe}**, which aligns well to the prediction. This suggests that maybe the binding method is slightly different to what is expected or that the software did not correctly predict the flexibility of the S-S bond.

Table 4.2.1: *Binding constants and redox potentials of substituted aryl disulfide guests.*

	K (GOLD) / M^{-1}	*K* (NMR) / M^{-1}	$E_{1/2}$ vs. SCE / V
bis(4-chlorophenyl)disulfide	2×10^6	5×10^4	-1.43 (DMF)[14]
bis(4-methoxyphenyl)disulfide	8×10^4	3×10^4	-1.71 (DMF)[14]
2,2’-dipyridyl disulfide	3×10^5	3×10^3	-0.81 (DMSO)[15]
4-nitrophenyl disulfide	-	3×10^4	-0.79 (DMF)[14], -0.60 (DMSO)[15]

To understand if binding could be observed in the solid state, measurements of crystal structures of the disulfide guests bound in the host cage was attempted. For this $\mathbf{G^{2py}}$ was used as it has a clear hydrogen bonding unit which makes it easier for the guest to be taken up into the host cage unit in ‘crystalline sponge’ experiments.[16] The work for this was performed at Diamond Light Source by Christopher Taylor, who also determined the crystal structure. Figure 4.2.2 shows the crystal structure of the cage/guest assembly where one $\mathbf{G^{2py}}$ molecule is positioned in the cavity of the cage, as well as two methanol molecules. The N and S atoms of the guest are directed into one of the *fac* tris-chelate metal vertices, as shown in the lower image in figure 4.2.2. This allows the lone pair on the N atom of $\mathbf{G^{2py}}$ to participate in a network of weak CH···N interactions (in the range of 2.59-2.98 Å), with a set of the convergent CH protons of the cage, that lie close to the metal centres. One of the S atoms of the disulfide atoms on $\mathbf{G^{2py}}$ also interacts with a CH proton of the cage with a distance of 2.82 Å. In addition to this, there are interactions of a methanol molecule with the opposite *fac* site, CH···OH, with a range of 2.52-2.90 Å.

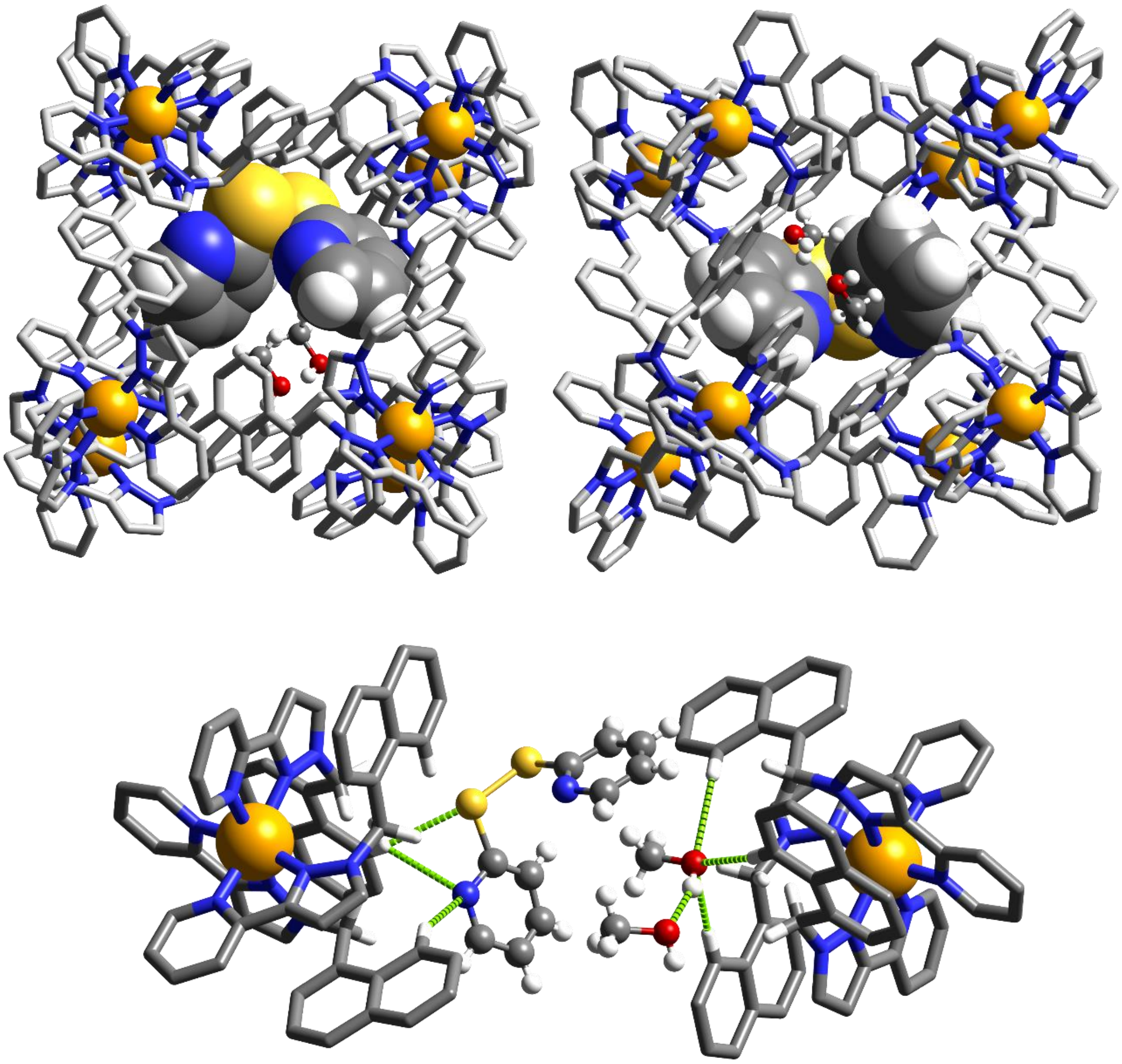

Figure 4.2.2: Three views of the crystal structure of $[Co_8(L^{nap})_{12}](BF_4)_{16}$•$\mathbf{G^{2py}}$ adduct. Top: two views of the complete cage (excluding H atoms) showing the position and orientation of the guest and 2 methanols. Lower: a view showing the guest and two MeOH molecules in between the two opposed *fac*-tris(chelate) metal complex vertices of the cage.

4.2.2 Luminescence quenching

The binding of the guests and photophysical effects on the cage upon guest binding were also examined by luminescence titrations. Initially $[Os_4Zn_4(L^{nap})_{12}]Cl_{16}$ was used as the host. If photoinduced electron transfer to the guest was occurring we would expect the addition of the disulfide guest to substantially quench the emission of the Os(II) cage's excited state.

On addition of small portions of guest during the titration, what was actually observed was an initial *increase* in emission intensity, which was then followed by a decrease in intensity (figure 4.2.3). The titrations in this work were repeated at least 2 times and gave consistent results. With 4-nitrophenyl disulfide ($\mathbf{G^{4NO2}}$) and $\mathbf{G^{2py}}$ as guests, the result of the titration was a net decrease in emission intensity by the end of the titration; with the other two guests, the intensity decrease, in the later stages of the titration, approximately returned to the initial intensity value for the free host. Notably the two guests that gave the largest quenching were those with the least negative reduction potentials of the four guests (table 4.2.1), as $\mathbf{G^{4NO2}}$ is the easiest to reduce, -0.6 V *vs.* SCE (in DMSO) and $\mathbf{G^{2py}}$ the second easiest with a reduction potential of -0.8 V *vs.* SCE (in DMSO). We would expect the most easily reduced guests to most effectively quench the cage emission by photo-induced electron transfer. It was shown earlier that the cage excited state can reduce guests whose reduction potentials are no more negative than -1.3 V (*vs*. SCE): given that the reduction potentials of bis(4-chlorophenyl)disulfide ($\mathbf{G^{4Cl}}$) and $\mathbf{G^{4OMe}}$ are -1.4 V and -1.7 V respectively we would not expect any photo-induced electron transfer quenching to occur with these two guests.

The two-stage change in emission intensity (increase and then decrease during the titration) is surprising. The initial increase suggests that during this phase the cage rigidity is being enhanced, as the reduction in vibrational flexibility is known to limit non-radiative decay pathways, thereby enhancing the observed emission intensity.[17] This implies a two-step binding process with initial binding of guest to the cage exterior surface, enhancing the emission followed by cavity binding as the guest concentration increases, reducing the emission. This would require that the exterior surface binding have a higher binding constant than the interior surface binding.

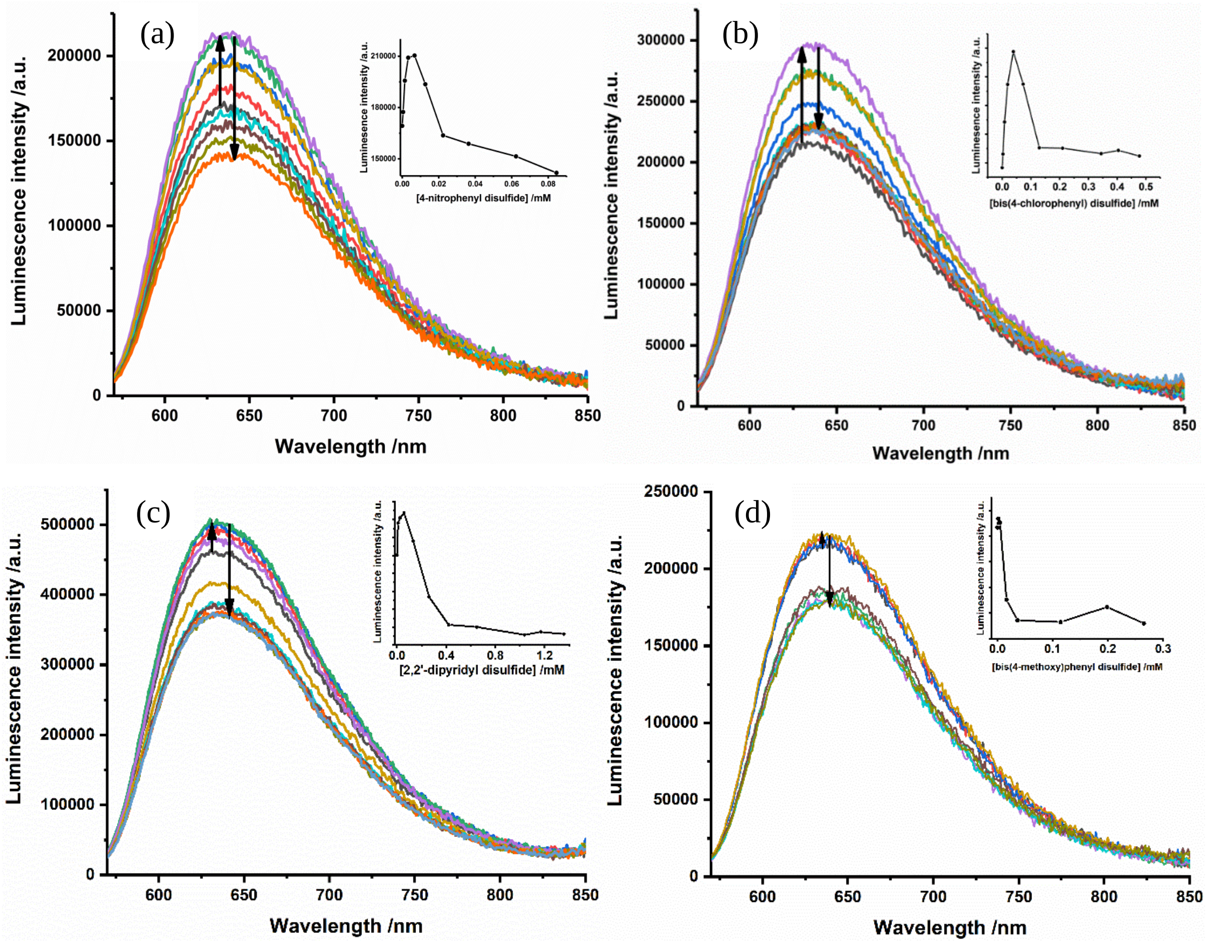

Figure 4.2.3: Luminescence titrations of guests, (a) $\mathbf{G^{4NO2}}$, (b) $\mathbf{G^{4Cl}}$, (c) $\mathbf{G^{2py}}$ and (d) $\mathbf{G^{4OMe}}$, into $[Os_4Zn_4(L^{nap})_{12}]Cl_{16}$ cage.

To study this interesting effect further, the same titration experiments were performed with the isostructural Cd(II) cage $[Cd_8(L^w)_{12}](NO_3)_{16}$, where L^w is the same molecule as L^{nap}, but additionally functionalised with -3.+CH$_2$OH groups on the pyridyl rings to enable water solubility. The cubic architectures and cavity size / shape, and hence guest binding properties, are the same between the two. Using the Cd(II) cage – which exhibits fluorescence from the naphthalene groups in the ligand – will allow us to see if this two-phase change in luminescence behaviour is the same for both types of luminescent cage and is therefore a general effect rather than being associated solely with the Os_4Zn_4 cage.

From previous work by the group, it is known that $[Cd_8(L^w)_{12}](NO_3)_{16}$ has UV/vis absorption maxima at 295 nm ($\varepsilon = 7.3 \times 10^4$ M^{-1} cm^{-1}) and 210 nm (2.4×10^5 M^{-1} cm^{-1}).[17] So to perform the fluorescence titrations, the cage was excited at 325 nm, which produced the expected naphthalene-based fluorescence band at 400 nm. The same set of guests were titrated into solutions of the Cd(II) cage as before, and the titration results are in figure 4.2.4. We see that these titrations also resulted in an initial increase in cage emission followed by a decrease to a limiting value. Again, this indicates that the initial increase in cage emission intensity could be due to interaction of the disulfide with exterior surface of the cage, rigidifying it and increasing luminescence by minimising vibrational deactivation pathways. Guest binding in the cavity with a smaller association constant then follows this phase, and causes quenching as the guest is held close to all the chromophores in the cage. The initial interaction of the guest with the exterior surface of the cage is also driven by the hydrophobic effect, in the same way as any hydrophobic species tend to aggregate in water. It is thought that this increase in rigidity is then outweighed by quenching affects from the internally bound guests, hence why the luminescence intensity decreases in the later stages of the titrations.

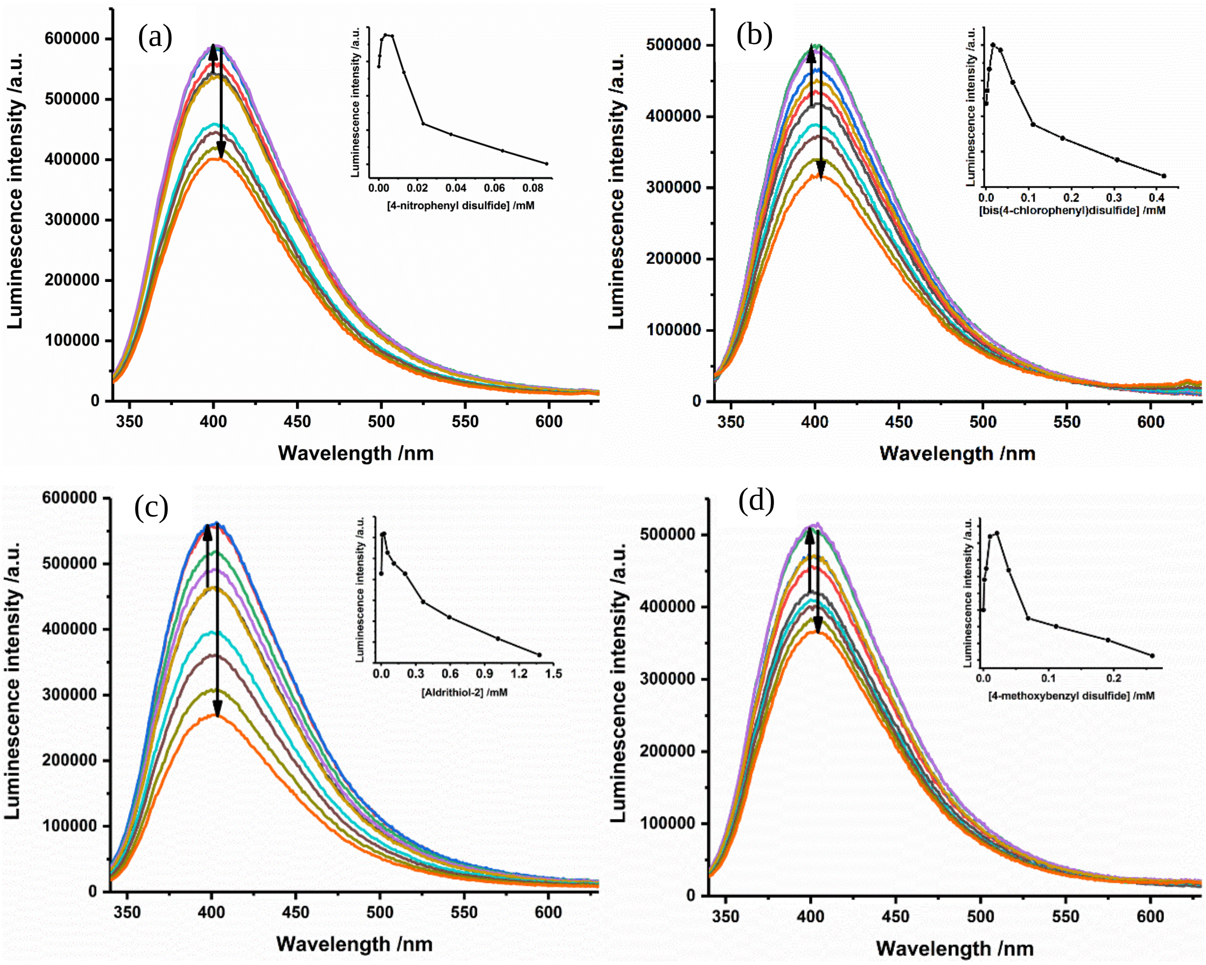

Figure 4.2.4: Luminescence titrations of guests, (a) $\mathbf{G}^{\mathbf{4NO2}}$, (b) $\mathbf{G}^{\mathbf{4Cl}}$, (c) $\mathbf{G}^{\mathbf{2py}}$ and (d) $\mathbf{G}^{\mathbf{4OMe}}$, into $[Cd_8(L^w)_{12}](NO_3)_{16}$ cage.

To compare the results from using the two different cages, the graphs in figure 4.2.5 were produced by normalising the change in intensity and plotting this against guest concentration.

The red lines relate to the titrations using $[Os_4Zn_4(L^{nap})_{12}]Cl_{16}$, and the grey lines relate to use of $[Cd_8(L^w)_{12}](NO_3)_{16}$ as the host cage. When using the Cd(II) cage we see that the emission is quenched by the end of the titration to a greater extent than when using the Os(II) cage. This makes sense as the Cd(II) cage is a better excited-state electron donor as naphthalene is known to have an oxidation potential of ~1.5 V (to give its radical cation), and the excited state energy content of this cage is measured to be 3.5 eV.[17] So from the Rehm-Weller equation, we expect the cage excited state to reduce guests whose reduction potentials are up to -2.0 eV, whereas the Os(II) cage can only reduce guests which reduce by -1.3 V.[17,18]

With regard to the titration of **Os•Zn** with **G^{4OMe}**, the results are slightly unusual with there being a very small increase in intensity followed by a decrease of nearly 20% which plateaus after 1 equivalent of guest is added. You would not expect **G^{4OMe}** to participate in electron transfer with **Os•Zn**, and so the reduction in intensity could be due to mechanical effects of **G^{4OMe}** binding in the cage rather than any photo-interaction between the two molecules. This is indicated by the intensity rapidly plateauing after 1 equivalent is added, whereas with **G^{4NO2}** the data never plateaus, suggesting if more guest were added quenching would continue. The lack of a significant rise in intensity for **G^{4OMe}** is also interesting if you relate it to the comparison of binding constants that GOLD predicted and those from NMR. These results showed that **G^{4OMe}** was the only guest that gave comparative binding constant figures, which indicates that maybe the external association of **G^{4OMe}** with the cage is less significant than with the other guests, as it more closely follows the predicted binding pattern.

When using $[Cd_8(L^w)_{12}](NO_3)_{16}$ as the cage; there is clearly a larger quenching effect with all four guests that are added to the solution, in line with the reasoning (above) that the naphthyl chromophores in this cage are a stronger electron donor. Thus, with **G^{2py}** there is a 40% reduction in intensity, with **G^{4NO2}** a nearly 30% reduction, and with **G^{4OMe}** and **G^{4Cl}** a 15% reduction. This trend follows the pattern of reduction potentials for the guests, apart from with **G^{4NO2}**, which has poor solubility so the limiting concentration was low. What is interesting, is that the Os(II) cage and the Cd(II) cage both require, with many of the guests, a similar concentration of a particular guest to reach the *maximum* luminescence intensity in the early stages of the titration. Which suggests that the binding constant of each disulfide with the cage exterior is similar in each case (i.e. it the external does not depend on the type of cage, but on the type of guest). The only exception to this is when using **G^{4OMe}**, which causes a large increase in intensity with the Cd(II) cage, which does not happen with the Os(II) cage. The reason for this is unclear and requires further work to understand.

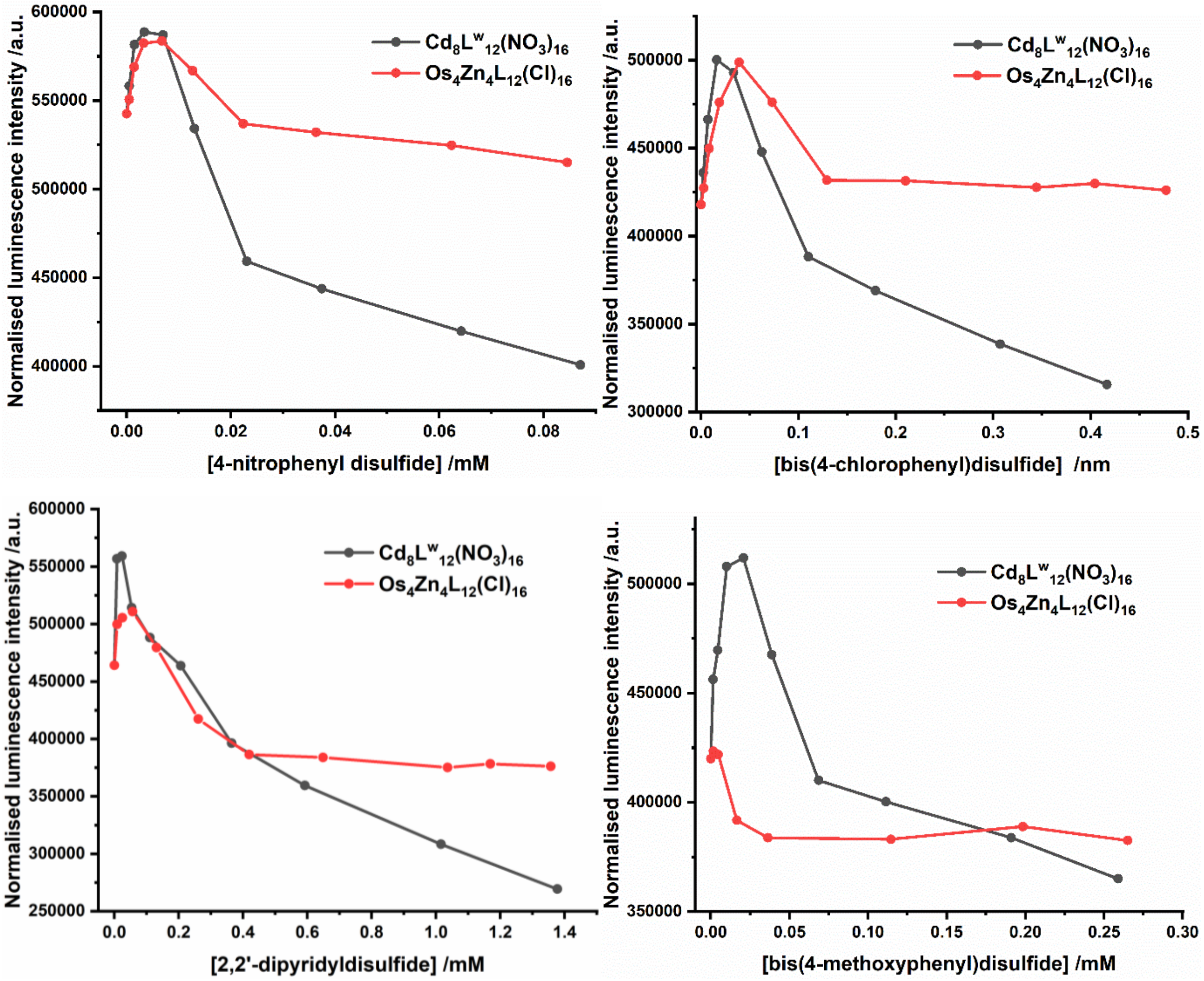

Figure 4.2.5: Comparisons of change in intensity versus guest concentration from titrations using cages, $[Cd_8(L^w)_{12}](NO_3)_{16}$ (grey line) and $[Os_4Zn_4(L^{nap})_{12}]Cl_{16}$ (red line), and the guests, clockwise from top left: $\mathbf{G^{4NO2}}$, $\mathbf{G^{4Cl}}$, $\mathbf{G^{4OMe}}$ and $\mathbf{G^{2py}}$.

To understand what type of quenching is occurring in these cage/guest systems (static or dynamic), the luminescence lifetime of the complex was measured during two of the $[Cd_8(L^w)_{12}](NO_3)_{16}$ titrations, with $\mathbf{G^{4Cl}}$ and $\mathbf{G^{4OMe}}$. The empty cage $[Cd_8(L^w)_{12}](NO_3)_{16}$ shows emission with two lifetime components of 4 ns and 10 ns.[17] The 10 ns component is expected to relate to the decay of a naphthalene singlet state and the 4 ns component is thought to be due to the exciplex-like emission arising because of the extensive π-stacking between the alternating electron-rich naphthyl units and electron-deficient pyridyl-pyrzole units of the ligands in the cage.[17,19] Therefore, when measuring the lifetimes of luminescence from the cage/guest complexes with this cage, the data was fit to two lifetime components. The Stern-Volmer plots for these titrations were based on the shorter component. Figure 4.2.6 shows the results. When the intensity is increasing, the lifetime also increases, which supports the suggestion that there is a decrease in non-radiative decay when the cage is more rigid. However, when the intensity starts to decrease the lifetime also decreases. The observed sublinear dependence of τ_0/τ *vs.* concentration of $\mathbf{G^{4OMe}}$, suggests that both dynamic and static quenching processes are occurring. However, with $\mathbf{G^{4Cl}}$, there are not enough points in the plot to determine whether τ_0/τ depends linearly on the concentration of the guest, thus the contributions of static vs dynamic quenching cannot be estimated. In chapter 2, Stern-Volmer plots with **Os•Zn** and 1,4-naphthoquinone/1,2,4,5-tetracyanobenzene showed that there is static quenching due to the bound guest, but there is also some dynamic quenching.

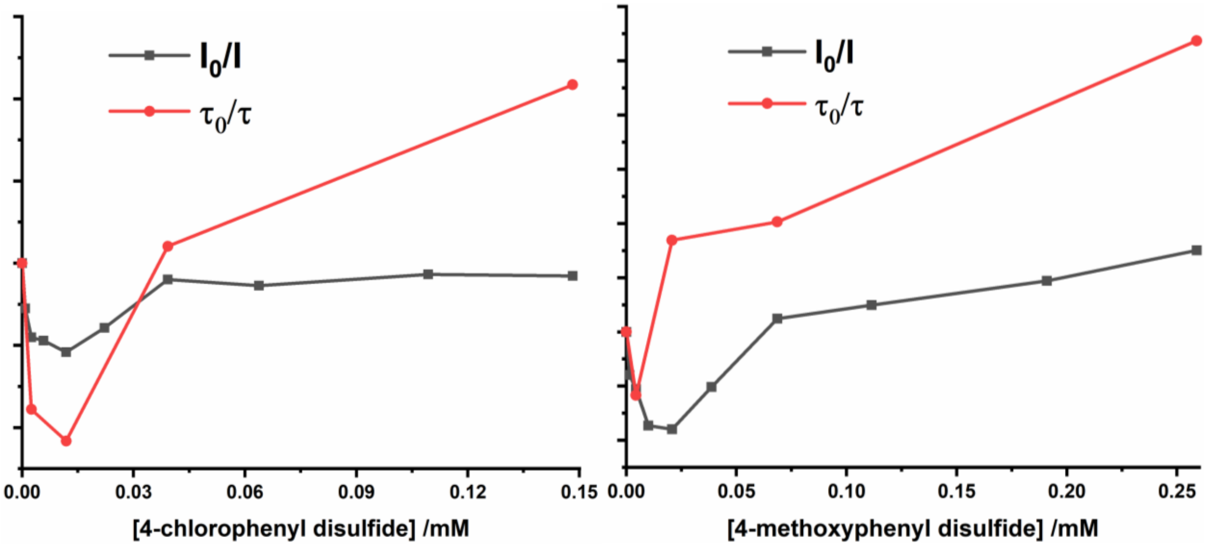

Figure 4.2.6: Stern-Volmer plot from titrations of $\mathbf{G^{4Cl}}$ (left) and $\mathbf{G^{4OMe}}$ (right) into $[Cd_8(L^w)_{12}](NO_3)_{16}$.

Another way to confirm whether the decrease in luminescence intensity during the second phase of the titrations, is related to the guest binding in the cage, is to fit the change in intensity *vs.* guest concentration to a 1:1 binding curve. The results of this analysis were fairly consistent with that of the ^{1}H NMR titrations and the comparison of the results can be seen in table 4.2.2. When performing the ^{1}H NMR titrations you don't observe the two-step binding behaviour, possibly due to the slow timescale of NMR compared to luminescence, meaning that NMR shows the ensemble average. Relating the results of both techniques give quite good consistency with the use of three different cages, with only the binding constants of $\mathbf{G^{4NO2}}$ being a lot higher from luminescence titrations compared to NMR. This could be due to the very low concentrations used, which give these binding constants a larger error than that of the more water soluble disulfides. The similarity of the calculated binding constants from the decay phase of the luminescence titrations with the results of the NMR titrations suggests that the decrease in luminescence intensity is indeed due to guest binding. In addition to this, in a couple of cases the rise of the emission intensity could be fitted to a 1:1 binding curve; for both $\mathbf{G^{4Cl}}$ and $\mathbf{G^{2py}}$ this binding constant is slightly larger than that of the decay, which is expected, as this process initially outweighs the internal binding in the luminescence titrations. Unfortunately, the rise could not be fitted in all cases due to the lack of data points of this region.

Table 4.2.2: *Comparison of the binding constants of several disulfides with three analogous cages, obtained by luminescence and ^{1}H NMR titrations.*

	K /M^{-1}		
	$[Co_8(L^{nap})_{12}]Cl_{16}$ – NMR	$[Os_4Zn_4(L^{nap})_{12}]Cl_{16}$ – luminescence	$[Cd_8(L^w)_{12}](NO_3)_{16}$ – luminescence
4-nitrophenyl disulfide	3×10^4	6×10^5	2×10^4
Bis(4-chlorophenyl)disulfide	5×10^4	6×10^4 (rise 6×10^5)	2×10^5
Bis(4-methoxyphenyl)disulfide	3×10^4	2×10^4	5×10^4
2,2’-dipyridyldisulfide	3×10^3	1×10^4 (rise 4×10^4)	2×10^3

4.2.3 Evidence for photoinduced electron transfer

To investigate further if electron transfer between the host cages and disulfide guests was taking place, UV/vis transient absorption (TA) spectroscopy was performed, which allows one to observe the dynamics of the excited state and to determine if any new charge separated states are formed. Initially, $[Cd_8(L^w)_{12}](NO_3)_{16}$ was used due to it being a stronger electron donor, and due to it undergoing electron-transfer quenching with all four disulfides. However, the TA spectra for $[Cd_8(L^w)_{12}](NO_3)_{16}$ exhibits quite unusual excited state dynamics, due to the aforementioned exciplex-like state from the π-stacked array of ligands (figure 4.2.7). This produces a TA spectrum where there are no ground state bleaches when exciting at 310 nm; instead what is observed is two broad transient states that are related to the singlet naphthyl excited state at 360 nm and a broad feature at 550 nm relating to the exciplex-like state. The decay behaviour was previously found to be bi-exponential with time constants of 32(±11) ps and 1130(±150) ps.[17] Therefore when adding the disulphide guests, due to the large component of free (unquenched) cage, there would have to be a clear strong transient absorption peak to stand out from the background intensity associated with the excited state of the empty cage. If PET occurred we would expect to observe peaks for the reduced guest $RSSR^{\bullet-}$ between 420-470 nm; or a peak for $RS^{\bullet-}$ at ~500 nm.[20,21]

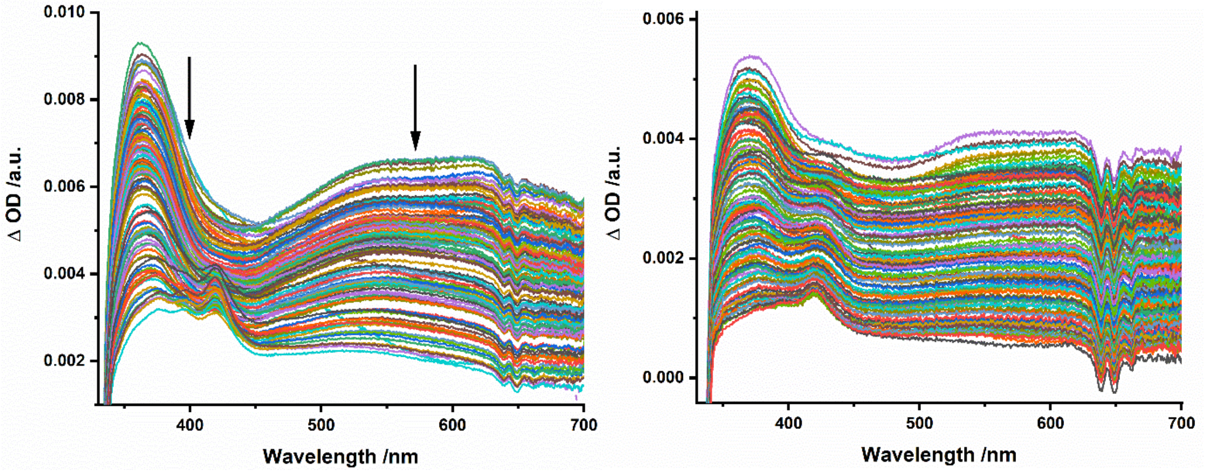

Figure 4.2.7: Transient absorption spectra, at time delays of 1 ps – 5 ns, of $[Cd_8(L^w)_{12}](NO_3)_{16}$ (left) and $[Cd_8(L^w)_{12}](NO_3)_{16}$ and $\mathbf{G^{4OMe}}$ (right).

However, as free $[Cd_8(L^w)_{12}](NO_3)_{16}$ has a large excited-state absorbance over this region, no distinctive new features, corresponding to the expected transiently reduced guests, could be discerned when viewing at the complexes of $\mathbf{G^{4OMe}}$ (figure 4.2.7), $\mathbf{G^{2py}}$ (figure 4.7.1) and $\mathbf{G^{4NO2}}$ (figure 4.7.2) with this cage. In addition to this, no subtractions of the background $[Cd_8(L^w)_{12}](NO_3)_{16}$ spectra could be performed like in the previous work with $[Os_4Zn_4(L^{nap})_{12}]Cl_{16}$, as there are no bleaches in the spectra to normalise the data to. Therefore, global analysis was undertaken to see if any new decay components could be observed corresponding to cage/guest charge-separated excited states. However, no new decay components could be distinguished as the large amount of free cage masked any new states formed. The expected absorbance peaks for photo-generated $RSSR^{\bullet-}$ or $RS^{\bullet-}$ are broad and cannot, if they are present, be differentiated from the broad $[Cd_8(L^w)_{12}](NO_3)_{16}$ excited state absorbance. Therefore, in future it is advised that when using $[Cd_8(L^w)_{12}](NO_3)_{16}$ to study electron transfer to bound guests, it would be beneficial if the guest radical anion has a sharp absorption feature that is more easily distinguishable in a TA spectrum; as well as higher guest water solubility, to enable a larger concentration of H.G complex to be formed. Another complication with $[Cd_8(L^w)_{12}](NO_3)_{16}$, is that in this example the cage is excited at 320 nm, which is also in the region where the organic guests absorb, so direct excitation of the guest confuses the issue further (figure 4.6.1) – this is the reason for the difference in appearance of figures 4.2.7, 4.6.1 and 4.6.2.

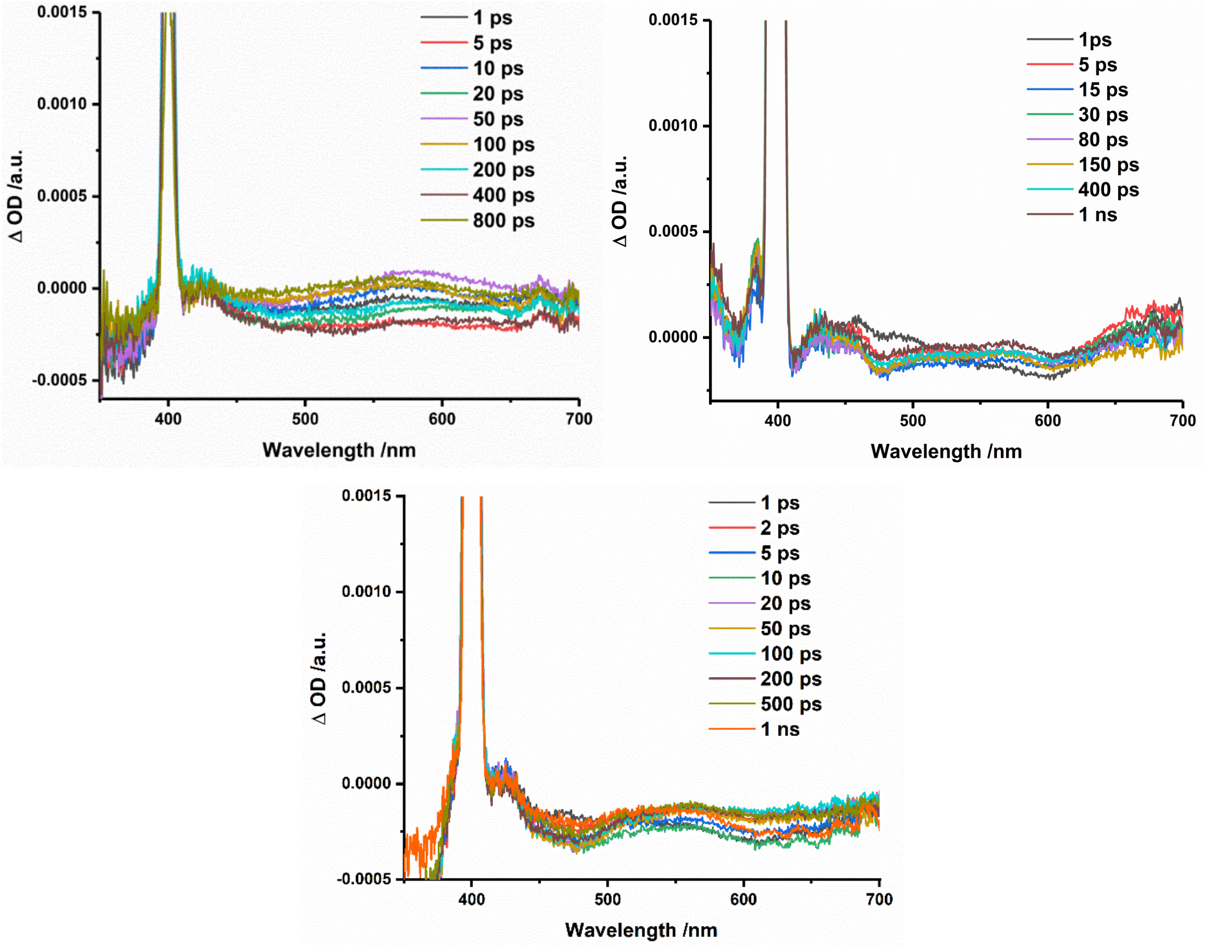

Figure 4.2.8: Subtraction of transient absorption spectra at 5 ns time delay from shorter time delays of complexes of $[Os_4Zn_4(L^{nap})_{12}]Cl_{16}$ with $\mathbf{G^{2py}}$ (left), $\mathbf{G^{4OMe}}$ (right) and $\mathbf{G^{4NO2}}$ (bottom). This should remove any long-lived transient signals from free cage and leave any new short-lived transients arising from cage-to-guest electron transfer.

UV/vis TA spectroscopy was also performed using **Os•Zn** as the host cage for the disulfide guests. The use of the Os-based cage allows for excitation in the visible region at 400 nm (into the Os-based ^{1}MLCT absorption manifold) where there is no direct excitation of the disulfide guests. Firstly, $\mathbf{G^{4NO2}}$ was looked at, as this guest is the easiest to reduce. As was shown before, with TA experiments using **Os•Zn**, there is a significant amount of free cage in the equilibrium mixture at the low concentrations of guest, therefore careful analysis of the data to subtract transient signals associated with free cage on its own was needed to reveal any new components. Figure 4.2.8 shows the results of the subtractions, using $\mathbf{G}^{\mathbf{4OMe}}$, $\mathbf{G}^{\mathbf{2py}}$ and $\mathbf{G}^{\mathbf{4NO2}}$. We would hope to see a new feature corresponding to the guest radical anion following photoinduced electron transfer between the cage and the easily reduced guests $\mathbf{G}^{\mathbf{2py}}$ and $\mathbf{G}^{\mathbf{4NO2}}$, and no feature for $\mathbf{G}^{\mathbf{4OMe}}$, as it should not be reduced by the cage-excited state; however, we could not detect any new transient signals at all. Global analysis also produced no indication of additional decay components. These results are not expected, however could be due to the small concentrations of guests used (much smaller than the previous work, 0.2 mM compared to 1.5 mM, because of the limited water solubility) or also due to the lack of quenching observed because of the exterior binding effect.

4.3 Conclusions

In summary, we have observed an interesting two-step binding profile for a set of substituted aryl disulfide guests interacting with the octanuclear cubic cages. An initial interaction of the guest with the exterior surface of the cage results in an initial increase in cage-based emission intensity; this is followed by a second binding event which partly quenches the luminescence, consistent with the guest binding inside the cage with a smaller binding constant ($K = 10^3 – 10^5\ M^{-1}$). The two most electron-deficient and easily-reduced of these guests have been shown to partly quench the emission of the Os_4Zn_4 cage; and all four guests partly quench the emission of the Cd_8 cage, in both cases suggesting the occurrence of photoinduced electron transfer. However, the charge-separated states that we would expect to see could not be observed *via* TA spectroscopy. Probably because the poor solubility of these guests in water meant that, the concentration of bound cage/guest complex in the equilibrium mixtures was low.

A few suggestions for future work, directly related to the use of disulfide molecules as guests, could be to use mixed-solvent systems to increase the solubility of the guests to allow for higher concentrations of guests to be used. There has already been some work carried out by the group into the use of mixed-solvents including H_2O/acetonitrile, H_2O/methanol and H_2O/DMSO. Another suggestion is to perform the work in a degassed environment, so that oxygen does not affect any longer timescale processes that might occur in the dissociation/reduction process, and to test the effects with and without oxygen.

Alternatively, to study the potential of two-electron transfer processes, different guests could be used that do not show such complicated binding within the cages. Quinone-type guests e.g. tetrachlorobenzoquinone and naphthoquinone could be appropriate substrates to explore 2 e^- reduction, via two successive 1 e^- reductions which are both at potentials sufficiently positive to be easily effected by PET from the Os(II) units. With a reaction of: $Q \rightarrow SQ^{\bullet -} \rightarrow (\text{catecholate})^{2-}$. 1,4-naphthoquinone has been used in this work (chapter 3) already and showed single photo-induced electron transfer; this guest could then be used to study the effect of power level on the electron transfer process as it is already known to bind in the cage and participate in photo-interactions. Increasing the power inputted into the system is known to increase the chance of 2-electron transfer.[6] Another possibility could be to look at photo-catalysed reactions like nitrobenzene to aniline, or phenyl boronic acid to phenol. Trial work on this has already been started with the interest that photocatalytic reactions on bound guests will be faster than those when the substrate is free in solution.

4.4 Experimental

4.4.1 Experimental techniques

NMR titration

$[Co_8L_{12}](Cl)_{16}$ was prepared according to previously published methods.[22] A stock host solution of $[Co_8L_{12}](Cl)_{16}$ (0.15 mM) in D_2O was used and the guests (0.15 - 0.80 mM) were dissolved in 2.5 ml of the host solution and gradually titrated into the host solution. The changes in chemical shift were plotted and fitted to a 1:1 host:guest binding model. The NMR data was processed using Bruker Topspin 4.0.3 and was fitted to binding isotherms using 14allMaster.xls, which is a macro-based Excel fitting program written by Christopher A. Hunter (University of Cambridge).

Luminescence titrations

Luminescence titrations were performed by preparing a stock solution of $[Os_4Zn_4L_{12}](Cl)_{16}$ (0.025 mM) or $[Cd_8(L^w)_{12}](NO_3)_{16}$ (0.100 mM) in deionised water. Guest solutions (0.10 – 1.5 mM) were made up using stock host solution (5 ml) and added in small portions to the quartz cuvette containing the host solution, with a luminescence spectrum measured after each addition. Luminescence spectra were recorded on a Horiba Jobin Yvon Fluoromax 4 spectrophotometer, with excitation at 550 nm and an emission window of 570 – 850 nm for $[Os_4Zn_4L_{12}](Cl)_{16}$ and excitation at 325 nm, with a measurement window of 340 – 630 nm for $[Cd_8(L^w)_{12}](NO_3)_{16}$. Changes in luminescence intensity with added guest concentration were fitted to a 1:1 host:guest binding model.

Transient Absorption Spectroscopy

The ultrafast transient absorption setup used consists of a commercial detection instrument (Helios, Ultrafast Systems) and the following laser system: a Ti:Sapphire regenerative amplifier (Spitfire ACE PA-40, Spectra-Physics) providing 800 nm pulses (40 fs fwhm, 10 kHz, 1.2mJ). Sample excitation at 400 nm was provided by doubling a portion of the 800 nm output, in a β-barium borate crystal within a commercially available doubler/tripler (TimePlate, Photop Technologies), yielding 400 nm pulses or 320 nm pulses were generated by a travelling-wave optical parametric amplifier of superfluorescence (TOPAS prime, Light Conversion) pumped by the 800 nm output. The pump pulses were focussed onto the sample cell, to a spot diameter of ≤ 0.3 mm and the pump pulse energy (3 mW) was controlled using a variable attenuation neutral-density filter wheel and the sample solution was stirred using a magnetic stirrer bar.

White light supercontinuum probe pulses were generated *in situ* using a portion of the Ti:Sapphire amplifier output, focused onto a CaF_2 crystal, allowing for the generation of light spanning 340 nm – 720 nm. Prior to generation of the white light, the 800 nm pulses were passed through a computer controlled optical delay line (DDS300, ThorLabs), which provides 8 ns of delay, with a temporal resolution of 1.67 fs. Detection was performed with a CMOS sensor for UV/Vis spectra. The pump and probe polarisations were set to a magic angle geometry. The data processing was performed using Origin 2017 and Glotaran 1.5.1.[23]

Samples were all in distilled water, with $[Os_4Zn_4(L^{nap})_{12}]Cl_{16}$ (0.15 mM) or $[Cd_8(L^{w})_{12}](NO_3)_{16}$ (0.15 mM), and guests (0.2 – 0.6 mM). Samples containing $[Os_4Zn_4(L^{nap})_{12}]Cl_{16}$ were excited at 400 nm and samples containing $[Cd_8(L^{w})_{12}](NO_3)_{16}$ were pumped at 320 nm. Guests were also excited separately at 320 nm.

Lifetime measurements

Luminescence lifetimes were measured in air-equilibrated H_2O solutions by the time-correlated single-photon counting method, using an Edinburgh Instruments 'Mini-τ' instrument using a 405 nm, ~70 ps pulsed diode laser excitation source, and with the decay data fitted using the supplied software.

X-ray crystallography

The $[Co_8(L^{nap})_{12}](BF_4)_{16}$•2,2'-dypridyl disulfide diffraction data was collected and refined by Christopher Taylor (University of Warwick). The data was collected at the UK Diamond Light Source Synchrotron facility (proposal MT19876). The structure determination suffered from the usual weak scattering characteristic of crystals of this type, associated with large unit cells and disorder of solvents/anions. The X-ray diffraction limit of the crystal was set at 0.69 Å resolution (SHEL 999). Large solvent-accessible voids containing diffuse electron density that could not be satisfactorily modelled were accounted for using the SQUEEZE command in PLATON. Full details of the refinement and treatment of this structure, including software used, are given in the CIF.

4.4.2 Synthetic procedures

Materials

$[Os_4Zn_4(L^{nap})_{12}]Cl_{16}$, $[Co_8L_{12}](Cl)_{16}$ and $[Cd_8(L^{w})_{12}](NO_3)_{16}$ were all prepared according to previously published methods.[24–26] Single crystals of $[Co_8(L^{nap})_{12})](BF_4)_{16}$ used for determination of the structure of the $[Co_8(L^{nap})_{12})](BF_4)_{16}$•2,2’-dipyridyl disulfide adduct were also prepared as described previously.[27] All other reagents were purchased from Sigma-Aldrich or Alfa-Aesar and used as received.

4.5 References

1 L. D. Zusman and D. N. Beratan, *J. Chem. Phys.*, 1996, **105**, 165.

2 J. R. Brocklehurst, *Phys. Bull.*, 1980, **31**, 54.

3 J. Lin, D. Balamurugan, P. Zhang, S. S. Skourtis and D. N. Beratan, *J. Phys. Chem. B*, 2015, **119**, 7589–7597.

4 S. Antonello, R. Benassi, G. Gavioli, F. Taddei and F. Maran, *J. Am. Chem. Soc.*, 2002, **124**, 7529–7538.

5 Y. Xu, T. Liu, H. Yin, T. Yao, X. Wang, H. Han and C. Li, *J. Photochem. Photobiol. A Chem.*, 2018, **355**, 332–337.

6 M. P. O'Neil, M. P. Niemczyk, W. A. Svec, D. Gosztola, G. L. Gaines III and M. R. Wasielewski, *Science (80-.).*, 1992, **257**, 63–65.

7 W. J. Wedemeyer, E. Welker, M. Narayan and H. A. Scheraga, *Biochemistry*, 2000, **39**, 4207–4216.

8 D. Ritz and J. Beckwith, *Annu. Rev. Microbiol.*, 2001, **55**, 21–48.

9 S. Oae, *Organic Sulfur Chemistry: Structure and Mechanism*, CRC Press, Boca Raton, 1st edn., 1991.

10 W. Hofmann, *Vulcanization and vulcanizing agents*, Palmerton, London, 1967.

11 A. Houmam, E. M. Hamed and I. W. J. Still, *J. Am. Chem. Soc.*, 2003, **125**, 7258–7265.

12 K. D. Asmus, *Methods Enzymol.*, 1990, **186**, 168–180.

13 W. Cullen, S. Turega, C. A. Hunter and M. D. Ward, *Chem. Sci.*, 2015, **6**, 2790–2794.

14 S. Antonello, K. Daasbjerg, H. Jensen, F. Taddei and F. Maran, *J. Am. Chem. Soc.*, 2003, **125**, 14905–14916.

15 I. A. Topol, C. McGrath, E. Chertova, C. Dasenbrock, W. R. Lacourse, M. A. Eissenstat, S. K. Burt, L. E. Henderson and J. R. Casas-Finet, *Protein Sci.*, 2008, **10**, 1434–1445.

16 W. Cullen, M. C. Misuraca, C. A. Hunter, N. H. Williams and M. D. Ward, *Nat Chem.*, 2016, **8**, 1–6.

17 J. R. Piper, L. Cletheroe, C. G. P. Taylor, A. J. Metherell, J. A. Weinstein, I. V. Sazanovich and M. D. Ward, *Chem. Commun.*, 2017, **53**, 408–411.

18 E. S. Pysh and N. C. Yang, *J. Am. Chem. Soc.*, 1963, **85**, 2124–2130.

19 P. D. Frischmann, V. Kunz and F. Würthner, *Angew. Chemie - Int. Ed.*, 2015, **54**, 7285–7289.

20 G. Caspari and A. Granzow, *J. Phys. Chem.*, 1970, **74**, 836–839.

21 T. Shida, *J. Phys. Chem.*, 1968, **72**, 2597–2601.

22 W. Cullen, S. Turega, C. A. Hunter and M. D. Ward, *Chem. Sci.*, 2015, **6**, 2790–2794.

23 J. J. Snellenburg, S. P. Laptenok, R. Seger, K. M. Mullen and I. H. M. van Stokkum, *J. Stat. Softw.*, 2012, **49**, 1.

24 J. S. Train, A. B. Wragg, A. J. Auty, A. J. Metherell, D. Chekulaev, C. G. P. Taylor, S. P. Argent, J. A. Weinstein and M. D. Ward, *Inorg. Chem.*, 2019, **58**, 2386–2396.

25 M. Whitehead, S. Turega, A. Stephenson, C. A. Hunter and M. D. Ward, *Chem. Sci.*, 2013, **4**, 2744–2751.

26 C. G. P. Taylor, J. R. Piper and M. D. Ward, *Chem. Commun.*, 2016, **52**, 6199–6338.

27 S. Turega, W. Cullen, M. Whitehead, C. A. Hunter and M. D. Ward, *J. Am. Chem. Soc.*, 2014, **136**, 8475–8483.

4.6 Appendix

Table 4.6.1: *Crystal data and structure refinement for* $[Co_8(L^{nap})_{12}](BF_4)_{12}$*•2,2'-dipyridyl disulfide.*

Identification code	DMWMSv3-130_F56_PydiSulph_sq
Empirical formula	$C_{378.65}H_{417.32}B_{16}Co_8F_{64}N_{73.08}O_{37.25}S_{1.08}$
Formula weight	8483.10
Temperature/K	100(1)
Crystal system	monoclinic
Space group	C2/c
a/Å	32.81236(7)
b/Å	30.21497(6)
c/Å	40.09564(8)
α/°	90.0
β/°	96.33120(19)
γ/°	90.0
Volume/Å^3	39509.35(10)
Z	4
ρ_{calc}g/cm^3	1.426
μ/mm^{-1}	0.410
F(000)	17552.0
Crystal size/mm^3	0.1 × 0.1 × 0.1
Radiation	Synchrotron (λ = 0.6889)
2Θ range for data collection/°	1.982 to 59.894
Index ranges	$-47 \leq h \leq 47$, $-43 \leq k \leq 43$, $-58 \leq l \leq 58$
Reflections collected	348244
Independent reflections	62856 [R_{int} = 0.0629, R_{sigma} = 0.0602]
Data/restraints/parameters	62856/6404/2425
Goodness-of-fit on F^2	1.106
Final R indexes [I>=2σ (I)]	R_1 = 0.0675, wR_2 = 0.2193
Final R indexes [all data]	R_1 = 0.0929, wR_2 = 0.2383
Largest diff. peak/hole / e Å^{-3}	1.42/-0.97

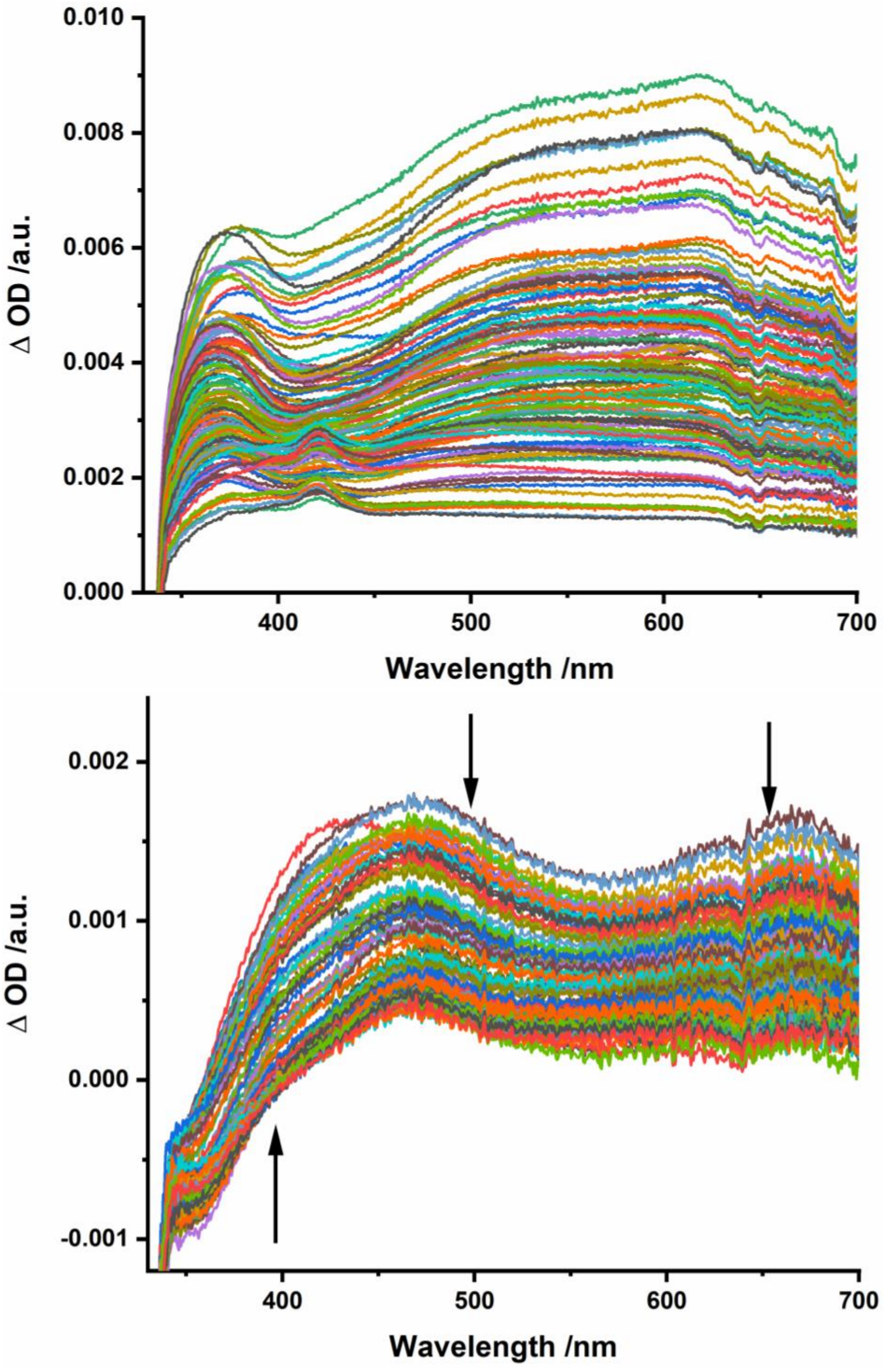

Figure 4.6.1: Transient absorption spectra at time delays from 1 ps – 5 ns, of $[Cd_8(L^w)_{12}](NO_3)_{16}$ and **G**$^{\mathbf{2py}}$ (top) and aqueous **G**$^{\mathbf{2py}}$ (bottom), exciting at 320 nm.

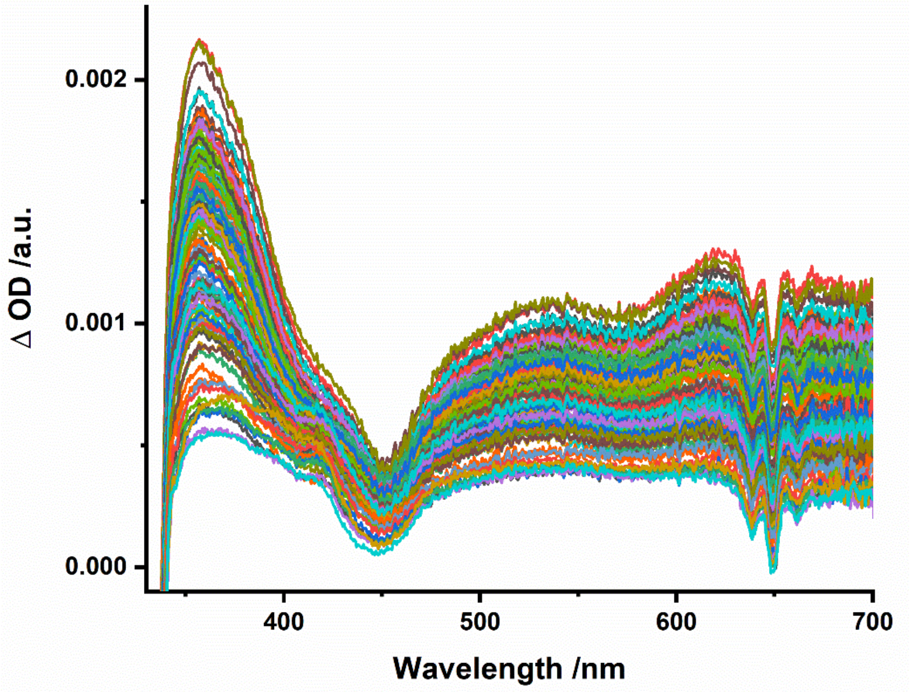

Figure 4.6.2: Transient absorption spectra at time delays of 1 ps – 5 ns, of $[Cd_8(L^w)_{12}](NO_3)_{16}$ and $\mathbf{G^{4NO2}}$.

Chapter 5

Cage Catalysis of the Kemp Elimination, Monitored by UV/vis Spectroscopy

5.1 Introduction

5.1.1 Catalysis in cages

Similarly to some enzymes, cages provide specific hydrophobic cavities to bind substrates and catalyse reactions on bound guests through a range of mechanisms, which include different noncovalent interactions.[1] The properties of cages – in particular the internal microenvironments associated with their cavities that are different from the properties of bulk solution – has meant that cages can be very effective catalysts. Showing, in some cases, substantial acceleration of the reaction rates for bound guests, enhanced reactivity and selectivity in the reactions, and changes to the reaction mechanisms and product distributions.[2,3] Catalysis can arise for many reasons including an increase in effective local concentrations of species when two species are co-located in a confined space; separation of guests from solvents or other reagents; control of the conformation of the bound guest; and shifting the equilibrium position of a reaction.[2]

Substantial increases in rates of catalysed reactions, compared to uncatalysed reactions, are possible. Two prominent examples of this have been demonstrated in different reactions by the Raymond group and the Ward group, with rate accelerations in the range 10^5 – 10^7 fold, which is similar to the rate acceleration achievable by some enzymes.[4,5]

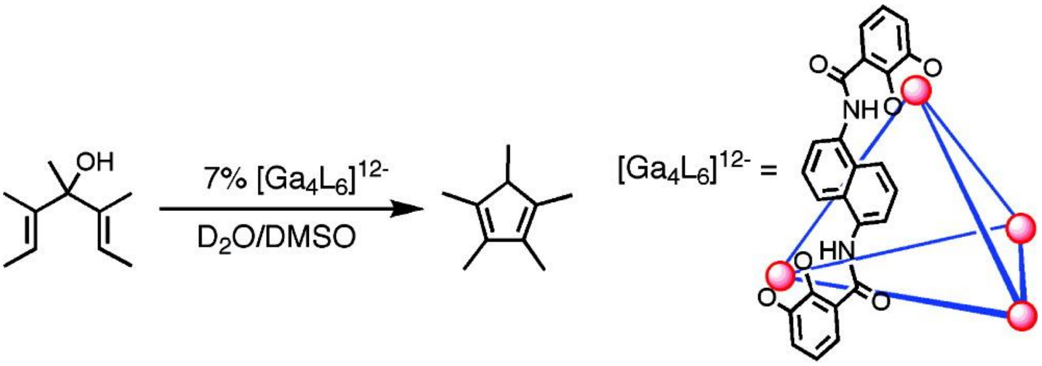

Scheme 5.1.1: Nazarov cyclisation reaction catalysed by $[Ga_4L_6]^{12-}$. (Reprinted with permission from ref. 4. Copyright 2010 American Chemical Society.)

The Raymond group demonstrated the catalysed Nazarov cyclisation of 1,4-pentadien-3-ols, using a tetrahedral Ga(III)-based cage (scheme 5.1.1).[4] The rate enhancement is up to 2.1×10^6 higher than that of the uncatalysed reaction. Through further mechanistic studies of both the uncatalysed and catalysed reactions, it was proven that this rate acceleration was largely due to the stabilisation of the transition state inside the cage, as well as the enhanced basicity of the hydroxyl group on the pentadienol caused by encapsulation.[6] This enhanced basicity occurs, as the Raymond cage is 12^- charge, so when guests are bound inside, they attract protons more easily, as the protons are enticed by the high negative charge of the host.

The Ward group's example catalyses the Kemp elimination of 1,2-benzisoxazole using a cubic $[Co_8(L^w)_{12}](BF_4)_{16}$ cage (figure 5.1.1).[5] The Kemp elimination has been widely studied, as it can be adapted to a large range of reaction rates and acts as a sensitive probe for biological and artificial catalytic systems.[7–10] The mechanism of rate acceleration, in this case, was found to be due to the aggregation of ^-OH groups around the cage (that has a 16+ charge), which therefore increased the effective concentration of ^-OH around the guest, when it was bound in the cage, thus rapidly increasing the rate of reaction.[5]

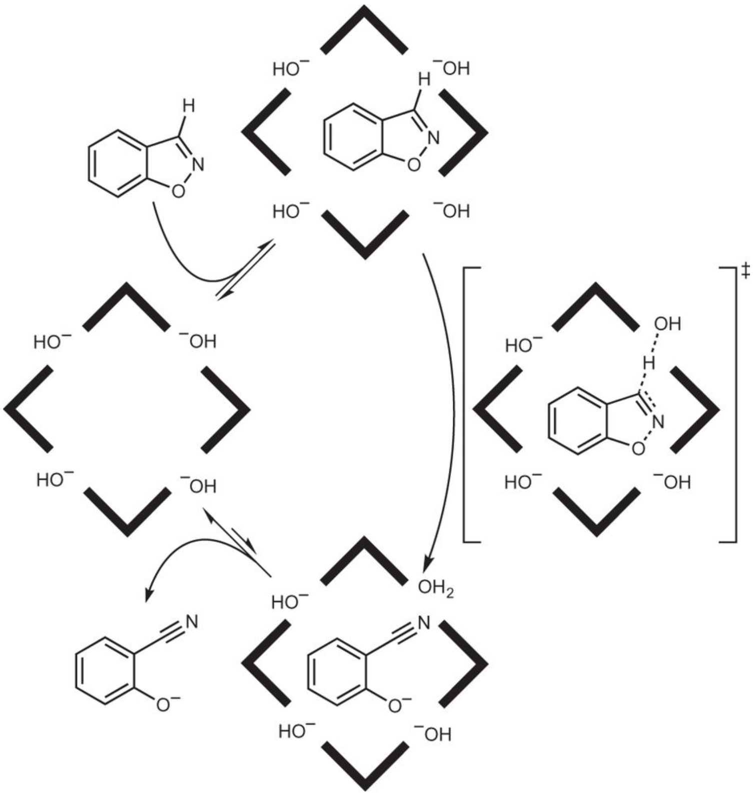

Figure 5.1.1: Mechanism of the Kemp elimination catalysed by $[Co_8(L^w)_{12}](BF_4)_{16}$. (Reprinted with permission from ref. 5. Copyright 2016 Springer Nature.)

5.1.2 Effects of charge on cage catalysis

Another interesting consequence of cage-based catalysis is that it can depend on the charge on the cage. The previous two examples of cage-based catalysis rely on the charge of the cage to accumulate counter-ions, which participate in the catalytic reaction. It follows that if the charge of a host cage can be varied, the catalysis should also be affected. The most notable example of this so far has also been by the Raymond group, where two analogous M_4L_6 cages were synthesised, which have charges of 12^{-} and 8^{-} (figure 5.1.2a). The work uses the previously mentioned $[\mathrm{Ga}^{\mathrm{III}}{}_4L_6]^{12-}$ cage and a new $[\mathrm{Si}^{\mathrm{IV}}{}_4L_6]^{8-}$ cage, where all that differs between the isostructural complexes is the nature of the metal and hence the charge.[11] When performing an Aza-Cope rearrangement (figure 5.1.2b), which had been formerly shown to be catalysed in the Ga(III) cage with an 850-fold rate enhancement,[12] the catalysis in the two cages was comparable and was found to be driven by steric effects (*i.e.* constrictive binding, the folding up of the substrate to fit inside the cavity).[2] However when performing the Nazarov cyclisation, there was a 680-fold difference in rates of catalysis between the two cages, with the more highly charged Ga(III) cage showing higher rates of catalysis. This is thought to be due to the Nazarov cyclisation requiring a protonation of the substrate and thus the generated carbocation, being more highly stabilised by the 12^{-} charged cage (figure 5.1.2).[11]

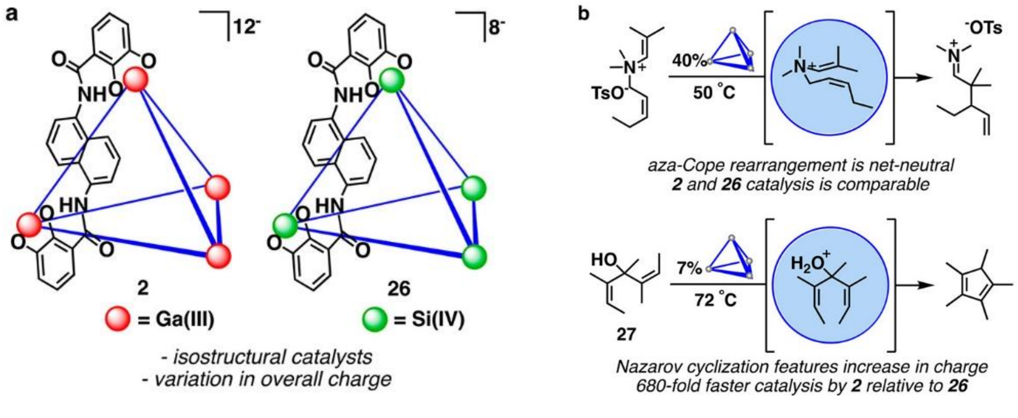

Figure 5.1.2: (a) Structures of $[\mathrm{Ga(III)}_4L_6]^{12-}$ and $[\mathrm{Si(IV)}_4L_6]^{8-}$ cages. (b) Aza-Cope rearrangement and Nazarov cyclisation reactions. (Reprinted with permission from ref. 2. Copyright 2018 American Chemical Society.)

5.1.3 Aims

The aims of the work in this chapter are:

(i) To provide a facile way to monitor the Kemp elimination reaction catalysed in our cubic coordination cage, by UV/Vis spectroscopy, rather than by NMR. This would be based on the use of 5-nitrobenzisoxazole as a substrate rather than 1,2-benzisoxazole, as the 2-cyano-4-nitrophenolate product that accumulates is coloured. This would make monitoring the reaction much quicker and easier, with the possibility to measure multiple sets of conditions in a single experiment using a UV/Vis plate reader.

(ii) Secondly, to determine whether the Os(II)/Os(III) redox swing in $[Os_4Zn_4(L^{nap})_{12}]Cl_{16}$ – which would change the charge on the cage form 16^+ to 20^+ – can have an effect on the rate of the cage-based catalysed reactions by modulating the accumulation of hydroxide ions around the cage surface as the charge changes.

5.2 Results and Discussion

For this work, we have used 5-nitrobenzisoxazole as the substrate for the Kemp elimination. The first step is the synthesis of this using a previously published method, whereby 1,2-benzisoxazole undergoes nitration using H_2SO_4/HNO_3 and is recrystallized in ethanol.[13] Once this was synthesised, tests were needed to determine whether 5-nitrobenzisoxazole would bind within the cage cavity. As ^{1}H NMR titrations using $[Co_8(L^{nap})_{12}]Cl_{16}$ showed good consistent results with data obtained in parallel from luminescence titrations in previous work, this method was again used to determine the strength of binding with this guest. Figure 5.2.1 shows the results of the ^{1}H NMR titration, where the guest is shown to be in fast exchange as there is a shift of host peaks as more guest is added. The titration was performed in similar conditions to previous work, except that the titration was carried out at pH ~ 4 to prevent the base-catalysed elimination reaction from occurring during the titration. This change in chemical shift of host signals with concentration of added guest produced a binding curve, which could be fitted to a 1:1 model. The binding constant derived from this was determined to be $K = 2 \times 10^4$ M^{-1}. This is higher than that previously found for 1,2-benzisoxazole in the same cage ($K = 4 \times 10^3$ M^{-1}).[5] This may be due to the lower water solubility (greater hydrophobicity) afforded to the 5-nitrobenzisoxazole guest, by the presence of the nitro substituent, which will increase its affinity for the hydrophobic cage cavity. This effect (stronger binding afforded by the presence of nitro groups) has been seen when using other nitrated guests too. A negative effect of this is that the guest can only be used at lower concentrations because of its limited solubility.

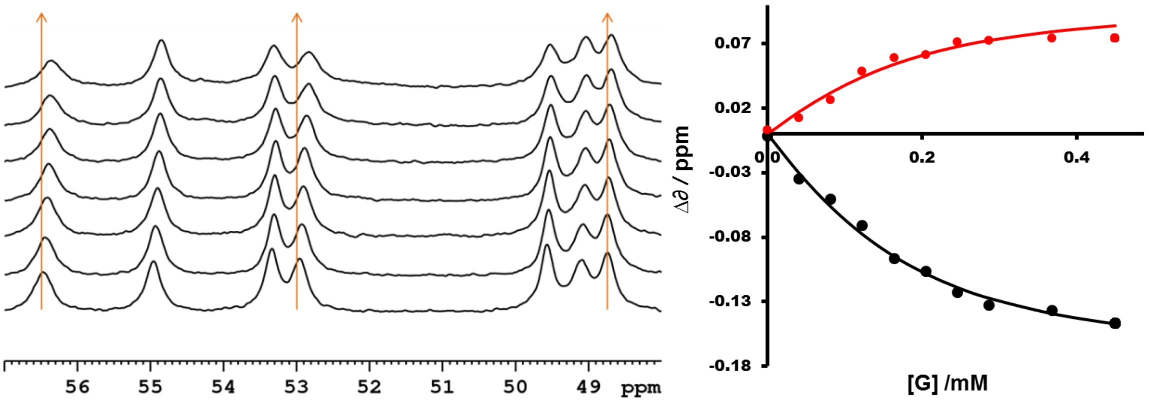

Figure 5.2.1: ^{1}H NMR titration of 5-nitrobenzisoxazole in $[Co_8(L^{nap})_{12}]Cl_{16}$ and the associated 1:1 binding curve.

In addition to the ^{1}H NMR titration, an X-ray crystal structure was obtained by Christopher Taylor (Univ. of Warwick) of 5-nitrobenzisoxazole bound in $[Co_8(L^{nap})_{12}](BF_4)_{16}$ (figure

5.2.2). The figures shows that there is a stacked pair of two 5-nitrobenzisoxazole guests. These guest molecules are orientated so that the electron-rich nitro-groups from the guests are directed into the two opposing *fac*-pockets of the cage. The C-H protons associated with this *fac* tris-chelate Co(II) centre are hydrogen-bond donors and the dotted lines in the figure shows the H···O interactions (2.50 – 2.98 Å) of N-O with the cage protons.

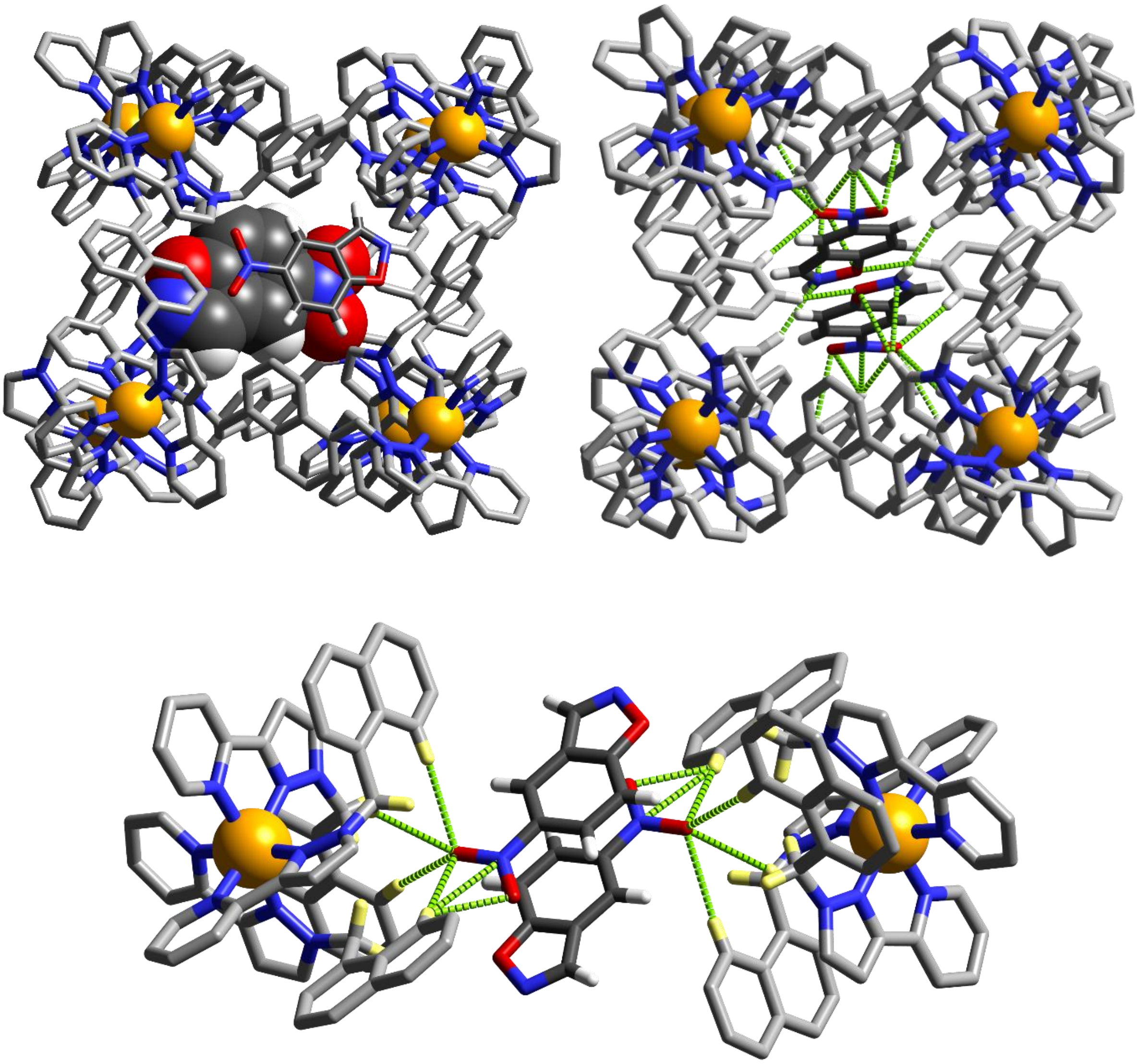

Figure 5.2.2: Three views of the crystal structure of $[Co_8(L^{nap})_{12}](BF_4)_{16}$•2(5-nitro-1,2-benzisoxazole) adduct. Top: two views of the compete cage (excluding H atoms) (left: one space-filling guest and one stick guest, right: showing the hydrogen-bond connections). Lower: a view of the two guests between the opposed *fac*-tris(chelate) metal complex vertices of the cage.

5.2.1 Uncatalysed reaction

Now that it has been shown that 5-nitrobenzisoxazole can bind in the cage, the Kemp elimination reaction needs to be studied. The reaction proceeds *via* the mechanism shown in scheme 5.2.1. It is a base-catalysed E2 elimination under basic conditions, and gives rise to the 2-cyano-4-nitrophenolate anion. The nitro group stabilises the negative charge on the oxygen and the charge-transfer nature of the π-π* transition makes this anion strongly coloured.

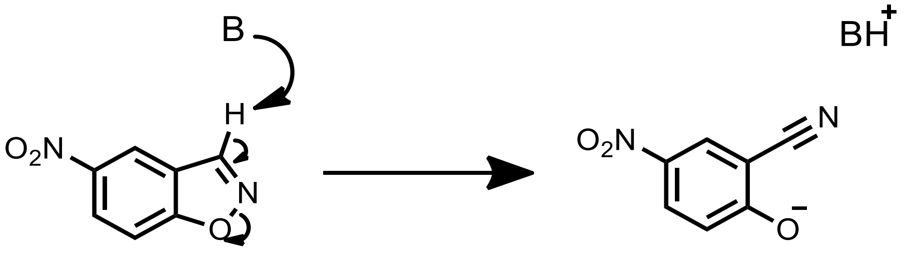

Scheme 5.2.1: Kemp elimination reaction of 5-nitrobenzisoxazole.

With 1,2-benzisoxazole as substrate for this reaction, the 2-cyanophenolate product has its absorption maximum at 325 nm – this cannot be observed conveniently by UV/Vis spectroscopy as it is obscured by the strong absorption of the host cage. However the addition of the nitro group red-shifts the maximum phenolate absorption to 380 nm, and the extinction coefficient also increases from 5980 $M^{-1}cm^{-1}$ (325 nm) compared to 15800 $M^{-1}cm^{-1}$ (380 nm).[10] This shift allows for easier analysis when performing UV/vis spectroscopy, as it moves the peak away from the high intensity UV region, to the generally lower intensity visible region where it can be conveniently monitored as it grows in during the reaction.

When monitoring the background elimination reaction in basic water, there is a clear difference between the starting material and product. The graph in figure 5.2.3 shows that as the peak at 280 nm of 5-nitrobenzisoxazole falls, the product peak from 2-cyano-4-nitrophenolate grows in at 380 nm.

This background reaction was performed at pH 9.2 with a borax buffer, which is known to be stable with the cage complex.[5] As this is a base catalysed reaction, pH has a large effect, so the rates of reaction were determined at various basic conditions. For this work, pH 8, 9 and 10 were used, as they are all within the limit of stability of the cage and give a spread of pH values large enough to show the differences between catalysed and uncatalysed reactions.

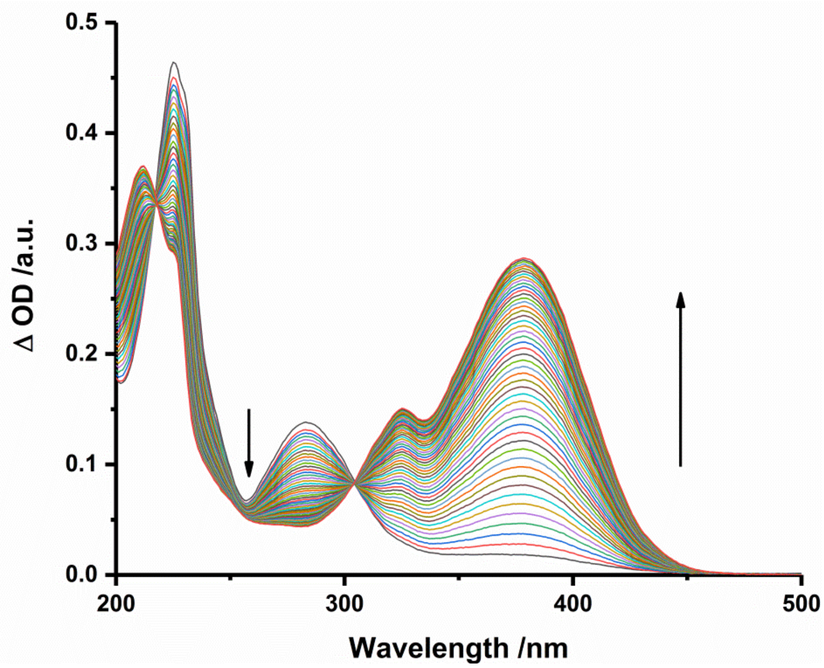

Figure 5.2.3: UV/vis spectra of uncatalysed reaction of 5-nitrobenzisoxazole with hydroxide at pH 9.2.

The reaction is first order in OH^- under basic conditions and figure 5.2.4 shows how the product appears over time at the three different pH values. The observed rates increase in a linear relationship of pH versus $\log(k_{obs})$ as expected, with the rate at pH 10 being much faster than that observed at pH 8. Another interesting observation is that these rates are a lot faster than for 1,2-benzisoxazole, with the reaction of unsubstituted benzisoaxole at pH 10.2 having a $\log(k_{obs})$ = -5.1 compared to the value here of -3.4 for 5-nitro-benzisoxazole. This is in agreement with initial work by Kemp in 1973, which showed that the elimination reaction with 5-nitrobenzisoxazole occurred much faster than the reaction of unsubstituted 1,2-benzisoxazole, where $k_{OH-} = 15\ M^{-1}\ s^{-1}$ compared to $k_{OH-} = 0.33\ M^{-1}\ s^{-1}$, respectively.[10] In his work, the associated pK_a values of the relevant cyanophenolate products were also determined, which are 4.1 for 2-cyano-4-nitrophenolate and 6.9 for 2-cyanophenolate.[10] This lower pK_a value of 2-cyano-4-nitrophenolate shows that it is effectively a better leaving group, therefore making the reaction proceed faster.

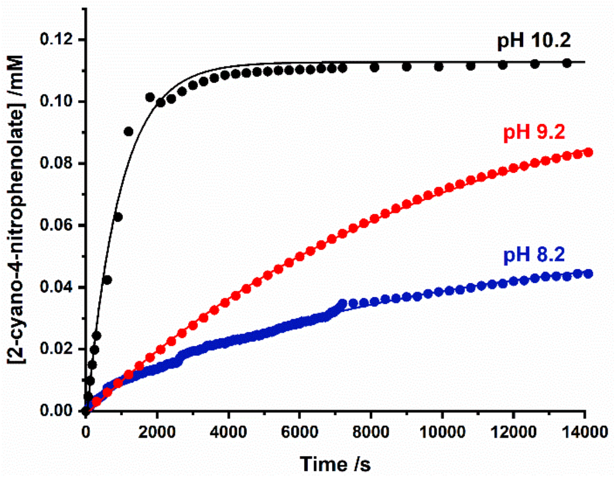

pH	$\log(k_{obs})$
8.2	-4.5
9.2	-4.1
10.2	-3.4

Figure 5.2.4: Comparison of reaction progress profiles of the uncatalysed Kemp elimination reaction of 5-nitrobenzisoxazole at various pH and a table of pH versus $\log(k_{obs})$.

5.2.2 Catalysed reaction

The studies on the uncatalysed reaction showed that the background reaction proceeds at a fairly high reaction rate relative to the much slower background reaction rate of unsubstituted benzisoxasole. So for this work, in order to minimise the effects of the high background reaction rate for free substrate, high concentrations of cage were needed, as well as low guest concentrations, so that there was little ‘free’ guest and so that the background (uncatalysed) pathway was therefore minimised. This is often referred to as sub-saturation conditions and is regularly used in enzyme kinetics experiments since it greatly simplifies the experiment.[14]

However, as the **Os•Zn** cage used in this research has such high UV/Vis extinction coefficient, to attain the required concentration of 0.15 mM without having too high an optical density, a UV/vis cuvette with a shorter path length was needed: so a 2 mm cuvette has been used. This is so that the observed increase in the product at 380 nm can be detected above the strong cage absorption. Figure 5.2.5 shows the absorption profile of the cage, the starting material and the product. The cage absorbs across the range of 200-600 nm, so when examining reactions of organic molecules, it would be hard to find a guest whose absorption spectrum does not significantly overlap with the cage absorption. However, by using a cuvette of 0.2 cm path length instead of 1 cm, the absorption of the solution can be reduced without reducing its concentration. The figure shows that the absorption of the 2-cyano-4-nitrophenolate product at 380 nm occurs in a low-absorbing part of the cage spectrum, so as it accumulates it can be detected above the baseline absorption of the cage.

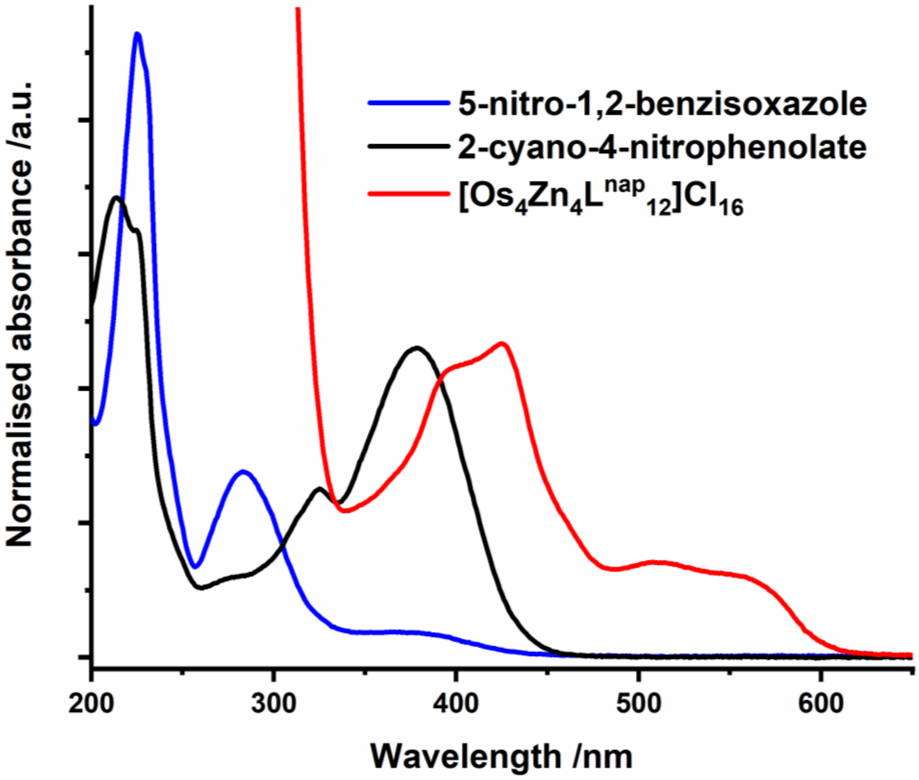

Figure 5.2.5: UV/vis spectra comparison of $[Os_4Zn_4(L^{nap})_{12}]Cl_{16}$, 5-nitro-1,2-benzisoxazole and 2-cyano-4-nitrophenolate.

Reaction conditions were first determined at pH 9.2 using a borax buffer. The pH was checked at the start and end of the reactions, to confirm that the buffer was working and that the pH was not changing throughout the measurements.

As the reaction was performed in a 2 mm cuvette: the reaction could not be stirred *in situ*, however the temperature was controlled at 25 ºC. Initially the whole UV/Vis spectrum (200-800 nm) was recorded at every time interval to see if the reaction was behaving in the expected way and once this was confirmed; the reaction was subsequently monitored by just measuring the absorption increase at 380 nm. To analyse the data, plots of [product] *vs.* time were derived, as well as plots of log[starting material] *vs.* time. The plots of log[starting material] *vs.* time were then fit to a straight line to determine the rates of reaction. This could be done, as the first 2 hours of the experiment showed pseudo first-order rate behaviour. Despite the usual Michaelis-Menten equation that is used for looking at enzyme kinetics, for this work – as the guest concentration was so small and because the percentage of bound cage does not change that much at these concentrations – then we can approximate simple first order behaviour.

Looking at the first results of these catalysis experiments, figure 5.2.6 shows the reaction rate profile of the catalysed (with **Os•Zn** cage) and uncatalysed (no cage) reactions at pH 9.2. These figures show a clear increase in reaction rate in the presence of catalyst, with $k_{\mathrm{cat}} = 2.0 \times 10^{-4}\ \mathrm{s}^{-1}$ and $k_{\mathrm{uncat}} = 8.1 \times 10^{-5}\ \mathrm{s}^{-1}$ (the measurements have all been repeated at least 3 times). This suggests that the **Os•Zn** cage does catalyse this reaction, probably by the same mechanism as was previously observed with $[\mathrm{Co_8(L^w)_{12}}](\mathrm{BF_4})_{16}$. However, the rate enhancement ($k_{\mathrm{cat}}/k_{\mathrm{uncat}}$) for this experiment, is only 3, which is very low compared to the previous work with 1,2-benzisoxazole which showed a rate enhancement of 10^5 at pH 9. This difference in enhancement could potentially be due to the large increase in rate of the uncatalysed (background) of 5-nitrobenzisoxazole, or it could also arise from different mechanistic factors.

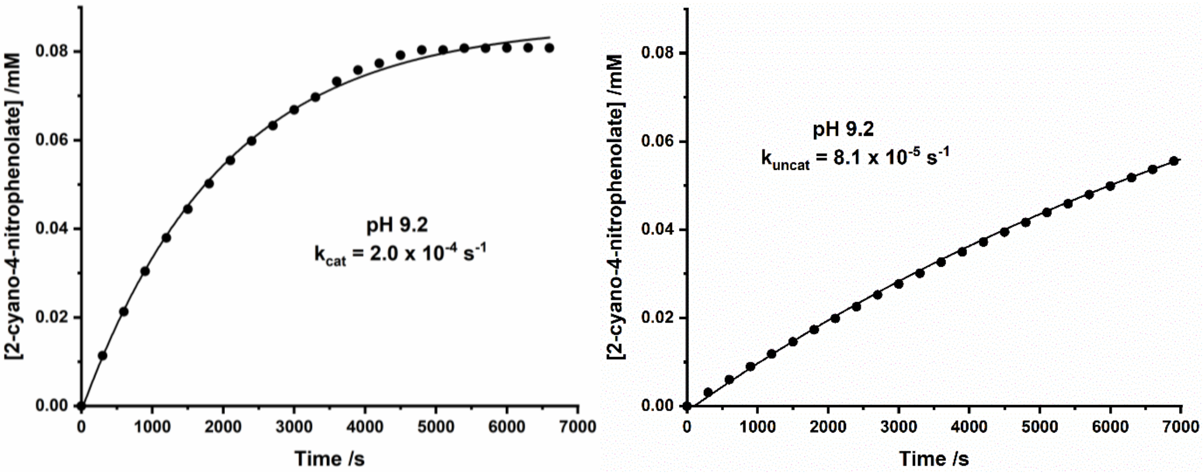

Figure 5.2.6: Comparison of rate profiles at pH 9, of **Os•Zn** catalysed and uncatalysed reactions.

To see if this rate enhancement could be improved, the reaction was performed at pH 8.2, as the background reaction is slower at lower pH. If the mechanism of catalysis is the same as that in the previous work using 1,2-benzisoxazole as substrate, then slowing down the background reaction should give a larger $k_{\mathrm{cat}}/k_{\mathrm{uncat}}$ value.

Figure 5.2.7 shows the comparison of rate curves for the cage catalysed and background reaction at pH 8.2. Again, there is an increase in rate of reaction for the catalysed ($2.1 \times 10^{-4}\ \mathrm{s}^{-1}$) compared to that of the uncatalysed ($3.4 \times 10^{-5}\ \mathrm{s}^{-1}$) reaction. This equates to a rate enhancement of 6, which is still low, but is significantly higher than the rate enhancement recorded at pH 9.2 (3). What is also interesting is that the values of k_{cat} at pH 8 and 9 are quite similar to each other (pH 8: $2.0 \times 10^{-4}\ \mathrm{s}^{-1}$ and pH 9: $2.1 \times 10^{-4}\ \mathrm{s}^{-1}$). This is also the case with the results of the previous work using 1,2-benzisoxazole, which showed that the cage catalysed reaction was unaffected by pH as the reaction sphere of $^{-}$OH around the cage was already saturated with hydroxide ions by pH 8, so the local hydroxide concentration was fairly constant.

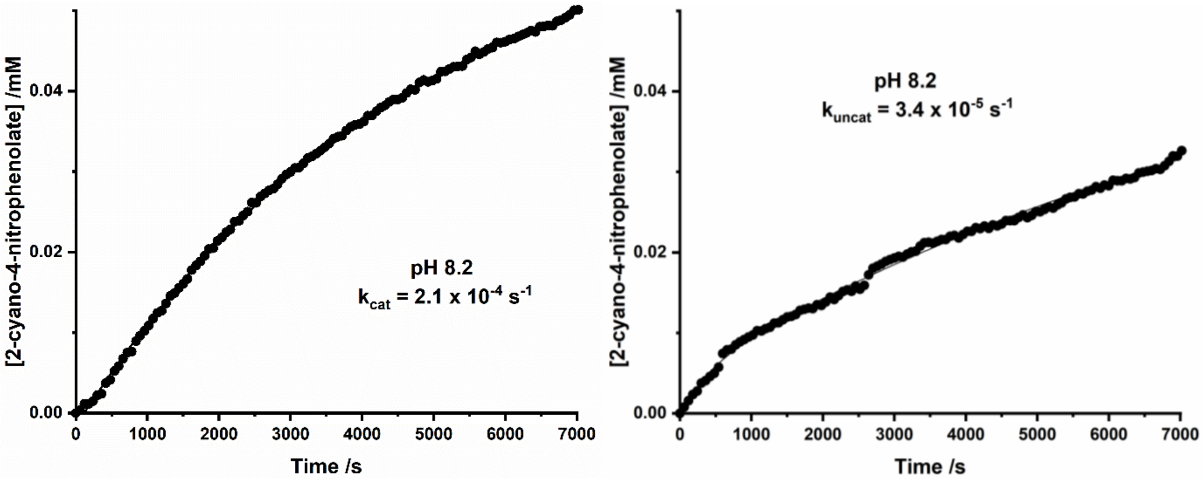

Figure 5.2.7: Comparison of rate profiles at pH 8.2, of the **Os•Zn** catalysed and uncatalysed reactions.

5.2.3 Method of catalysis

To investigate the catalysis in more detail a few control experiments were performed. Firstly, the use of a competitively binding guest (cycloundecanone) was achieved, which has been proven to bind strongly within the cage cavity in water (10^6 M^{-1}) and so we would expect it to displace a more weakly binding guest like 5-nitrobenzisoxazole ($K \approx 10^4$ M^{-1}) from the cavity. In this case, we would expect the rate to drop to that of the uncatalysed reaction as the substrate will be expelled from the cavity and free in solution.

However, the results show (figure 5.2.8) a slight *increase* (by a factor of 2.3) in reaction rate when cycloundecanone (C11) is added to the solution (the overall rate increases from 2.1 x 10^{-4} s^{-1} to 4.9 x 10^{-4} s^{-1}). The reason for this is unclear and suggests that the mechanism for the reaction with 5-nitrobenzisoxasole is different from that of 1,2-benzisoxazole, where the addition of cycloundecanone fully inhibited the reaction.[5]

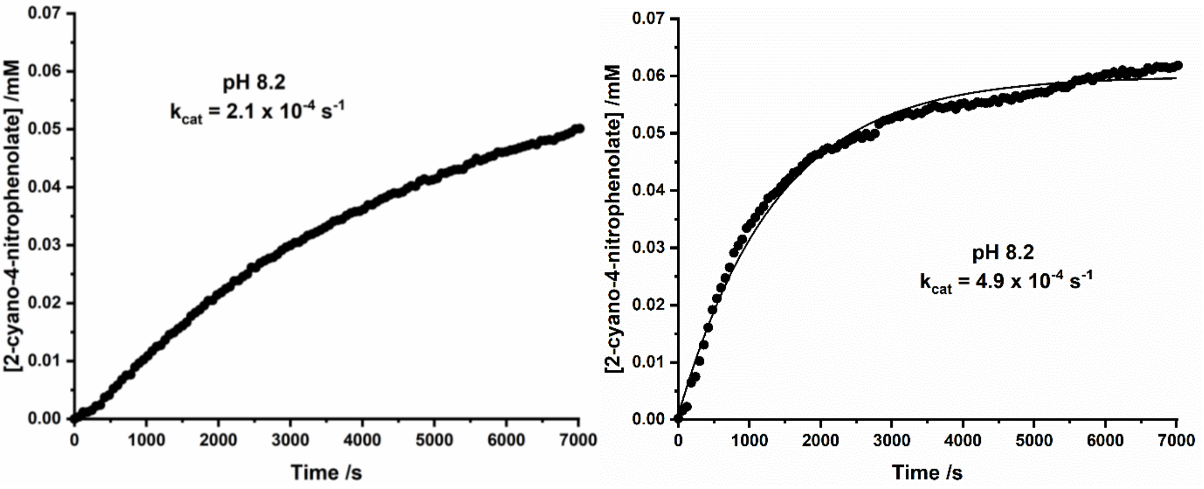

Figure 5.2.8: Comparison of rate profiles at pH 8.2, of the **Os•Zn** catalysed reaction without (left) and with (right) added cycloundecanone.

To determine whether this effect was due to the difference between the Os(II) based cage and the Co(II) based cage, the reaction was performed with $[Co_8(L^w)_{12}](BF_4)_{16}$ under the same reaction conditions. This would show whether the difference in behaviour is specifically associated with the Os(II) cage and also whether the use of a chloride counter ion in this work has a large effect on the rates. Because previous work has shown that the addition of chloride is known to decrease the rate of reaction by displacing hydroxide ions from around the cage surface.[16,10,17] Chloride ions (compared to hydroxide ions) are preferentially bound to the interface region of cationic micelles (typically 10 fold[9,18]) and so in this case, chloride displaces the hydroxides in the cage windows therefore inhibiting the reaction as hydroxide surface binding is crucial for catalysis to occur.

Figure 5.2.9 shows the comparison between the reaction profiles of the reaction of $[Co_8(L^w)_{12}](BF_4)_{16}$ with and without cycloundecanone. As observed above, there is also a clear increase in rate (factor of 5) upon addition of the supposedly inhibiting guest. Also notable is the similarity in rate of the **Os•Zn**-catalysed reaction in the presence of cycloundecanone (4.9 x 10^{-4} s^{-1}), and the $[Co_8(L^w)_{12}](BF_4)_{16}$-catalysed reaction in the presence of cycloundecanone (5.6 x 10^{-4} s^{-1}). We also note that the reaction rate when using $[Co_8(L^w)_{12}](BF_4)_{16}$ is similar to that obtained using **Os•Zn** as catalyst, which is unexpected as the chloride counter-anion in the latter case was thought to have the potential to inhibit the reaction rate slightly.

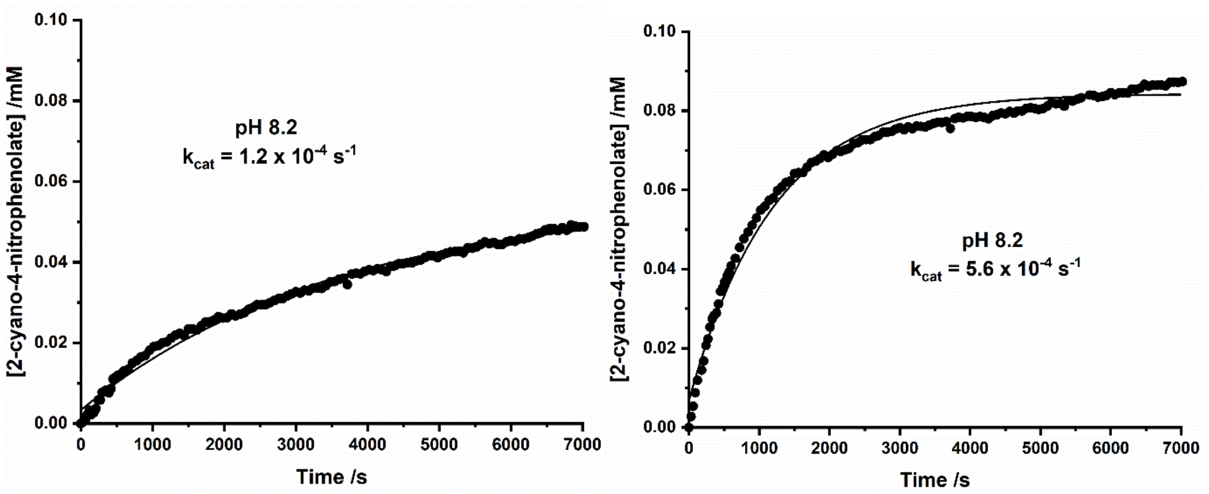

Figure 5.2.9: Comparison of rate profiles at pH 8.2, of $[Co_8(L^w)_{12}](BF_4)_{16}$ and $[Co_8(L^w)_{12}](BF_4)_{16}$ and cycloundecanone catalysis reactions.

Overall the slight increase in reaction rate in the presence of cycloundecanone suggests that the substrate when bound inside the cavity does not react effectively, possibly because it is not in an optimal orientation with respect to the layer of hydroxides around it. Therefore, the cage actually inhibits the reaction by protecting the substrate. On displacement of the substrate from the cage cavity using cycloundecanone the reaction is accelerated slightly because it now occurs at the *exterior* surface of the cage, with which it can associate *via* hydrophobic interactions, bringing the nitrobenzisoxazole into the region of locally high hydroxide concentration. Other members of the group have recently obtained evidence for catalysed reactions actually occurring at the external surface of the cage in a similar way using phosphotriester substrates.[19]

One way of testing this theory would be to lower the concentration of the cage and increase the concentration of starting material. This would give an indication on how large an effect the cage has on catalysis and differentiating that to the effects due to starting material, product and cycloundecanone. Another useful control experiment would be to use a small tetrahedral cage that cannot accommodate the guest but still has a charged exterior surface, and see whether the cage still acted as a catalyst.

What is also interesting is how different the behaviour is between 5-nitrobenzisoxasole and 1,2-benzisoxazole;0 this could potentially be due to how the substrate binds in the cage and how available the active site is in terms of being correctly positioned in the cavity to interact with external hydroxide ions. It would be interesting to monitor the reaction via NMR spectroscopy to determine whether there is any additional interactions or any additional products being formed, this can be done using $[Co_8(L^w)_{12}](BF_4)_{16}$ due to it being paramagnetic and spreading out the proton peaks which simplifies analysis.

5.2.4 Catalysis with oxidised cage

In addition to these findings, the reason why **Os•Zn** was of interest for this work, was because it could potentially be used as a redox-switchable catalyst, whereby increasing the oxidation state of the cage could lead to an increase in the concentration of hydroxide ions that aggregate around the cage (figure 5.2.10). Thus if the mechanism were the same as in the previous work, then this could lead to an increase in catalysis. For this use, **Os•Zn** has an obvious advantage over $[Co_8(L^w)_{12}](BF_4)_{16}$, as with **Os•Zn**, the Os(III) oxidation state is readily accessible and has long-term stability, which is not the case for the Co(II) based cage.

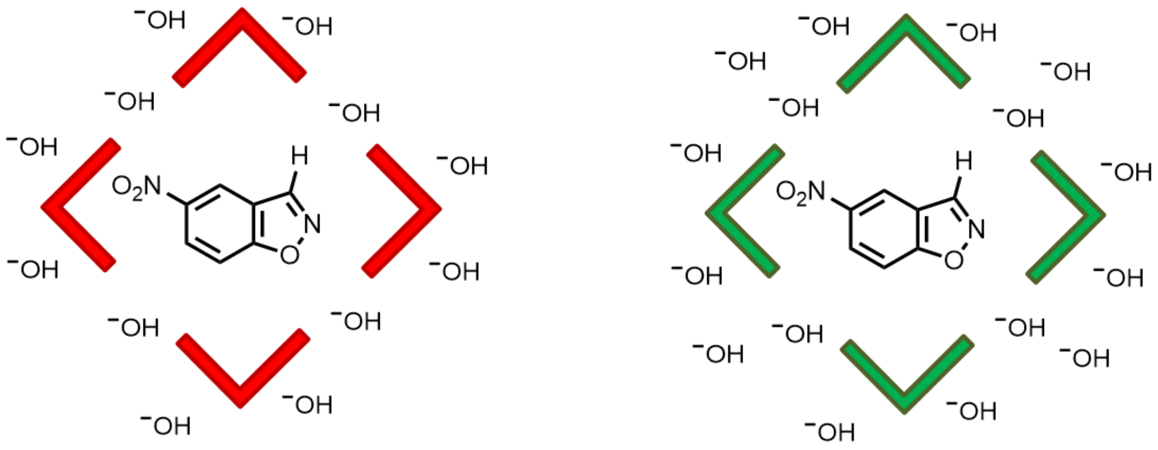

Figure 5.2.10: Depiction of **Os•Zn** cage with 16 anions vs. with 20 anions.

The first method of oxidation that was tried was electrochemical. The cage has an oxidation potential of +0.7 V for the Os(II)/Os(III) couple (*vs.* SCE in H_2O). Using a 1 cm path length cuvette into which was placed; a Pt gauze working electrode, an Ag wire reference electrode and a Pt wire counter electrode, the working electrode potential was held at +1 V and changes in the resulting UV/Vis spectra were monitored (figure 5.2.11). The results showed that the cage took quite a long time to fully oxidise due to the volume of material in the cuvette, leading to inefficient mass transport of material to the electrode surface. In addition, the oxidised material did not stay oxidised for a long time, but spontaneously re-reduced in air. We could avoid these issues by using a much thinner (0.5 mm path length) cuvette designed for spectroelectrochemistry (OTTLE cell),[20] which would allow all of the solution around the Pt gauze to be oxidised quickly. However, addition of the substrate (5-nitrobenzisoxazole) and efficient mixing of the solution would be difficult. These issues are all mechanical and would require an adaption of the experimental setup, which can be easily done if more time allowed and if enough material was synthesised.

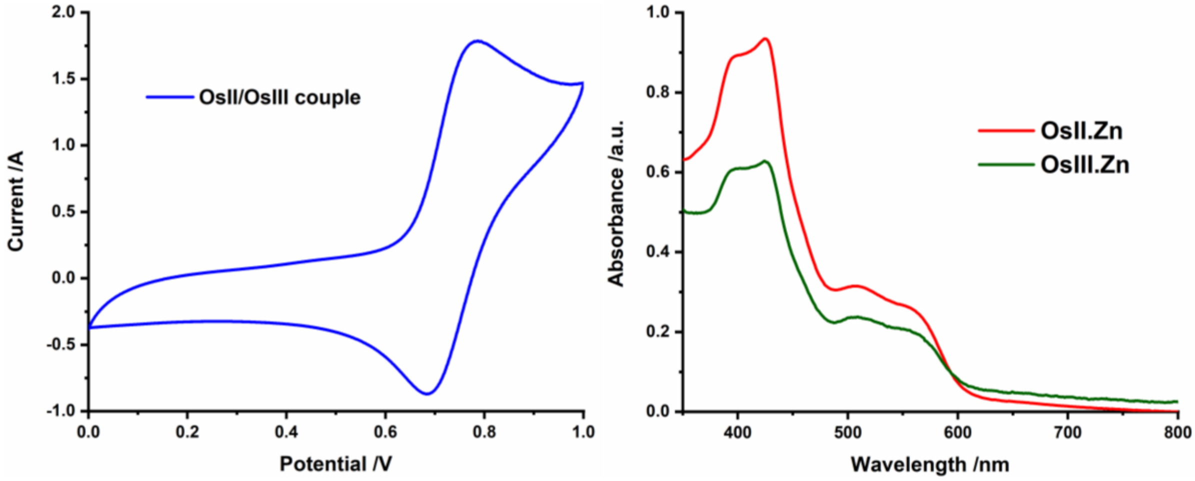

Figure 5.2.11: Cyclic voltammogram of Os•Zn oxidation and UV/vis spectra from a spectroelectrochemistry experiment.

To avoid these difficulties associated with performing the catalysis while simultaneously performing electrochemical oxidation of the catalyst, we decided to test whether the cage could be oxidised through chemical methods. Therefore, it was decided to see if there were any appropriate chemical oxidants. The first chemical oxidant tried was ammonium persulfate, which had been shown previously to successfully oxidise the cage. In first use, where 2 equivalents of oxidant were added [as each cage has 4 Os(II) units, and the persulfate ion is a 2-electron oxidant] the cage took 20 mins to oxidise and then stayed oxidised for ~10 minutes before spontaneous re-reduction in aqueous solution (figure 5.2.12). This change was observed by following the change in absorbance of the cage at 380 nm (where 2-cyano-4-nitrophenolate absorbs). As shown in figure 5.2.11, the cage absorbance significantly decreases once oxidised and then returns (in air) to the original Os(II) absorbance. The amount of oxidant used was adjusted and increased to a level which maintained the cage in its fully oxidised state, without precipitation, for long enough to perform a catalytic reaction with. This led to the cage being oxidised fully in 30 mins, and then stayed oxidised for 1-2 hours (at pH 9.2). If a neutral or lower pH was used then the cage would be more stable in solution and will stay oxidised for longer, for example at pH 2 the cage does not revert to Os(II) at all: however, unfortunately, basic conditions are needed for the elimination reaction.

Using an inert atmosphere slightly improved the lifetime of the oxidised form of the cage. However, this presented practical difficulties associated with the addition of the solid guest substrate into the UV/Vis cuvette to monitor the reaction and most significantly, cuvettes with a Youngs tap fitted did not fit inside the temperature controlled UV/Vis spectrometers.

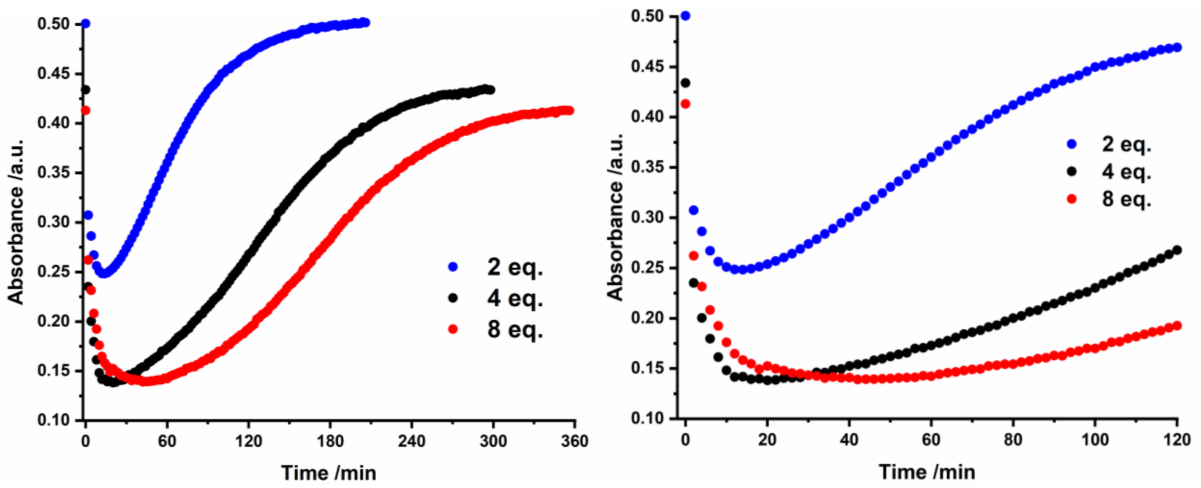

Figure 5.2.12: Left: graph showing the change in absorbance (at 380 nm) over time of **Os•Zn** upon addition of ammonium persulfate oxidant of various concentrations. Right – expanded graph of the change in absorbance (0-120 mins).

Despite these hurdles, the oxidised cage was stable enough at high pH for a period of time long enough to measure the accumulation of 2-cyano-4-nitrophenolate product. At pH 9.2, the rates of reaction catalysed by the oxidised and non-oxidised cages are essentially the same (k_{cat} = 2.3 x 10^{-4} s^{-1} and 2.0 x 10^{-4} s^{-1} respectively) and so no increase in catalysis could be observed (figure 5.2.13) as the cage was oxidised from 16+ to 20+. To investigate this work further, it could be beneficial to use unsubstituted 1,2-benzisoxazole as the substrate, as the catalysed reaction is much faster and any rate changes associated with changes in cage oxidation state would be easier to detect. Accumulation of 2-cyanophenolate is not easy to follow by UV/Vis spectroscopy, due to overlap with strong absorbance from the cage; therefore, these experiments would need to be done through NMR spectroscopy, with (ideally) an electrode array in the NMR tube that allowed the cage to be oxidised *in situ* in the NMR instrument - a formidable experimental challenge.

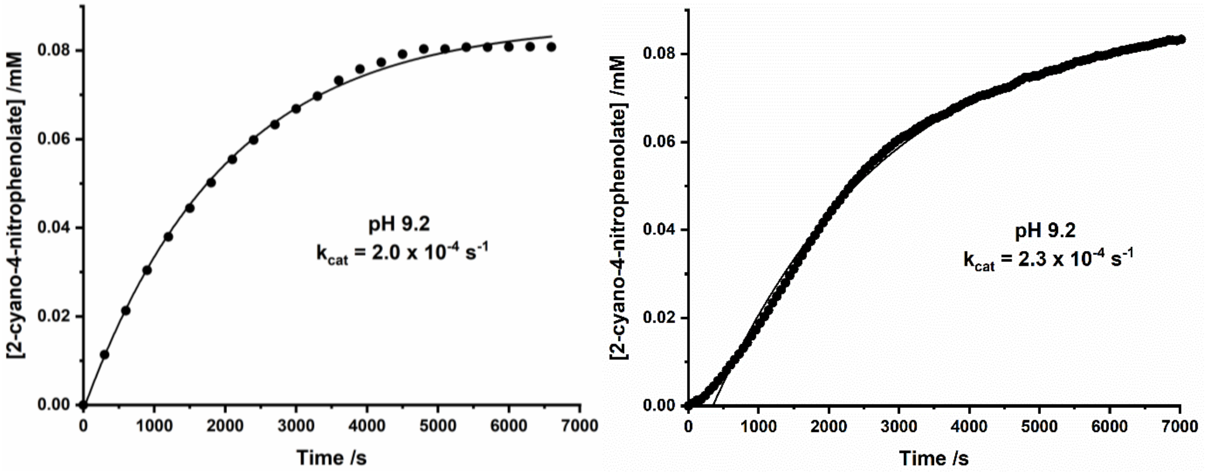

Figure 5.2.13: Comparison of rate profiles at pH 9.2, of **Os(II)•Zn** (left) and **Os(III)•Zn** (right) catalysed reactions (Kemp elimination with 5-nitrobenzisoxazole).

5.3 Conclusions

In summary, the heterometallic cage, **Os•Zn**, catalyses the Kemp elimination reaction of 5-nitrobenzisoxazole with a rate enhancement of 6 times, at pH 8.2. The isostructural Co(II)-based cage $[Co_8(L^w)_{12}](BF_4)_{16}$ similarly enhances the rate of this reaction by a factor of 4. However, control tests using a competitively binding guest, which blocks the access of the substrate to the cavity, showed that expulsion of the substrate from the cavity actually slightly increased the reaction rate. Suggesting that the reaction proceeds more effectively at the exterior surface of the cage rather than inside the cavity, possibly because of issues associated with correct positioning / orientation of the bound guest.

In addition, it has been found that the Os(II) units of **Os•Zn**, at basic pH, can be oxidised to Os(III) and this can be achieved through electrochemical or chemical means. This oxidised cage containing four Os(III) ions, with a charge of 20+ rather than 16+, has been found not to enhance the rate of catalysis beyond that of the Os(II) cage – in contrast to what Raymond and co-workers observed in a different cage-catalysed reaction by changing the charge on the cage. To determine the effect of the increased oxidation state of this cage on catalysis, a different reaction will need to be studied or the mechanism of this reaction will need to be determined first. Attempts have been made to follow the much faster elimination of 1,2-benzisoxazole catalysed by **Os•Zn** *via* ^{1}H NMR spectroscopy, but reaction conditions need to be adapted as the signals of starting material, 1,2-benzisoxazole, and the subsequent product (2-cyanophenolate) were masked by the aromatic ^{1}H signals of the **Os•Zn** cage.

Further work would be to determine the mechanism of the cage-catalysed reaction of 5-nitrobenzisoxazole; through varying the concentrations/equilibrium of cage and guest, performing the catalysis with a smaller, non-binding tetrahedral cage to study the effect of the exterior surface and also by following the reaction by ^{1}H NMR spectroscopy to verify the reaction products. Further work relating to the investigation of charge dependence on catalysis would be to; develop the electrochemical oxidation of **Os•Zn**, optimise the **Os•Zn** catalysis of 1,2-benzisoxasole (by NMR) and also to explore the use of chromium as a metal corner in cubic cages (to utilise its various oxidation states).

This work has shown that Os(II) cages can utilise the Os(II)/Os(III) swing for redox-based modulation of catalysis as well as the long-lived electron-donor excited state for applications in photocatalysis.

5.4 Experimental

5.4.1 Experimental techniques

NMR titration

$[Co_8L_{12}](Cl)_{16}$ was prepared according to previously published methods.[21] A stock host solution of $[Co_8L_{12}](Cl)_{16}$ (0.15 mM) in D_2O was used and 5-nitro-1,2-benzisoxazole (0.183 mg, 0.45 mM) was dissolved in 2.5 ml of the host solution and a drop of gaseous Hydrochloric acid added to give a pH of 4. The changes in chemical shift with increasing concentration of guest were plotted and fitted to a 1:1 host:guest binding model. The NMR data was processed using either Bruker Topspin 4.0.3 and was fitted to binding isotherms using 14allMaster.xls, which is a macro-based Excel fitting program written by Prof. Christopher A. Hunter (University of Cambridge).

Monitoring the reaction

5-nitro-1,2-benzisoxazole (0.015 – 0.017 mg, 0.13 – 0.15 mM) was added to buffered cage ($[Os_4Zn_4(L^{nap})_{12}]Cl_{16}$ or $[Co_8(L^{w})_{12}](BF_4)_{16}$) solution (0.15 mM, 0.7 ml), sonicated for 10 seconds and then pipetted into a 0.2 mm path length cuvette. When performing the reaction with Os(III), the reaction conditions were the same aside from the addition of ammonium persulfate (40 μL of 42 mM solution) to $[Os_4Zn_4(L^{nap})_{12}]Cl_{16}$ 25 minutes before the addition of guest. Also when performing the control experiments with the competitive binder, cycloundecanone (2 μL, 15 mM) was added to the cage solution and sonicated before adding the guest. To control the pH a borate buffer was used, with the concentrations being; borax 10 mM for pH 9.2; borax/boric acid 2 mM/20 mM for pH 8.2 and borax/NaOH 10 mM/25mM at pH 10.2.

The catalysed reactions were followed by UV/vis spectroscopy, either using a Cary 50 spectrometer or a temperature controlled (25 °C) Cary 300 bio spectrometer. The experiments were initially monitored using the Scanning Kinetics function, where the whole UV/vis spectrum (200 -800 nm) was measured every 2 minutes, then once the conditions were determined the Kinetics function was used and the product grow in was monitored at 380 nm. Each experiment was repeated at least 3 times and the resultant rate constants were averaged. To obtain k_{uncat} and k_{cat}, log(starting material) against time was fit to a linear equation.

UV/vis Spectroelectrochemistry measurements

Spectroelectrochemical measurements were performed using an open top 1 cm path length cuvette, with a Pt mesh working electrode, a Pt coil counter electrode and Ag wire pseudo-reference electrode. The UV/vis spectra were performed using a Cary 5000 spectrophotometer. $[Os_4Zn_4(L^{nap})_{12}]Cl_{16}$ (50 μM) was buffered to pH 8.55 using a borate (borax/boric acid) buffer and the measurements were performed in both degassed (N_2) and non-degassed conditions, with no difference in results under either conditions.

X-ray Crystallography

The $[Co_8(L^{nap})_{12}](BF_4)_{16}$•2(5-nitrobenzisoxazole) diffraction data was collected and refined by Christopher Taylor (University of Warwick). The data was collected at the UK Diamond Light Source Synchrotron facility (proposal MT19876). The structure determination suffered from the usual weak scattering characteristic of crystals of this type, associated with large unit cells and disorder of solvents/anions. The X-ray diffraction limit of the crystal was set at 0.69 Å resolution (SHEL 999). Large solvent-accessible voids containing diffuse electron density that could not be satisfactorily modelled were accounted for using the SQUEEZE command in PLATON. Full details of the refinement and treatment of this structure, including software used, are given in the CIF.

5.4.2 Synthetic procedures

Starting materials

5-nitro-1,2-benzisoxazole, $[Os_4Zn_4(L^{nap})_{12}]Cl_{16}$, $[Co_8L_{12}](Cl)_{16}$ and $[Co_8(L^{w})_{12}](BF_4)_{16}$ were all prepared according to previously published methods.[13,16,22,23] Single crystals of $[Co_8(L^{nap})_{12})](BF_4)_{16}$ used for determination of the structure of the $[Co_8(L^{nap})_{12})](BF_4)_{16}$•5-nitrobenzisoxazole adduct were also prepared as described previously.[15] All other reagents were purchased from Sigma-Aldrich or Flourochem and used as received.

Chemical cage oxidation

To determine the appropriate conditions for oxidising $[Os_4Zn_4(L^{nap})_{12}]Cl_{16}$, various volumes (5 – 50 μL) of Ammonium persulfate$_{(aq)}$ solution (42 mM) were added to buffered cage. The oxidation was followed by UV/vis spectroscopy using a Cary 50 or Cary 5000 spectrometer and the reactions were performed in degassed (Ar) and non-degassed conditions, with the oxidation product being more stable when the solution was degassed.

5.5 References

1 C. Tan, D. Chu, X. Tang, Y. Liu, W. Xuan and Y. Cui, *Chem. - A Eur. J.*, 2019, **25**, 662–672.

2 C. M. Hong, R. G. Bergman, K. N. Raymond and F. D. Toste, *Acc. Chem. Res.*, 2018, **51**, 2447–2455.

3 Y. Fang, J. A. Powell, E. Li, Q. Wang, Z. Perry, A. Kirchon, X. Yang, Z. Xiao, C. Zhu, L. Zhang, F. Huang and H.-C. Zhou, *Chem. Soc. Rev.*, 2019, **48**, 4707-4730.

4 C. J. Hastings, M. D. Pluth, R. G. Bergman and K. N. Raymond, *J. Am. Chem. Soc.*, 2010, **132**, 6938–6940.

5 W. Cullen, M. C. Misuraca, C. A. Hunter, N. H. Williams and M. D. Ward, *Nat Chem.*, 2016, **8**, 1–6.

6 C. J. Hastings, R. G. Bergman and K. N. Raymond, *Chem. - A Eur. J.*, 2014, **20**, 3966–3973.

7 D. Röthlisberger, O. Khersonsky, A. M. Wollacott, L. Jiang, J. DeChancie, J. Betker, J. L. Gallaher, E. A. Althoff, A. Zanghellini, O. Dym, S. Albeck, K. N. Houk, D. S. Tawfik and D. Baker, *Nature*, 2008, **453**, 190–195.

8 E. Sanchez, S. Lu, C. Reed, J. Schmidt and M. Forconi, *J. Phys. Org. Chem.*, 2016, **29**, 185–189.

9 J. E. Klijn and J. B. F. N. Engberts, *J. Am. Chem. Soc.*, 2003, **125**, 1825–1833.

10 M. L. Casey, D. S. Kemp, K. G. Paul and D. D. Cox, *J. Org. Chem.*, 1973, **38**, 2294–2301.

11 C. M. Hong, M. Morimoto, E. A. Kapustin, N. Alzakhem, R. G. Bergman, K. N. Raymond and F. D. Toste, *J. Am. Chem. Soc.*, 2018, **140**, 6591–6595.

12 D. Fiedler, R. G. Bergman and K. N. Raymond, *Angew. Chemie - Int. Ed.*, 2004, **43**, 6748–6751.

13 Y. Miao, R. Metzner and Y. Asano, *ChemBioChem*, 2017, **18**, 451–454.

14 D. L. Purich, *Enzyme Kinetics: Catalysis & Control: A Reference of Theory and Best-Practice Methods*, 2010.

15 S. Turega, W. Cullen, M. Whitehead, C. A. Hunter and M. D. Ward, *J. Am. Chem. Soc.*, 2014, **136**, 8475–8483.

16 W. Cullen, A. J. Metherell, A. B. Wragg, N. H. Williams and M. D. Ward, *J. Am. Chem. Soc.*, 2018, **140**, 2821–2828.

17 D. S. Kemp and M. L. Casey, *J. Am. Chem. Soc.*, 1973, **95**, 6670–6680.

18 J. E. Klijn and J. B. F. N. Engberts, *Org. Biomol. Chem.*, 2004, **2**, 1789.

19 C. G. P. Taylor, A. J. Metherell, S. P. Argent, F. Ashour, N. H. Williams and M. D. Ward, *Chem. - A Eur. J.*

20 S. Lee, R. Kowallick, M. Marcaccio, J. A. Mccleverty and M. D. Ward, *Dalt. Trans.*, 1998, 3443–3450.

21 W. Cullen, S. Turega, C. A. Hunter and M. D. Ward, *Chem. Sci.*, 2015, **6**, 2790–2794.

22 J. S. Train, A. B. Wragg, A. J. Auty, A. J. Metherell, D. Chekulaev, C. G. P. Taylor, S. P. Argent, J. A. Weinstein and M. D. Ward, *Inorg. Chem.*, 2019, **58**, 2386–2396.

23 M. Whitehead, S. Turega, A. Stephenson, C. A. Hunter and M. D. Ward, *Chem. Sci.*, 2013, **4**, 2744–2751.

5.6 Appendix

Table 5.6.1: *Crystal data and structure refinement for* $[Co_8(L^{nap})_{12}](BF_4)_{16}\bullet 2$*(5-nitrobenzisoxazole).*

Identification code	DMWMSv6-103_sq
Empirical formula	$C_{374.84}H_{392.48}B_{14.2}Cl_{1.8}Co_8F_{56.8}N_{74.24}O_{34.36}$
Formula weight	8255.24
Temperature/K	100(1)
Crystal system	monoclinic
Space group	C2/c
a/Å	33.12481(19)
b/Å	30.0412(2)
c/Å	40.1650(3)
α/°	90.0
β/°	95.9731(6)
γ/°	90.0
Volume/Å^3	39751.6(3)
Z	4
ρ_{calc}g/cm^3	1.379
μ/mm^{-1}	0.409
F(000)	17060.0
Crystal size/mm^3	0.13 × 0.1 × 0.08
Radiation	Synchrotron (λ = 0.6889)
2Θ range for data collection/°	1.972 to 59.894
Index ranges	$-48 \le h \le 48$, $-43 \le k \le 43$, $-58 \le l \le 58$
Reflections collected	342014
Independent reflections	63327 [R_{int} = 0.0778, R_{sigma} = 0.0672]
Data/restraints/parameters	63327/6797/2523
Goodness-of-fit on F^2	1.038
Final R indexes [I>=2σ (I)]	R_1 = 0.0886, wR_2 = 0.2897
Final R indexes [all data]	R_1 = 0.1387, wR_2 = 0.3254
Largest diff. peak/hole / e Å^{-3}	1.33/-0.74